ORTA DOĞU TEKNİK ÜNİVERSİTESİ
FEN BİLİMLERİ ENSTİTÜSÜ MÜDÜRLÜĞÜ

TEZ ŞABLONU ONAY FORMU
THESIS TEMPLATE CONFIRMATION FORM

1. Şablonda verilen yerleşim ve boşluklar değiştirilmemelidir.
2. **Jüri tarihi** Başlık Sayfası, İmza Sayfası, Abstract ve Öz'de ilgili yerlere yazılmalıdır.
3. İmza sayfasında jüri üyelerinin unvanları doğru olarak yazılmalıdır. Tüm imzalar **mavi pilot kalemle** atılmalıdır.
4. **Disiplinlerarası** programlarda görevlendirilen öğretim üyeleri için jüri üyeleri kısmında tam zamanlı olarak çalıştıkları anabilim dalı başkanlığının ismi yazılmalıdır. Örneğin: bir öğretim üyesi Biyoteknoloji programında görev yapıyor ve biyoloji bölümünde tam zamanlı çalışıyorsa, İmza sayfasına biyoloji bölümü yazılmalıdır. İstisnai olarak, disiplinler arası program başkanı ve tez danışmanı için disiplinlerarası program adı yazılmalıdır.
5. Tezin **son sayfasının sayfa** numarası Abstract ve Öz'de ilgili yerlere yazılmalıdır.
6. Bütün chapterlar, referanslar, ekler ve CV sağ sayfada başlamalıdır. Bunun için **kesmeler** kullanılmıştır. **Kesmelerin kayması** fazladan boş sayfaların oluşmasına sebep olabilir. Bu gibi durumlarda paragraf (¶) işaretine tıklayarak kesmeleri görünür hale getirin ve yerlerini **kontrol edin**.
7. Figürler ve tablolar kenar boşluklarına taşmamalıdır.
8. Şablonda yorum olarak eklenen uyarılar dikkatle okunmalı ve uygulanmalıdır.
9. Tez yazdırılmadan önce PDF olarak kaydedilmelidir. Şablonda yorum olarak eklenen uyarılar PDF dokümanında yer almamalıdır.
10. Tez taslaklarının kontrol işlemleri tamamlandığında, bu durum öğrencilere METU uzantılı öğrenci e-posta adresleri aracılığıyla duyurulacaktır.
11. Tez yazım süreci ile ilgili herhangi bir sıkıntı yaşarsanız, Sıkça Sorulan Sorular (SSS) sayfamızı ziyaret ederek yaşadığınız sıkıntıyla ilgili bir çözüm bulabilirsiniz.

1. Do not change the spacing and placement in the template.
2. Write **defense date** to the related places given on Title page, Approval page, Abstract and Öz.
3. Write the titles of the examining committee members correctly on Approval Page. **Blue ink** must be used for all signatures.
4. For faculty members working in **interdisciplinary programs**, the name of the department that they work full-time should be written on the Approval page. For example, if a faculty member staffs in the biotechnology program and works full-time in the biology department, the department of biology should be written on the approval page. Exceptionally, for the interdisciplinary program chair and your thesis supervisor, the interdisciplinary program name should be written.
5. Write **the page number of the last page** in the related places given on Abstract and Öz pages.
6. All chapters, references, appendices and CV must be started on the right page. **Section Breaks** were used for this. **Change in the placement** of section breaks can result in extra blank pages. In such cases, make the section breaks visible by clicking paragraph (¶) mark and **check their position.**
7. All figures and tables must be given inside the page. Nothing must appear in the margins.
8. All the warnings given on the comments section through the thesis template must be read and applied.
9. Save your thesis as pdf and Disable all the comments before taking the printout.
10. This will be announced to the students via their METU students e-mail addresses when the control of the thesis drafts has been completed.
11. If you have any problems with the thesis writing process, you may visit our Frequently Asked Questions (FAQ) page and find a solution to your problem.

☒ **Yukarıda bulunan tüm maddeleri okudum, anladım ve kabul ediyorum. / I have read, understand and accept all of the items above.**

Name : Halim
Surname : Polat
E-Mail : halim.polat@metu.edu.tr
Date :
Signature : _____

AN ARRAY OF SQUARE PLATE RESONATORS WITH ADJUSTABLE RESONANCE FREQUENCY

A THESIS SUBMITTED TO
THE GRADUATE SCHOOL OF NATURAL AND APPLIED SCIENCES
OF
MIDDLE EAST TECHNICAL UNIVERSITY

BY

HALİM POLAT

IN PARTIAL FULFILLMENT OF THE REQUIREMENTS
FOR
THE DEGREE OF MASTER OF SCIENCE
IN
MECHANICAL ENGINEERING

AUGUST 2022

Approval of the thesis:

AN ARRAY OF SQUARE PLATE RESONATORS WITH ADJUSTABLE RESONANCE FREQUENCY

submitted by **HALİM POLAT** in partial fulfillment of the requirements for the degree of **Master of Science** in **Mechanical Engineering, Middle East Technical University** by,

Prof. Dr. Halil Kalıpçılar
Dean, Graduate School of **Natural and Applied Sciences** _____

Prof. Dr. M. A. Sahir Arıkan
Head of the Department, **Mechanical Engineering** _____

Assoc. Prof. Dr. Kıvanç Azgın
Supervisor, **Mechanical Engineering, METU** _____

Examining Committee Members:

Assoc. Prof. Dr. Mehmet Bülent Özer
Metallurgical and Materials Eng, METU _____

Assoc. Prof. Dr. Kıvanç Azgın
Mechanical Engineering, METU _____

Assoc. Prof. Dr. Ender Yıldırım
Mechanical Engineering, METU _____

Assist. Prof. Dr. Hakan Çalışkan
Mechanical Engineering, METU _____

Assist. Prof. Dr. Emir Kutluay
Mechanical Engineering, Hacettepe University _____

Date: 19.08.2022

I hereby declare that all information in this document has been obtained and presented in accordance with academic rules and ethical conduct. I also declare that, as required by these rules and conduct, I have fully cited and referenced all material and results that are not original to this work.

Name Last name : Halim Polat

Signature :

ABSTRACT

AN ARRAY OF SQUARE PLATE RESONATORS WITH ADJUSTABLE RESONANCE FREQUENCY

Polat, Halim
Master of Science, Mechanical Engineering
Supervisor : Assoc. Prof. Dr. Kıvanç Azgın

August 2022, 92 pages

In this study, a MEMS square plate resonator with adjustable resonance frequency is designed, mathematically modelled and verified with finite element analysis (FEA) and experiments.

Resonance frequency of microelectromechanical system (MEMS) square plate is adjusted with the help of several cutouts which are placed in unique lines like center lines and nodal lines. First of all, plates are modelled with the help of semi-analytic method called Rayleigh-Ritz method for the 1^{st} and 2^{nd} modes since higher modes have higher resonance frequencies. Later, effects of cutouts are included with subtracting kinetic and strain energies of cutouts from those of the plate. Up to 140 Hz frequency shift is proved to be achievable with simply changing position of cutouts. Electrostatic spring softening is calculated and added to general formula. Lastly, thermal effects are considered to have impact on modulus of elasticity, volume and density of the plate. Thermal effects are included in the formula with the help of thermal coefficient of expansion and temperature sensitivity is calculated to 2 Hz/˚C. Analytical model is verified with finite element modelling (FEM) at the end

of the second chapter. Several finite element analyses (FEA) including eigenfrequency and thermal modules were done to prove validity.

MEMS plates are manufactured by METU MEMS CENTER, which utilizes silicon on insulator (SOI) wafers. A basic test setup with network analyzer, vacuum chamber and power supplies is prepared to test manufactured MEMS plates to observe resonance frequency shift of the plates with cutouts. Quality factors over 9000 with a resonance frequency of 78.6 kHz is shown. With a measured temperature sensitivity of 3.8 Hz/˚C is achieved, proving that these microplate resonators are feasible temperature sensors.

Keywords: Plate vibration, Resonator, Cutout, MEMS, Temperature sensor

ÖZ

BİR DİZİ AYARLANABİLİR REZONANS FREKANSLI KARE PLAKA REZONATÖRLER

Polat, Halim
Yüksek Lisans, Makina Mühendisliği
Tez Yöneticisi: Doç. Dr. Kıvanç Azgın

Ağustos 2022, 92 sayfa

Ayarlanabilir rezonans frekansına sahip MEMS kare plakalı rezonatör tasarlanmış, matematiksel olarak modellenmiş, sonlu elemanlar analizi (FEA) ve deneylerle doğrulanmıştır.

MEMS kare plakanın rezonans frekansı, merkez çizgileri ve düğüm çizgileri gibi benzersiz çizgilere yerleştirilmiş birkaç kesik yardımıyla ayarlanır. Öncelikle, yüksek modların daha yüksek rezonans frekanslarına sahip olması nedeniyle 1. ve 2. modlar için Rayleigh-Ritz yöntemi adı verilen yarı analitik yöntem yardımıyla plakalar modellenmiştir. Daha sonra, kesiklerin etkileri, plakanınkilerden kesiklerin kinetik ve gerinim enerjileri çıkarılarak göz önünde bulundurulmuştur. 140 Hz'e kadar frekans kaymasının, yalnızca kesme konumlarının değiştirilmesiyle elde edilebileceği kanıtlanmıştır. Elektrostatik yay yumuşaması basit kapasitans formülleri kullanılarak hesaplanır ve genel formüle eklenir. Son olarak, termal etkilerin plakanın elastikiyet modülü, hacmi ve yoğunluğu üzerinde etkisi olduğu düşünülmektedir. Termal etkiler, termal genleşme katsayısı yardımıyla formüle dahil edilmiş ve sıcaklık hassasiyeti 2 Hz/˚C olarak hesaplanmıştır. Analitik model, ikinci bölümün sonunda sonlu elemanlar modellemesi (FEM) ile doğrulanmıştır.

Geçerliliği kanıtlamak için öz frekans ve termal modüller dahil olmak üzere çeşitli sonlu elemanlar analizi (FEA) yapıldı.

MEMS plakaları, yalıtkan üzerinde silikon (SOI) kullanılarak ODTÜ MEMS CENTER tarafından üretilmiştir. Plakanın kesikli rezonans frekans kaymasını gözlemlemek için üretilen MEMS plakalarını test etmek için ağ analizörü, vakum odası ve güç kaynakları ile temel bir test düzeneği hazırlanır. 78.6 kHz rezonans frekansı ile 9000'in üzerindeki kalite faktörleri gözlemlenmiştir. Ölçülen 3,8 Hz/°C sıcaklık hassasiyeti ile mikroplaka rezonatörlerinin elverişli bir sıcaklık sensörü olduğu kanıtlanmıştır.

Anahtar Kelimeler: Plaka titreşimi, Rezonatör, Kesik, MEMS, Sıcaklık sensörü

I dedicate my dissertation work to my family.

A special feeling of gratitude to my loving parents, Leyla and Kazım whose words of encouragement and push for tenacity ring in my ears.

My brothers and sisters who have always supported and advised me are very special.

ACKNOWLEDGMENTS

The author wishes to express his deepest gratitude to his supervisor Assoc. Prof. Dr. Kıvanç Azgın for their guidance, advice, criticism, encouragements and insight throughout the research.

The author would also like to thank Assoc. Prof. Dr. Ender Yıldırım and Asst. Prof. Dr. Hakan Çalışkan for their suggestions and comments.

The technical assistance of Mr. Şener Yılmaz, Mr. Emre Ersoy, Mr. Ertuğ Şimşek, Mr. Sedat Mert and Ms. Büşra Erdoğan are gratefully acknowledged.

TABLE OF CONTENTS

LIST OF TABLES

TABLES

LIST OF FIGURES

FIGURES

LIST OF ABBREVIATIONS

ABBREVIATIONS

AC	Alternating current
BC	Boundary condition
CbM	Condition-based Monitoring
CMOS	Complementary metal oxide
CVD	Chemical vapor deposition
DC	Direct current
DETF	Double ended tuning forks
DOF	Degree of freedom
DUT	Device under test
EOM	Equation of motion
FEA	Finite element analysis
GPS	Global positioning system
IC	Integrated circuit
IR	Infrared radiation
MEMS	Microelectromechanical systems
MUMPS	Multi user MEMS processes
NEP	Noise equivalent power
NETD	Noise equivalent temperature difference
PDE	Partial differential equation
PID	Proportional integral derivative
PR	Photoresist
RF	Radio frequency
RRM	Rayleigh-Ritz method
SAW	Surface acoustic wave
SCPI	Standard commands for programmable instruments
SCS	Single crystal silicon

SOI	Silicon on insulator
TCF	Temperature coefficient of frequency
TEC	Thermoelectric cooler
TED	Thermoelastic damping
TFBAR	Thin film acoustic resonator
TIA	Transimpedance amplifier
UHF	Ultra high frequency
UV	Ultraviolet

LIST OF SYMBOLS

SYMBOLS

E	Modulus of elasticity of Silicon
ρ	Density of Silicon
ν	Poisson's ratio of Silicon
α_{Si}	Thermal expansion coefficient of Silicon
α_{SiO_2}	Thermal expansion coefficient of Silicon dioxide
a, b	Side length of the plate in x and y directions
t	Side length of the cutout
l	Position of the cutout from the corner
h	Thickness of the plate
D	Flexural rigidity of the plate
g	Gap between electrodes and plate
w	Transverse displacement of the plate
W	Nondimensional transverse displacement of the plate
W_0	Nondimensional maximum transverse displacement
$T^*_{\max}$	Nondimensional maximum reference kinetic energy
$U_{\max}$	Nondimensional maximum strain energy
R_f	Feedback resistance of the transimpedance amplifier
ε_0	Dielectric permittivity of vacuum
σ_{xx}, σ_{yy}	Normal stresses in x and y directions
$\varepsilon_{xx}, \varepsilon_{yy}$	Normal strains in x and y directions
$\sigma_{xy}, \varepsilon_{xy}$	Shear stress and strain in xy plane
∇^2	Laplacian operator
∇^4	Biharmonic operator

CHAPTER 1

INTRODUCTION

Miniaturization has long been desired since the beginning of the 20th century due to undeniable advantages. Miniature devices are produced using fewer chemicals and raw materials thanks to taking up less space. In parallel, size of production devices decreases considerably along with area of manufacturing premises. Therefore, mass production of relatively little structures is considered as easier, economical and more precise compared to huge ones. However, it is obvious that as the number of process steps increases, so the complexity of production machines. In his famous talk, Richard Feynman addresses the issue regarding power consumption of electronic devices stemming from desire to have computers perform qualitative tasks and points out smaller computer elements as the only promising solution[1]. Fundamentally, micro devices facilitate both information processing and data storage by virtue of low power and material consumption. In the modern world, huge stacks of information are required to be stored and handled daily. Such demanding daily tasks are not likely to be completed without marvels of miniaturization.

Computers before the invention of transistors made use of thousands of vacuum tubes and complex electronic components to complete simple tasks. Nonetheless, reliability of these devices is considered low because of long time of troubleshooting, even sometimes surpassing operational time[2]. With the development of the point contact transistor in 1947, expectation for the revolution in electronics has arisen but not completed. Undoubtedly one of the cornerstones of miniaturization has been initiated in electronics with the invention of integrated circuit by Jack Kilby in 1958. Nevertheless, monolithic integrated circuit demonstrated in 1959 by Robert Noyce is sometimes regarded as the first true IC rather than hybrid IC proposed by Jack

Kilby[3]. Single crystal silicon is the main semiconductor element of ICs because band gap of the silicon atom is larger than that of germanium. Apart from electrical properties, silicon is favorable thanks to its mechanical properties which are comparable to steel in terms of Young's modulus and yield strength. Another important property of the silicon is being convenient for mass production of ICs as silicon dioxide and silicon nitride, which are strong insulators, is feasible to put on ICs with several methods.

Under the influence of IC fabrication methods, micromechanical structures are integrated into microelectronics, leading to microelectromechanical systems (MEMS). The idea behind MEMS is to manufacture small mechanical systems which are controlled and monitored by micro electronic devices. One of the examples of the earliest MEMS sensors is an isotropic micromachined piezoresistive diaphragm designed by Honeywell in 1962[4]. Aim of this MEMS sensor is to measure pressure with the help of piezoresistive effect caused by pressure difference on the diaphragm. Another example of the earliest MEMS device is resonant gate resistor developed by Harvey Nathanson in 1965. Resonant gate transistor is aimed to serve as a tuner for microelectronic radios. Nathanson is well-known not only for its MEMS device but also for the method of serial production in which layers of insulator, metal and silicon are deposited via masks on silicon wafers is still prevailing today[5]. With the help of improvement towards batch production of MEMS devices, commercialization of MEMS sensors is rationalized.

Dimensions of MEMS devices usually range from several micrometers to ten millimeters. However, basic miniature designs of macroscale mechanical systems are not plausible because of scaling effect, which is considered as a tool to design MEMS sensors rather than a hindrance. Relative weights of physical effects in microscale are completely different than those in macroscale. For instance, electrostatic actuation becomes practical in microscale while rapid heat transfer prohibits us from using mechanisms like internal combustion engines. Similarly, common mechanical designs like gears, joints and wheels are not practical due to

huge energy losses caused by friction[6]. Therefore, some microscale devices perform better than their macroscale counterparts. Moreover, microscale structures are faster and more sensitive to the environment compared to macroscale structures. If a cantilever beam is to shrink to a tenth of its dimensions, resonance frequency of the beam increases a hundred times while sensitivity to mass change rises a ten thousand-fold[7].

MEMS devices are appropriate to the market thanks to low cost of production and outstanding performance. Worth of the MEMS market has reached to US$13.4 billion in 2020 and it is expected to continue growing and reach US$18.2 billion by 2026. The most eminent MEMS products are certainly microphones, inertial and optical sensors[8]. Optical MEMS sensors are utilized to monitor and record wavelengths of interest. Infrared radiation (IR) is one of the most studied electromagnetic waves, wavelength of which starts approximately from 700nm and ends at 1mm, due to its practical applications in various industries, e.g., meteorology, electronics repair, aerospace industry and nondestructive testing.
In this chapter, MEMS resonators will be discussed briefly along with their application as temperature sensors and IR sensing. Then, research objectives and organization of the thesis are presented.

1.1 Resonators

Fundamentally timekeeping has been achieved through observing periodic physical phenomena such as movement of celestial bodies, oscillation of a quartz crystal under periodic voltage difference. Resonators keep track of time by vibrating at resonance frequency around which amplitude of the response is greater than that of the other frequencies. Several clocks utilizing different principles of physics in order to measure time present in the modern world. Atomic clocks and oven stabilized quartz crystal oscillators are among the best performing clocks. Specifically, atomic clocks are right now the most precise timekeepers in the world. Even unit of the time, second, is defined in terms of hyperfine transition frequency of cesium atoms, i.e.,

cesium atomic clocks, by International Bureau of Weights and Measures[9]. Other than timekeeping, these devices provide synchronizer signals for digital operations and are thus key components of integrated circuits and electronic devices. An accurate and precise frequency reference in an integrated circuit is a vital element for successful digital operations. However, atomic clocks and oven stabilized quartz oscillators are not preferable due to their huge size, cost and high-power consumption. Thus, alternative frequency references such as quartz resonators, thin film bulk acoustic resonators (TFBARs) and surface acoustic wave (SAW) resonators are preferred as high-quality signal providers for different kind of circuits including RF filters, GPS receivers and mobile devices. For instance, ability and speed of a mobile device to find its position is directly affected by quality of reference frequency source[10].

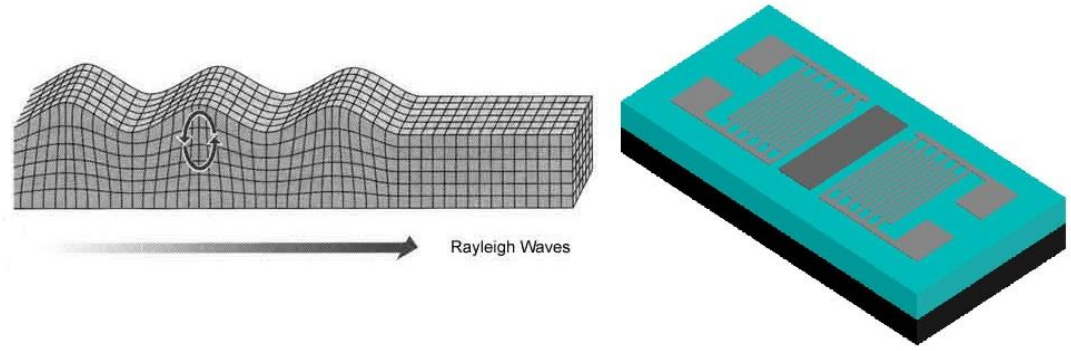

Figure 1.1. Surface acoustic wave and a simple 2-port SAW device

Recently, there has been an attempt to replace piezoelectric resonators with MEMS resonators because they are produced outside of the chip, later placed in a special cavity package and wire bonded to ICs. On the other hand, MEMS oscillators make use of process steps similar to complementary metal oxide semiconductors (CMOS) technology and is therefore readily capable of being integrated to production of ICs. With the elimination of an off-chip component, production cost of ICs is further decreased. Nevertheless, MEMS resonators still require further research and development to match key resonator figures of merit for such as quality factor (Q-factor), resonance frequency and temperature stability. Quality factor is simply defined as ratio of initial energy to energy lost in one cycle of oscillation. Narrow

band filtering of the oscillator noise and low phase noise is direct result of having high Q-factor. Over the past decades, it has been proven that MEMS resonators are capable of having high Q-factor in GHz regime with different kind of designs and materials[11].

1.1.1 Types of resonators and their performances

Different kinds of resonator designs and materials has been extensively studied in the literature stemming from macro structures like beams, plates and shells. Beam resonator is by far the most prevalent resonator design due to its simple geometry and analytical model. Quality factors exceeding 8,000 over a frequency range of 30-90 MHz has been demonstrated with a free-free beam vibrating at flexural mode by making small changes in design parameters[12]. In this study, supports of the free-free (F-F) beam attached from nodal points in order to minimize anchor loss. With a robust design and appropriate temperature compensation, F-F beams are shown to be capable of achieving Q-factors up to 16,000 with 70 MHz frequency[13]. It has been reported that higher quality factors are reachable with further miniaturization. For instance, Q-factor of 177,000 around 19 kHz resonance frequency is attainable in vacuum with clamped-free beam[14]. Nevertheless, such a beam requires special production techniques to form high aspect ratio submicron gaps.

Similar to beam resonators, folded beam resonators with capacitive comb drive and sense pads have been extensively studied. A completely CMOS compatible folded beam resonator with Q=51,000 where resonance frequency is approximately 18 kHz has been demonstrated[15]. Integrating production procedure into CMOS process flow is one of the most desired properties of microresonators because CMOS is already well-established process flow utilized to mass produce microelectronics. Another such important design is definitely double-ended tuning forks (DETF) resembling design of the folded beams. DETF resonators are regarded best for low frequency applications which need high Q-factor. An DETF resonator with quality factor of 80,000 at 154 kHz frequency has been achieved in 4 mTorr vacuum[16].

Moreover, this DETF resonator is manufactured using a standardized process flow named SOI MUMPs developed by MEMSCAP.

An interesting design is the use of plates as resonator. Several quality factors ranging from 800 to 1900 has been reported with F-F-F-F square plate resonators excited in one of the flexural modes[17], [18]. Having been produced with CMOS-MEMS is impressive for such resonators centered around 6.52 MHz. A riveting solution has been tested in another article. Instead of four tethers attached to plate from each corner, a cylindrical anchor is connected to plate from its center, where nodal lines intersect. Q=15 000 centered at 68.5 MHz has been demonstrated with a 16 ×16 μm center-stem square plate under high vacuum[19].

Unfortunately, different loss mechanisms become dominant with increasing resonance frequency and nanometer dimensions. While Akhiezer damping limits the resonance frequency in ultra-high frequency (UHF) region, thermoelastic damping (TED) is considered the main source of losses in submicron domain[20]. In order not to encounter such loss mechanisms, bulk mode vibrations are preferred over flexural modes in micrometer domain due to two key advantages. Resonance frequencies of bulk modes are high because their structural stiffnesses are larger and bulk modes yield higher Q-factors compared to flexural modes owing to less surface energy loss[21]. To illustrate, a square plate resonator reaching 3.7 million quality factor at 5.16 MHz has been accomplished with only single crystal silicon (SCS) manufactured via SOI MUMPs[22]. In this study, stems are aligned with nodal lines to shrink anchor losses and square plate is excited in contour mode inside a high vacuum chamber to attain high Q-factor. Similar to the previous square plate resonator, a polydiamond disk resonator vibrating in contour mode has been reported to exhibit a stunning quality factor of 10,100 at 1.5 GHz resonance frequency without vacuum[23]. However, deposition of polydiamond remains as a drawback for this resonator design since it requires chemical vapor deposition (CVD) at 800 ˚C and special process steps.

1.2 Resonant temperature & IR sensors

Resonators are considered to be already part of the digital electronics since they are capable of providing discrete signals. Moreover, their high stability is indispensable for sensor applications. Therefore, advantage of resonant sensors in digital electronics cannot be ignored.

Although there are well-established thermocouple, resistance and thermistor temperature sensors, resonant temperature sensors have been developed and tested. AuPd microresonator beam, which is electrostatically actuated, has been reported to have a responsivity of 164 Hz/K with a massive Q-factor~10^5[24]. Furthermore, Pandey reports a temperature rise per incident laser of 3 K/mW, implying noninvasive temperature measurement is achievable through infrared radiation sensing. A DETF mechanism with a quality factor of 10,000 and frequency of 1.3 MHz has been shown to have a -1.4×10^{-3} V/˚C sensitivity and resolution of 0.002 ˚C[25]. In this article, root mean square (RMS) detector is attached to output of oscillator to improve temperature resolution of the resonator. An outstanding resonator temperature sensitivity has been reported as -3.7 kHz/˚C for beam mechanism with Q=5,000 at f=10.7 MHz[26].

IR sensors are usually divided into two groups: photon and thermal detectors. Even though photon detectors are superior in terms of sensitivity and speed, they require cryogenic cooling. In photon detectors, absorbed photon excite electron to conduction band or vice versa. Low operation temperature is attributed to desire of longer wavelength sensitivity to suppress noise and close energy levels[27]. Therefore, thermal detectors have been widely studied to eliminate costly cryogenic cooling.

As previously stated, incident infrared radiation on a surface causes temperature change. There have been several attempts to utilize this temperature change and sense infrared radiation. For instance, a miniature resonator tuning fork mechanism is designed for IR sensing. An absorber area between branches is manufactured from

p++ doped silicon. Incident IR causes temperature change which is detected by tuning fork mechanism. Responsivity of 120 ppm/μW has been demonstrated for this design[28]. According to Cabuz et al., key point of developing highly sensitive microresonator sensor is to have small thermal mass and high thermal resistance, which are accomplishable with MEMS. AIN microresonator plate is demonstrated to have TCF of -26.9 ppm/K and noise equivalent power (NEP) of -20 $nWHz^{-1/2}$ at 3.4 μm wavelength[29]. NEP is one of the most important parameters for IR sensing and defines signal-to-noise ratio for infrared thermography. In this article, graphene is chosen as electrode rather than metals in order not to cause decline in Q-factor since it is well-known metal electrodes are one of the most prominent energy loss mechanism in piezoelectric resonators.

1.3 Research objectives

Application area of MEMS has been expanding since its invention due to obvious reasons such as low cost of production, being suitable to mass production and taking up less space compared to old fashioned mechanical counterparts. With the rise of information technologies, demand for MEMS sensors is expected to grow exponentially[30]. These sensors are utilized to continuously monitor condition of mechanical systems and plan maintenance schedule of the mechanism. However, the first condition necessary to achieve such a condition-based monitoring (CbM) is to achieve inexpensive sensor technologies. As previously explained IR sensing photonic detectors are both cumbersome to manufacture and operate because of cryogenic cooling. In this thesis, a plate mechanism with adjustable resonance frequency is developed to demonstrate that plate resonators are one of the promising microbolometers for temperature and IR sensing. The main objectives of this thesis are:

1. To develop an array of microplate resonators with adjustable resonance frequency. Resonance frequencies of microplates are accomplished through cutout with unique position placed on microplates.

2. To derive an analytical model of the microplate resonators with cutouts for the first and second modes using Rayleigh-Ritz method since these two modes are the ones with smaller resonance frequency and higher displacement of the body. In the literature, cantilever plates are widely studied as sensors along with simply supported plates. There are few articles regarding F-F-F-F plate resonators but none of them proposes adjustment of resonance frequency. Electrostatic actuation and sense of the plate is simulated as parallel plates. Thermal effects on the plate vibration are modelled with the help of simple thermal expansion formula.
3. To verify analytical model with finite element analysis (FEA). Comparison of results are illustrated with the graphs along with investigation into convergence of finite element model (FEM).
4. To fabricate designed pixel plates and address problems regarding microfabrication process flow. Microfabrication results are discussed and problems are identified.
5. Characterization of fabricated pixel and comparison of the performance metrics of designed and fabricated versions

1.4 Organization of the thesis

In this chapter, background information about MEMS, resonators and resonant sensors is provided along with a brief history. Advantages of miniaturization along with scaling effect is explained and then resonators with different designs and their performances are compared. Later, infrared radiation (IR) sensing is discussed with certain performance metrics.

In the second chapter, design of the microresonator plates is shown and later analytical model is developed for plate resonators with adjustable frequency. In analytical model, plate is assumed to be thin plate while effects of electrostatic spring softening and temperature change is included afterwards. Lastly, FEM is conducted to validate results calculated with analytical model.

In the third chapter, manufacturing steps of microresonator plates are briefly shown. Experimental setup consisting of network analyzer, vacuum chamber, power supplies and temperature sensor is introduced along with manufactured plates. Manufacturing flaws are determined and discussed shortly. Possible solutions to these errors are suggested. Frequency responses for different resonance frequency plates with different temperatures are graphed.

In the last chapter, results are discussed and some conclusions are deduced from experimental data. Comparison between analytical model and tests results are done. Work can be done in the future is pointed out

CHAPTER 2

DESIGN

Design and modelling of the square plate resonator with cutouts are explained in this chapter. Key terms of the plate vibration like nodal lines, resonance frequency and flexural modes are discussed in detail with a little look into history of the plate vibration. Later, equation of motion (EOM) of the plate is derived by making use of two approaches: equilibrium approach and variational approach. Then, Rayleigh-Ritz method is introduced in order to solve transverse vibration EOM of the plate. Effects of cutouts are modeled with the help of Rayleigh-Ritz method. After completing the mechanical model of the square plate resonator with cutouts, electrostatic drive and sense is modelled with exploitation of the simple capacitance formula. Effect of temperature on the resonance frequency is calculated via considering thermal expansion of the materials. Lastly, analytical model of the square plate with cutouts are verified through finite element analysis (FEA). Last section of this chapter summarizes the design and modelling of the square plate.

2.1 Fundamentals of transverse plate vibration

Classical mechanics is mainly divided into three branches: statics, dynamics and kinematics. While statics examines equilibrium of bodies by observing forces, dynamics studies motion of bodies and its relation to forces. On the other hand, examination of motion without any consideration of forces is called kinematics. Vibration is a physical phenomenon caused by repeated motion of the body around the equilibrium point and thus is modelled with the help of dynamics. Although vibration is unwanted in some devices like electric motors and internal combustion

engines since it wastes energy, it is completely desired in some mechanical systems like tuning forks.

Mechanical vibrations are divided into two types: free and forced. Free vibration occurs when an initial input sets system in motion and it repeats the motion while slowly decaying. On the other hand, a periodic or random disturbance keeps providing energy to the system. Although there are energy losses in the system, its motion is prolonged with the aid of energy input from disturbance. Energy losses in a vibrating system is taken into account by means of damping. In the absence of damping, mechanical vibrations are expected to last infinitely. Such an ideal system is called undamped and unfortunately non-existent in reality. Applying input disturbance at different frequencies to a mechanical system causes different displacement (from equilibrium point) responses for each frequency. The frequency at which the biggest displacement happens is called natural frequency. If a mechanical system is excited at natural frequency, the magnitude of displacement increases with each oscillation, thus resulting in structural damage. Natural frequency is alternatively worded as the frequency at which system tends to vibrate without any force.

Systems with damping are divided into three types, namely underdamped, critically damped and overdamped. While no oscillations are observed in critically damped and overdamped systems, movements slowly decay in underdamped systems. How gradually vibrations perish is completely dependent on damping ratio as the lower damping ratio is, the smaller energy loss is. Another important parameter for vibrating systems is quality factor, which is inversely proportional to damping ratio. As stated in the first chapter, the higher Q-factor results in longer oscillations since damping ratio decreases with rise in Q-factor. Underdamped systems exhibit maximum displacement at a frequency called resonance frequency rather than natural frequency. Even though resonance frequency is close to natural frequency, they are not the same. In order to attain peak displacement, an underdamped system is excited at resonance frequency.

The number of DOF of a system is simply defined by the minimum number of displacement components necessary to define shape and position of the body in the space. It is obvious that infinity number of displacement components are existent in a continuous body. One resonance frequency is present in a multi-DOF system for each degree of freedom. For example, a n-DOF system have n resonance frequencies. Consequently, an infinite number of DOF translates into infinite resonance frequencies. System vibrating at resonance frequency reveals unique forms related to its frequency. These unique forms are called mode shapes and they define relative displacement of each generalized coordinate. In other words, mode shapes are displacement patterns unique to each resonance frequency. Yet, there are some points on each mode shape called nodes, which don't move in anyway. Nodes become nodal lines in resonance of two-dimensional bodies separating the surface into different regions with opposite displacements. In the first half of the cycle, some regions move upwards whilst opposite regions move downwards. In the second half of the cycle, movement directions of regions are reversed. Subsequently, these nodal lines are one of the important parameters to distinguish modes from each other.

Mode shapes are keystone to understanding vibration since they also provide information regarding vibration characteristic of the system. Modes are mainly divided into three groups, which are flexural, bulk and torsional modes. Distinctive property of flexural mode is that bending is the predominant elastic deformation in vibrating body while torsional modes are identified by twisting motion. On the other hand, bulk modes display contraction and extraction of the body bringing about greater stiffnesses[31]. Most extensively studied square plate bulk modes are shown below[32].

Figure 2.1. Some bulk modes of the square plate

Square plate, which is a continuous medium, have infinite number of resonance frequencies, each exhibits unique mode shapes. Ernst Chladni, who is sometimes

labeled as father of acoustics, is one of the first people to study vibration of plates. In his phenomenal work, Ernst Chladni vibrates a square plate covered with sand using a violin bow in order to visualize nodal lines[33]. Nonetheless, these mode shapes found by Chladni are flexural ones since they categorize transverse displacement of a thin plate. Below figure illustrates flexural modes.

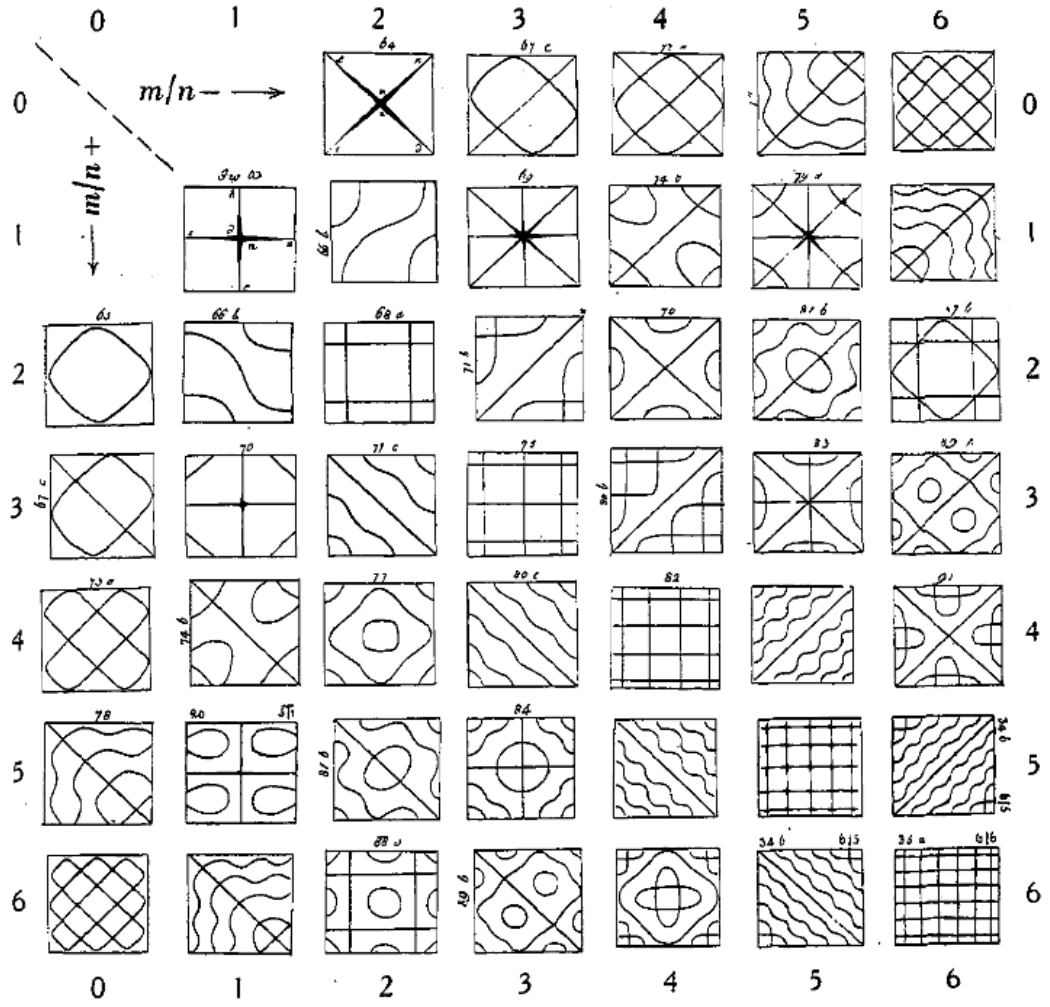

Figure 2.2. Chladni figures and naming convention

Waller is one of the scientists to repeat the experiments conducted by Chladni[34]. In her article, nodal patterns of the square plate are drawn and naming of the modes are shown as in Figure 2.2. Mode shapes in the lower triangle are labeled as (m,n)+(n,m) whilst mode shapes in the upper triangle are labeled as (m,n)-(n,m).

Modes on the diagonal lines are simply named (n,m) since n=m. However, not all of the modes are not noteworthy as the resonance frequency exceedingly grows with increasing modes. The first three modes are (1,1), (2,0)-(0,2) and (2,0)+(0,2) in order of the smallest resonance frequency to the largest resonance frequency. From now on, they are called 1st mode, 2nd mode and 3rd mode respectively in order to avoid further confusion.

2.2 Design of the square plate resonators with adjustable frequency

Square plate resonators with adjustable resonance frequency are proposed in this article, shown in Figure 2.3. Adjustment of the resonance frequency is achieved through changing positions of the diminutive square cutouts.

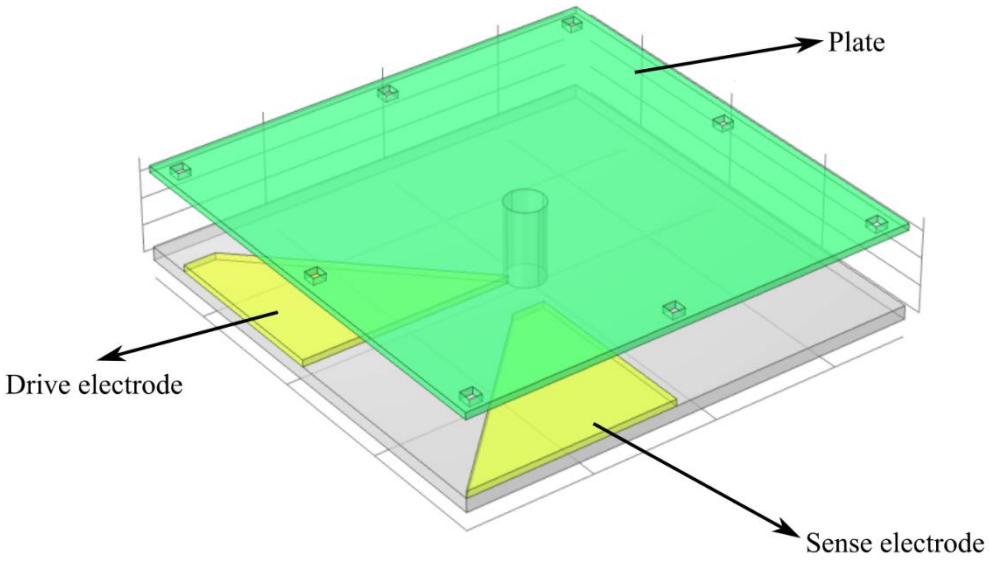

Figure 2.3. Plate resonator with adjustable frequency design

Anchor or plate post is placed at the center of the plate because of the fact that nodal lines of 1st and 2nd mode intersects at the center point. Thus, anchor loss while vibrating minimized since this point relatively stays motionless, increasing Q-factor of the plate resonator.

Cutouts are positioned on centerlines and diagonal lines since 1st and 2nd modes are either symmetric or antisymmetric with respect to center and diagonal lines. Changing positions of the cutouts on diagonals are anticipated to have huge effect on natural frequency of the 1st mode and less impact on that of the 2nd mode because cutouts are on the nodal lines of the 2nd mode. To contrary, cutouts on center lines are anticipated to have huge effect on natural frequency of the 2nd mode and less impact on that of the 1st mode since cutouts are on the nodal line of the 2nd mode.

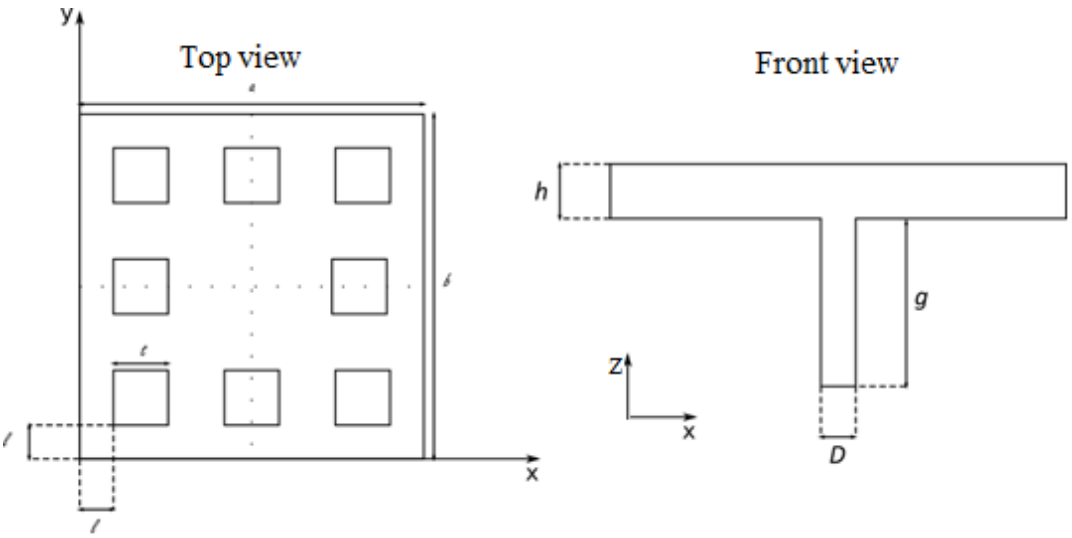

Figure 2.4. L-plate design parameters of the plate

Above figure illustrates the parameters of the plate design. Dimensions of the cutouts are exaggerated so that they are visible on the drawing. Note that there are two different kind of plate designs. While both of these plate designs with cutouts share the same thickness, side length, size of the cutouts, only number of cutouts are different. Design of the plate with 8 cutouts is called L-plate. On the other hand, design of the plate with 4 cutouts is named K-plate and shown in the Figure 2.5. Effects of the cutouts on L-plates are expected to be greater compared to K-plate due to cutouts comprising larger portion of the microplate resonator.

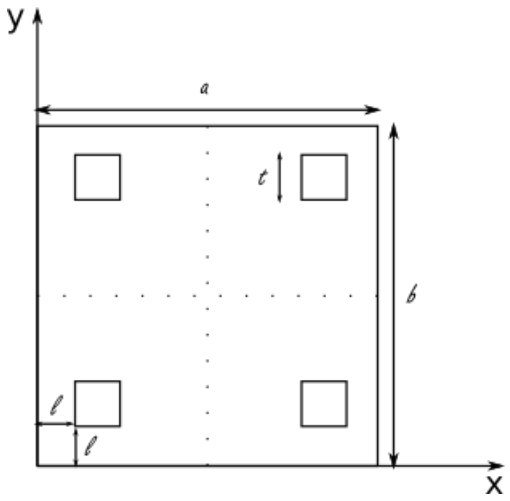

Figure 2.5. K-plate design

In this study, capacitive actuation and detection mechanisms are used to excite and sense vibration of plates. Drive and sense pads of the plate are deposited gold metal shown as yellow in Figure 2.3. Plate is produced from single crystal silicon wafer, face of which is (111) plane. Plates are attached to substrate which is SiO_2 glass in order to prevent short circuit between electronic components.

Capacitive actuation and detection are selected in this design because of the fact that deposition of lossy mediums on resonator mechanism is not necessary in this type of actuation and detection unlike it is necessary for the piezoelectric ones. Details of the electrode design are not provided here but they are simple trapezoidal electrodes with 45° side angles, symmetric with respect to anchor positioned at the center of the plate. One of them is used for driving plate resonator while other one is utilized to capture induced current by capacitive sensing. Sensed current is later fed to a transimpedance amplifier (TIA) to convert it to voltage. Feedback resistance of the transimpedance amplifier is chosen as $R_f = 1\mathrm{M}\Omega$ so that output is also amplified to facilitate sensing of the resonance frequency.

Table 2.1 Design parameters

Design parameter	*Value*
Side length of the plate resonator – *a* & *b*	360 µm
Side length of the cutouts – *t*	10 µm
Position of cutouts – *l*	0, 10, 20…, 140 µm
Thickness of the plate – *h*	1.61 µm
Diameter of the anchor – D_{anchor}	30 µm
Capacitive gap – *g*	10 µm

Geometric properties of the plate with adjustable frequency are summarized in above table. In order to develop analytical model of the plate, some of the mechanical and thermal properties of materials are necessary. Since materials are widespread in MEMS field, necessary properties are found in the literature.

Table 2.2 Mechanical and thermal properties of the materials

Property name	*Value*
Modulus of elasticity of (111) SCS[35] – E	168.9 GPa
Density of Si[36] – ρ	2330 kg/m^3
Poisson's ratio of (111) SCS[37] – ν	0.262
Thermal expansion coefficient of Silicon[38] – α_{Si}	$2.63\times10^{-6}\,K^{-1}$
Thermal expansion coefficient of SiO_2[39] – α_{SiO2}	$5.6\times10^{-7}\,K^{-1}$
Thermal coefficient of E of Silicon[40] – α_E	$-60\times10^{-6}\,K^{-1}$

2.3 Equation of motion of the thin plate

Most widely studied structural elements are undoubtedly beams, plates and shells due to generality. Although Chladni travelled the Europe and demonstrated his famous experiment, he wasn't able to explain these patterns. Sophie German is one of the first individual to formulate these patterns with differential equations along some errors regarding hypothesis and boundary conditions[41]. The correct way to formulate transverse displacement of the thin plate comes from similarity to thin beam. Euler-Bernoulli beam theory explains load carrying capacity and deflection characteristics of beams undergoing small deflections with the following assumption: a straight line normal to beam axis before bending remains (1) straight, (2) nonextensile and (3) perpendicular to the beam axis even after deformation. Later, Euler-Bernoulli theory is extended to thin plates by Kirchhoff and Love[42]. Hence, classical plate theory (CPT), describing stresses and deformations in thin plates, is sometimes called Kirchhoff-Love plate theory. Assumptions of Kirchhoff-Love plate theory is listed below.

1 Lateral dimensions of the plate are greater than its thickness.

2 The material of the plate is homogenous, isotropic and linear elastic. In other words, it abides Hooke's law.

2 The mid-surface does not undergo in-plane deformation, implying the mid-surface is a neutral plane and remains as it is.

3 Thickness of the plate is far larger than its transverse deflection.

4 Straight lines perpendicular to the mid-surface before deformation stays perpendicular and straight after deformation. Accordingly, effects of transverse shear deformation are neglected.

5 The effect of rotary inertia is not considered throughout the derivation.

Even though Kirchhoff-Love plate theory is sufficient for thin plates, it still lacks necessary means to explain stresses and deformations in thick plates and thin plates

vibrating at higher modes. Timoshenko beam theory is an extended version of the Euler-Bernoulli beam theory incorporating both the effects of transverse shear and rotary inertia[43]. Correspondingly, plate vibration taking the effects of shear deformation and rotary inertia has been published[44], [45]. However, these theories are irrelevant to designed plates since plates are very thin and not excited at higher modes.

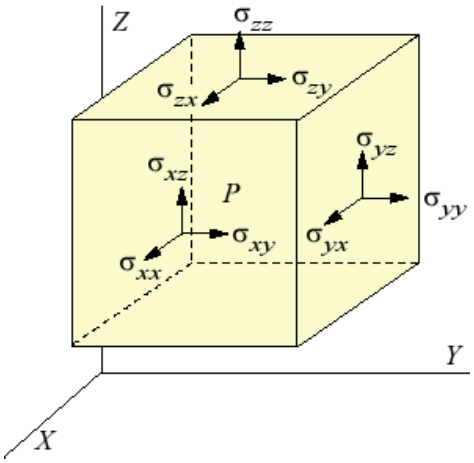

Figure 2.6. Three-dimensional stress element

First of all, look at the stress element shown in Figure 2.3. Despite the fact that 15 stresses are present in 3D stress element, only 6 stresses are unique. Further simplification is achieved through either plane strain or plane stress of theory of elasticity. However, these two types of assumptions are not suitable for the thin plate case. Thin plate is not constrained from both upper and lower boundaries, making plain strain inappropriate. On the other hand, plane stress necessitates all stress elements linked to z axis are zero, i.e., σ_{zz}, σ_{xz} *and* σ_{yz}. However, plates carry loads by means of moments and shear forces rather than in-plane tensions as in the case of membranes. Therefore, only normal stress in z direction chosen to be neglected so that shear forces are existent.

$$\begin{aligned} u &= u(x, y) \\ v &= v(x, y) \\ \sigma_{zz} &= 0 \end{aligned} \tag{2.1}$$

With the above assumptions, linear relations between displacements of small plate element are explicitly published in the literature[46].

$$u = -z\frac{\partial w}{\partial x}$$
$$v = -z\frac{\partial w}{\partial y} \tag{2.2}$$

Where $u, v \text{ and } w$ represents displacements in the x, y and z directions, respectively. In the same book, linear strain-displacement relations are derived by Timoshenko.

$$\varepsilon_{xx} = \frac{\partial u}{\partial x}$$
$$\varepsilon_{yy} = \frac{\partial v}{\partial y} \tag{2.3}$$
$$\varepsilon_{xy} = \frac{\partial u}{\partial y} + \frac{\partial v}{\partial x}$$

$\varepsilon_{xx} \text{ and } \varepsilon_{yy}$ are normal strains parallel to x and y axes while ε_{xy} is the shear strain in the xy plane.

Replacing displacements in linear strain-displacement equations with equations (2.2) in order to express strains in terms of transverse displacement.

$$\varepsilon_{xx} = -z\frac{\partial^2 w}{\partial x^2}$$
$$\varepsilon_{yy} = -z\frac{\partial^2 w}{\partial y^2} \tag{2.4}$$
$$\varepsilon_{xy} = -2z\frac{\partial^2 w}{\partial x \partial y}$$

Then strains and stresses are related by using Hooke's law.

$$\sigma_{xx} = \frac{E}{1-\nu^2}\varepsilon_{xx} + \frac{\nu E}{1-\nu^2}\varepsilon_{yy} = -\frac{Ez}{1-\nu^2}\left(\frac{\partial^2 w}{\partial x^2} + \nu\frac{\partial^2 w}{\partial y^2}\right)$$
$$\sigma_{yy} = \frac{E}{1-\nu^2}\varepsilon_{yy} + \frac{\nu E}{1-\nu^2}\varepsilon_{xx} = -\frac{Ez}{1-\nu^2}\left(\frac{\partial^2 w}{\partial y^2} + \nu\frac{\partial^2 w}{\partial x^2}\right) \qquad (2.5)$$
$$\sigma_{xy} = G\varepsilon_{xy} = -\frac{Ez}{1+\nu}\frac{\partial^2 w}{\partial x \partial y} \quad where \quad G = \frac{E}{2(1+\nu)}$$

Now strain-stress relations are constituted where ν is Poisson's ratio and E is Young's modulus of the isotropic material.

Consider the plate element, mid-plane of which coincides with xy-plane, given below. While M_x and M_y denote bending moments, M_{xy} designates twisting moment. Shear forces are represented by Q_x and Q_y.

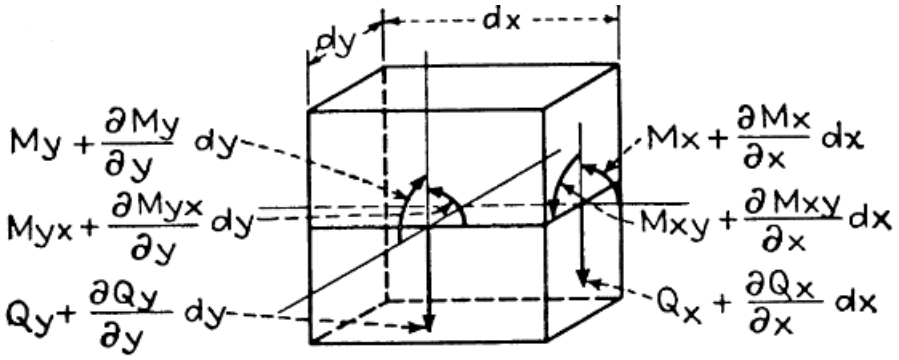

Figure 2.7. A plate element showing forces and induced moment resultants

At the edges, the plate is free to move and strain of the mid-plane is assumed to be negligible. Thus, reactive forces at the edges are normal to the plate and zero.

$$\int_{-h/2}^{h/2} \sigma_{xx} dz = 0$$
$$\int_{-h/2}^{h/2} \sigma_{yy} dz = 0 \qquad (2.6)$$

Bending and twisting moment intensities per unit length are defined.

$$M_x = \int_{-h/2}^{h/2} \sigma_{xx} dz \;\; and \;\; M_y = \int_{-h/2}^{h/2} \sigma_{yy} dz$$
$$M_{xy} = M_{yx} = \int_{-h/2}^{h/2} \sigma_{xy} dz \;\; as \;\; \sigma_{xy} = \sigma_{yx} \tag{2.7}$$

Similar to moment intensities, shear force intensities per unit length are defined below.

$$Q_x = \int_{-h/2}^{h/2} \sigma_{xz} dz \;\; and \;\; Q_y = \int_{-h/2}^{h/2} \sigma_{yz} dz \tag{2.8}$$

Mid-plane of the plate with only force intensities per unit length is drawn below.

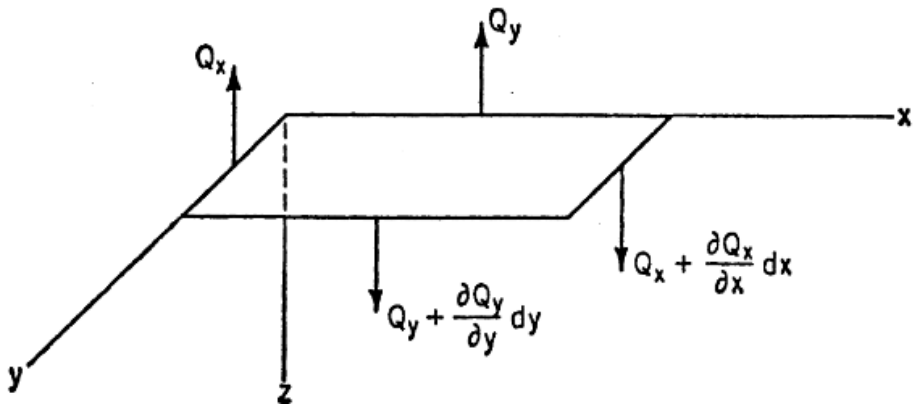

Figure 2.8. Force equilibrium

Multiplying shear force intensities by length results in forces. Force equilibrium in z direction is written.

$$\left(Q_x + \frac{\partial Q_x}{\partial x} dx\right) dy + \left(Q_y + \frac{\partial Q_y}{\partial y} dy\right) dx - Q_x dy - Q_y dx = dM \frac{\partial^2 w}{\partial t^2} - q dx dy \tag{2.9}$$

Where dM is infinite small mass and q is the force distributed over the plate.

Performing multiplication, addition and subtraction operations and simplifying equation.

$$\frac{\partial Q_x}{\partial x} dxdy + \frac{\partial Q_y}{\partial y} dxdy = dM \frac{\partial^2 w}{\partial t^2} - qdxdy \tag{2.10}$$

Substituting infinite small mass with density times volume. Volume is thickness of the plate times infinite small plate area.

$$\frac{\partial Q_x}{\partial x} + \frac{\partial Q_y}{\partial y} = \rho h \frac{\partial^2 w}{\partial t^2} - q \tag{2.11}$$

When only the moment intensities are shown on the plate, it is easier to write moment equilibrium equations.

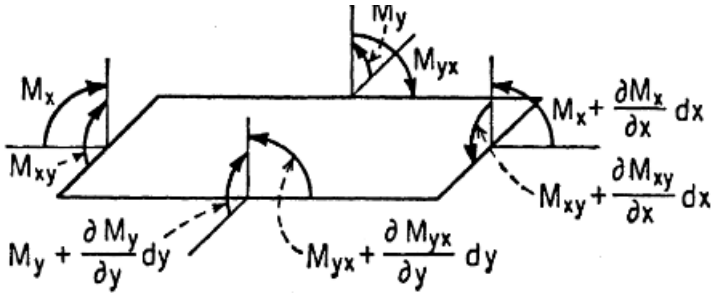

Figure 2.9. Only moment intensities acting on the plate

Writing moment both moment equilibriums about x axis and y axis and simplifying equations.

$$\begin{aligned} \frac{\partial M_{xy}}{\partial x} - \frac{\partial M_y}{\partial y} + Q_y = 0 \\ \frac{\partial M_{yx}}{\partial y} + \frac{\partial M_x}{\partial x} - Q_x = 0 \end{aligned} \tag{2.12}$$

Solving moment equilibrium equations for Q_x and Q_y and substituting results into force equilibrium equation.

$$\frac{\partial^2 M_x}{\partial x^2} - 2\frac{\partial^2 M_{xy}}{\partial x \partial y} + \frac{\partial^2 M_y}{\partial y^2} = \rho h \frac{\partial^2 w}{\partial t^2} - q \tag{2.13}$$

In order to get moments in terms of displacements, bending and twisting moment intensity integrals, given in equations (2.7), are calculated.

$$\begin{aligned} M_x &= -D\left(\frac{\partial^2 w}{\partial x^2} + \nu \frac{\partial w^2}{\partial y^2}\right) \\ M_y &= -D\left(\frac{\partial^2 w}{\partial y^2} + \nu \frac{\partial w^2}{\partial x^2}\right) \\ M_{xy} &= -D(1-\nu)\frac{\partial^2 w}{\partial x \partial y} \\ Q_x &= -D\frac{\partial}{\partial x}\left(\frac{\partial^2 w}{\partial x^2} + \frac{\partial w^2}{\partial y^2}\right) \\ Q_y &= -D\frac{\partial}{\partial y}\left(\frac{\partial^2 w}{\partial x^2} + \frac{\partial w^2}{\partial y^2}\right) \end{aligned} \tag{2.14}$$

Where D is defined as flexural rigidity of the plate, similar to flexural rigidity of a beam $D = EI$.

$$D = \frac{Eh^3}{12\left(1-\nu^2\right)} \tag{2.15}$$

Inserting equations (2.14) into equation (2.13) results in EOM of transverse vibration of the plate.

$$D\nabla^4 w + \rho h \frac{\partial^2 w}{\partial t^2} = q \tag{2.16}$$

Note that ∇^4 is called biharmonic operator and it is square of the Laplacian operator.

$$\begin{aligned} \nabla^2 &= \frac{\partial^2}{\partial x^2} + \frac{\partial^2}{\partial y^2} \\ \nabla^4 &= \nabla^2\nabla^2 = \frac{\partial^4}{\partial x^4} + 2\frac{\partial^2}{\partial x \partial y} + \frac{\partial^4}{\partial y^4} \end{aligned} \tag{2.17}$$

Similar to the Laplacian operator, biharmonic operator is encountered in diverse areas such as continuum mechanics, linear elasticity and fluid mechanics.

Even though EOM of the transverse vibration of the thin plate is already derived, derivation with variational method is shown below as energy equations are employed while calculating natural frequency of the plate.

Kinetic energy of the plate is found by integrating kinetic energies of every particle over the plate surface area, which is denoted with R.

$$T = \frac{1}{2}\iint_R \rho h \left(\frac{\partial^2 w}{\partial t^2}\right)^2 dxdy \tag{2.18}$$

Potential energy due to distributed load q on the plate is formulated.

$$V = -\iint_R qw dxdy \tag{2.19}$$

Strain energy of the plate is calculated with a similar approach to kinetic energy. However, stress elements including z terms are neglected by virtue of plane stress assumption. Integration of strain energy over volume leads to following equation.

$$U = \frac{1}{2}\iint_R \left[\int_{-h/2}^{h/2} \left(\sigma_{xx}\varepsilon_{xx} + \sigma_{yy}\varepsilon_{yy} + \sigma_{xy}\varepsilon_{xy}\right)dz\right] dxdy \tag{2.20}$$

Inserting strain stress relation given in equations (2.5) into equation (2.20).

$$\begin{aligned} U = \frac{1}{2}\iint_R \Bigg[\int_{-h/2}^{h/2} &\frac{E}{\left(1-\nu^2\right)}\left(\varepsilon_{xx} + \nu\varepsilon_{yy}\right)\varepsilon_{xx} + \frac{E}{2(1+\nu)}\varepsilon_{xy}{}^2 \\ &+ \frac{E}{\left(1-\nu^2\right)}\left(\varepsilon_{yy} + \nu\varepsilon_{xx}\right)\varepsilon_{yy} dz\Bigg] dxdy \end{aligned} \tag{2.21}$$

Performing algebraic operations and simplifying above equation.

$$U = \frac{1}{2}\iint_R \left[\int_{-h/2}^{h/2} \varepsilon_{xx}{}^2 + \varepsilon_{yy}{}^2 + 2\left(1-\nu\right)\varepsilon_{xy}{}^2 + 2\nu\varepsilon_{xx}\varepsilon_{yy} dz\right] dxdy \tag{2.22}$$

Similarly, inserting strain displacement relations of equations (2.4) into equation (2.22).

$$U=\frac{E}{2(1-\nu^2)}\iint_R\left[\int_{-h/2}^{h/2}\left(\frac{\partial u}{\partial x}-z\frac{\partial^2 w}{\partial x^2}\right)\varepsilon_{xx}+\left(\frac{\partial u}{\partial y}-z\frac{\partial^2 w}{\partial y^2}\right)\right.$$
$$+2(1-\nu)\left(\frac{1}{2}\left(\frac{\partial u}{\partial y}+\frac{\partial v}{\partial x}\right)-z\frac{\partial^2 w}{\partial x\partial y}\right)^2 \qquad (2.23)$$
$$\left.+2(1-\nu)\left(\frac{\partial u}{\partial x}-z\frac{\partial^2 w}{\partial x^2}\right)\left(\frac{\partial v}{\partial x}-z\frac{\partial^2 w}{\partial y^2}\right)\right]dzdxdy-\iint_R qwdxdy$$

With the help of simplification, total strain energy of the plate is written.

$$U=\frac{D}{2}\iint_R\left[\left(\nabla^2 w\right)^2-2(1-\nu)\left(\frac{\partial^2 w}{\partial x^2}\frac{\partial^2 w}{\partial y^2}-\left(\frac{\partial^2 w}{\partial x\partial y}\right)^2\right)\right]dxdy$$
$$-\iint_R qwdxdy \qquad (2.24)$$

In order to apply Hamilton's principle, a functional called Lagrange is defined.

$$L=\frac{1}{2}\iint_R\left[D\left\{\left(\nabla^2 w\right)^2-2(1-\nu)\left(\frac{\partial^2 w}{\partial x^2}\frac{\partial^2 w}{\partial y^2}-\left(\frac{\partial^2 w}{\partial x\partial y}\right)^2\right)\right\}-2qw\right.$$
$$\left.-\rho h\left(\frac{\partial^2 w}{\partial t^2}\right)^2\right]dxdy \qquad (2.25)$$

According to Hamilton's principle, change of the system between two specified states at two specified times t_1 and t_2 is a stationary point of the functional called Lagrange.

$$\delta\int_{t_1}^{t_2}\left(T-U\right)dt=\delta\int_{t_1}^{t_2}Ldt=0 \qquad (2.26)$$

Substituting defined functional into equation (2.26).

$$\delta\int_{t_1}^{t_2}\iint_R\left[\frac{D}{2}\left\{\left(\nabla^2 w\right)^2-(1-\nu)\left(\frac{\partial^2 w}{\partial x^2}\frac{\partial^2 w}{\partial y^2}-\left(\frac{\partial^2 w}{\partial x\partial y}\right)^2\right)\right\}-2qw-\frac{\rho h}{2}\frac{\partial^2 w}{\partial t^2}\right]dxdydt \tag{2.27}$$

Applying variation operator to inside of the integral.

$$\int_{t_1}^{t_2}\iint_R\Big[D\left\{\left(\nabla^2 w\right)\left(\nabla^2\delta w\right)-(1-\nu)\left(\frac{\partial^2\delta w}{\partial x^2}\frac{\partial^2 w}{\partial y^2}+\frac{\partial^2 w}{\partial x^2}\frac{\partial^2\delta w}{\partial y^2}-2\left(\frac{\partial^2 w}{\partial x\partial y}\right)\frac{\partial^2\delta w}{\partial x\partial y}\right)\right\}-2q\delta w-\frac{\rho h}{2}\frac{\partial^2 w}{\partial t^2}\frac{\partial^2\delta w}{\partial t^2}\Big]dxdydt \tag{2.28}$$

Further simplification of the above equation is possible with Green's theorem and it is a long algebraic expression to write down. Fortunately, it is already completed and shown in the literature[47]. Simplified integral is written below.

$$\int_{t_1}^{t_2}\left[\iint_R\left(-\rho h\frac{\partial^2 w}{\partial t^2}-D\nabla^4 w+q\right)\delta w dxdy\right]dt=0 \tag{2.29}$$

Which eventually leads to equation of motion found with equilibrium approach.

$$D\nabla^4 w+\rho h\frac{\partial^2 w}{\partial t^2}=q \tag{2.30}$$

Unsurprisingly, both of the EOM derived with different approaches are the same. In spite of the fact that equilibrium approach is effortless and doesn't require integration of complicated functions, variational approach is necessary for the rest of the analysis because Rayleigh-Ritz method requires strain and kinetic energy integrals.

2.4 Solution of the EOM

EOM of the transverse vibration of the plate is a fourth order nonhomogeneous partial differential (PDE) equation. In order to solve equations for free vibrations q is neglected.

$$D\left(\frac{\partial^4 w}{\partial x^4}+2\frac{\partial^2 w}{\partial x\partial y}+\frac{\partial^4 w}{\partial y^4}\right)+\rho h\frac{\partial^2 w}{\partial t^2}=0 \tag{2.31}$$

The plate has three different simple boundary types with requirement to satisfy different boundary conditions, divided into natural and geometric boundary conditions. Geometric BCs involve boundary conditions regarding displacement and slope. On the other hand, natural BCs necessitate satisfaction of force and moment equations.

The first type of boundary is called *clamped (fixed) edge* requires that displacement and slope at the edge must be zero.

$$\begin{aligned} w\big|_{x=a} &= 0 \\ \left.\frac{\partial w}{\partial x}\right|_{x=a} &= 0 \end{aligned} \tag{2.32}$$

Where $x=a$ denotes the edge since y is unconstrained. The second type boundary is called *simply supported edge*. It is required to have zero displacement and bending moments at the edge for simply supported case.

$$\begin{aligned} w\big|_{x=a} &= 0 \\ M_x\big|_{x=a} &= -D\left(\frac{\partial^2 w}{\partial x^2}+\nu\frac{\partial w^2}{\partial y^2}\right)\Bigg|_{x=a}=0 \end{aligned} \tag{2.33}$$

Last boundary type is called *free edge*. Free boundary necessitates zero bending moments and shear forces at the edge.

$$\begin{aligned} M_x\big|_{x=a} &= -D\left(\frac{\partial^2 w}{\partial x^2} + \nu\frac{\partial w^2}{\partial y^2}\right)\Bigg|_{x=a} = 0 \\ M_{xy}\big|_{x=a} &= 0 \\ Q_x\big|_{x=a} &= 0 \end{aligned} \tag{2.34}$$

Although M_{xy} *and* Q_x boundary conditions seem to be different and they are related and thus form only one boundary condition.

$$V_x\big|_{x=a} = \left(Q_x - \frac{\partial M_{xy}}{\partial y}\right)\Bigg|_{x=a} = D\left[\frac{\partial^3 w}{\partial x^3} + (2-\nu)\frac{\partial^3 w}{\partial x \partial^2 y}\right]_{x=a} = 0 \tag{2.35}$$

Other than these boundary conditions, edge supported by elastic torsional spring and edge supported by elastic spring boundary conditions are present but not in the scope of this article.

Solution of the EOM shown in equation (2.31) varies with the boundary conditions. Hence, transversely vibrating plates are defined according to their boundary conditions. S and C respectively denotes simply supported and clamped edge whilst F symbolizes free edge. For instance, C-F-F-F plate is read as cantilever plate since all of the edges are free except one is fixed to substrate. Although there exists 81 combination of classical boundary conditions, only 21 of them are unique. S-S-S-S plate is the simplest one and therefore solved as an example to demonstrate analytical solutions in coursebooks. Moreover, plates having two opposite sides simply supported have well-known Navier and Levy analytical solutions. These cases are S-F-S-F, S-C-S-F, S-C-S-C, S-S-S-F and S-S-S-C. Other boundary conditions are unfortunately hard to solve or impossible to find an exact solution[48]. Completely free plate, which is F-F-F-F, fall in the category of boundary conditions that doesn't have any exact solution. Solution of F-F-F-F plate is achieved through approximate

methods like Rayleigh-Ritz or Galerkin methods. Accuracy of such methods depends on assumed approximate functions.

Solving EOM given in equation (2.31) is expected to yield a result in the form of multiplication with space variables and time because EOM is a PDE with two space variables and time.

$$w(x, y, t) = \theta(x)\phi(y)e^{i\omega t} \tag{2.36}$$

Assumed approximate functions are necessary to develop a solution in Rayleigh-Ritz method. Thus, transverse displacement of the plate is written in the form of series.

$$w(x, y) = \sum_{j} c_j f_j(x, y) \tag{2.37}$$

Where j is the number of assumed functions and determined by user without any constrain. As the number of assumed approximate functions increase, so the accuracy of the end result. However, computational burden grows with rising number of assumed functions. Hence, an optimal number of assumed functions is chosen so that neither computation requires a lot of time nor accuracy of the calculation is low.

As previously stated, EOM consists of two space variables and time. Therefore, another form of equation (2.37) is written below.

$$w(x, y) = \sum_{m} \sum_{n} C_{mn} \theta_m(x) \phi_n(y) \tag{2.38}$$

Note that $j = m \times n$ is the number of assumed functions.

A system without any kind of energy dissipation constantly transforms kinetic energy to potential energy while vibrating. If maximum potential and kinetic energies are equated to each other, there exist a constant in this equation. This constant is calculated by minimizing the Rayleigh quotient as constant is expected to be minimum around fundamental natural frequency.

Rayleigh quotient's definition is given below.

$$R = \frac{U_{\max}}{T_{\max}} \tag{2.39}$$

According to Lord Rayleigh, assuming a function and then calculating energies impose additional constraint on system and results in upper bound frequency[49]. Walter Ritz has demonstrated that superimposing several assumed functions generates multiple eigenvalues and eigenvectors with an example solution of natural frequencies and mode shapes of a F-F-F-F plate in his famous papers[50], [51].

Before applying Rayleigh-Ritz method, kinetic and strain energy integrals are put in the nondimensional form. Nondimensional counterparts of the variables are shown with capital letters.

$$\begin{aligned} X &= \frac{x}{a} \\ Y &= \frac{y}{b} \end{aligned} \tag{2.40}$$

Transverse displacement of the plate in nondimensional form.

$$\begin{aligned} w(x,y) &= W(aX, bY) \\ W(X,Y) &= \sum_j c_j F_j(X,Y) \end{aligned} \tag{2.41}$$

Strain energy of the plate without external force is nondimensionalized.

$$\begin{aligned} U_{\max} = \frac{Dab}{2a^4} \iint_R \Bigg[& \left(\frac{\partial^2 W}{\partial x^2} + \alpha^2 \frac{\partial^2 W}{\partial y^2} \right)^2 \\ & -2(1-\nu)\alpha^2 \left(\frac{\partial^2 W}{\partial x^2}\frac{\partial^2 W}{\partial y^2} - \left(\frac{\partial^2 W}{\partial x \partial y} \right)^2 \right) \Bigg] dX dY \end{aligned} \tag{2.42}$$

Where $\alpha = a/b$ is the aspect ratio of the plate. For square plate, it is 1.

Similar to strain energy integral, nondimensional kinetic energy is expressed.

$$T_{\max} = \frac{\rho hab\omega^2}{2} \iint_R W^2 dXdY \tag{2.43}$$

In order to apply Rayleigh-Ritz method, maximum kinetic and strain energies are equated to each other. Later, that equation is changed to division with simple algebra.

$$\begin{aligned} V_{\max} &= T_{\max} \\ V_{\max} &= \omega^2 T^*_{\max} \\ R = \omega^2 &= \frac{V_{\max}}{T^*_{\max}} \end{aligned} \tag{2.44}$$

Where $T^*_{\max}$ is called reference kinetic energy in some course books and defined as follows[52].

$$T^*_{\max} = \frac{\rho hab}{2} \iint_R W^2 dXdY \tag{2.45}$$

Then, Rayleigh quotient is written and minimized with respect to each coefficient of assumed functions.

$$\frac{\partial R}{\partial c_i} = 0 \tag{2.46}$$

It is already defined as the ratio of strain energy to kinetic energy.

$$\frac{\partial R}{\partial c_i} = \frac{\partial\left(\frac{V_{\max}}{T^*_{\max}}\right)}{\partial c_i} = \frac{\frac{\partial V_{\max}}{\partial c_i} T^*_{\max} - V_{\max} \frac{\partial T^*_{\max}}{\partial c_i}}{{T^*_{\max}}^2} = 0 \tag{2.47}$$

Dividing each side with T^2 expression.

$$\begin{aligned} &\frac{1}{T^*_{\max}} \left(\frac{\partial V_{\max}}{\partial c_i} - \frac{V_{\max}}{T^*_{\max}} \frac{\partial T^*_{\max}}{\partial c_i} \right) = 0 \\ &\frac{\partial V_{\max}}{\partial c_i} - \lambda \frac{\partial T^*_{\max}}{\partial c_i} = 0 \end{aligned} \tag{2.48}$$

Resultant is obviously an Eigenvalue problem (EVP). Solution of this EVP generates eigenvalues, which are square of natural frequencies, and eigenvectors, which describe modes in the space.

$$\left(\left[K\right]-\lambda\left[M\right]\right)\mathbf{c}=\mathbf{0} \tag{2.49}$$

Where stiffness and mass matrices are calculated by virtue of strain and kinetic energy integrals.

$$\begin{aligned}\left[K\right]&=\frac{\partial V_{\max}}{\partial \mathbf{c}}\\ \left[M\right]&=\frac{\partial T_{\max}}{\partial \mathbf{c}}\end{aligned} \tag{2.50}$$

Substituting Equation (2.41) into above equation and deriving stiffness and mass matrices. Derivation of the stiffness and matrix elements is shown in the literature[53].

$$M_{ij}=\frac{\rho hab}{2}\int_0^1\int_0^1 F_iF_j\,dXdY \tag{2.51}$$

$$\begin{aligned}K_{ij}=\frac{Dab}{2a^4}\int_0^1\int_0^1\Bigg\{&\frac{\partial^2F_i}{\partial X^2}\frac{\partial^2F_j}{\partial X^2}+\frac{\partial^2F_i}{\partial Y^2}\frac{\partial^2F_j}{\partial Y^2}\\ &+\nu\alpha^2\left(\frac{\partial^2F_i}{\partial X^2}\frac{\partial^2F_j}{\partial Y^2}+\frac{\partial^2F_j}{\partial X^2}\frac{\partial^2F_i}{\partial Y^2}\right)\\ &+2\left(1-\nu\right)\alpha^2\frac{\partial^2F_i}{\partial X\,\partial Y}\frac{\partial^2F_j}{\partial X\,\partial Y}\Bigg\}dXdY\end{aligned} \tag{2.52}$$

Up to now, mass and stiffness matrix derivations are shown but trial functions are yet to be discussed.

Although there are several sets of orthogonal and linearly independent trial functions suitable for RRM method, F-F beam eigenfunctions are widely utilized to solve for natural frequencies and mode shapes[54]. Despite the fact that F-F beam characteristic functions only satisfy geometric BCs but not natural ones, they are

proven to provide adequate approximations. As a result, trial functions in this scenario are called admissible functions rather than comparison or eigenfunctions.

These F-F beam eigenfunctions are widely published in the literature. F-F beam eigenfunctions with corner being the origin is shown.

$$\theta(x) = 1 \; for \; m = 0$$

$$\theta(x) = 1 - \frac{2x}{a} \; for \; m = 1$$

$$\theta(x) = \cos\left[\gamma_1\left(\frac{x}{a} - \frac{1}{2}\right)\right] - \frac{\sin\left(\frac{\gamma_1}{2}\right)}{\sinh\left(\frac{\gamma_1}{2}\right)}\cosh\left[\gamma_1\left(\frac{x}{a} - \frac{1}{2}\right)\right] \; for \; m = 2,4,6... \tag{2.53}$$

$$\theta(x) = \sin\left[\gamma_2\left(\frac{x}{a} - \frac{1}{2}\right)\right] + \frac{\sin\left(\frac{\gamma_2}{2}\right)}{\sinh\left(\frac{\gamma_2}{2}\right)}\cosh\left[\gamma_2\left(\frac{x}{a} - \frac{1}{2}\right)\right] \; for \; m = 3,5,7...$$

For $\phi(y)$, replace x with y and a with b in above equations. γ_1 *and* γ_2 are the roots of the following equations.

$$\begin{aligned} \tan\left(\frac{\gamma_1}{2}\right) + \tanh\left(\frac{\gamma_1}{2}\right) &= 0 \\ \tan\left(\frac{\gamma_2}{2}\right) - \tanh\left(\frac{\gamma_2}{2}\right) &= 0 \end{aligned} \tag{2.54}$$

Roots of the above equations is already tabulated in the literature[55].

Table 2.3 Roots of the F-F beam eigenfunctions

m	γ_1	*m*	γ_1
2	4.730	3	7.853
4	10.996	5	14.137
6	17.279	7	20.420
Approximate	$(2m-1)\pi/2$	Approximate	$(2m-1)\pi/2$

As all necessary information is known, trial function is written in terms of assumed functions.

$$W = \sum_j c_j F_j(x,y) = C_{00}\theta_0\phi_0 + C_{01}\theta_0\phi_1 + C_{10}\theta_1\phi_0 + C_{11}\theta_1\phi_1 \\ +C_{02}\theta_0\phi_2 + C_{20}\theta_2\phi_0 + C_{12}\theta_1\phi_2 + C_{21}\theta_2\phi_1 + C_{22}\theta_2\phi_2 + ... \tag{2.55}$$

Above equation leads to following equations.

$$\begin{aligned} c_1F_1 &= C_{00}\theta_0\phi_0 \\ c_2F_2 &= C_{01}\theta_0\phi_1 \\ c_3F_3 &= C_{10}\theta_1\phi_0 \\ &\vdots \end{aligned} \tag{2.56}$$

In order to apply RRM, functions given above is substituted into equation (2.51) and equation (2.52). Number of trial functions are decided regarding convergence of the natural frequencies. There several possible number of trial functions such as j=4, 9, 16, 25, 36, 49, 64, 81. These numbers are determined by which last coefficient is included in the trial function. For instance, last term A_{11} corresponds to 4 terms while number of trial functions is equal to 64 when last term is A_{77}. After computing natural frequencies of the 1st and 2nd modes along with relative error, it is seen that relative error becomes smaller than 0.3% after j=16 and 0.1% after j=64. Henceforth, all of the reported results considering natural frequencies and mode shapes are found with 81 trial functions.

Then, eigenvalue problem is solved numerically using MATLAB. Output of the eigenvalue solution is tabulated on the next page.

Table 2.4 RRM results for 1st and 2nd mode

Type of Travel	*1st Mode*	*2nd Mode*
Dimensionless frequency	13.812	20.085
Coefficients	$C_{11}=1$ $C_{13}=-0.0293$ $C_{31}=-0.0293$ $C_{33}=0.0029$	$C_{02}=1$ $C_{20}=-1$ $C_{04}=-0.0155$ $C_{40}=0.0155$

Even though other coefficients exist they are either zero or negligible compared to these coefficients. At the end, 1st and 2nd mode is written in terms of F-F beam eigenfunctions.

$$\begin{aligned} W_1 &= \theta_1(x)\phi_1(y) - 0.0293\theta_1(x)\phi_3(y) \\ &\quad - 0.0293\theta_3(x)\phi_1(y) + 0.0029\theta_3(x)\phi_3(y) \\ W_2 &= \theta_0(x)\phi_2(y) - \theta_2(x)\phi_0(y) \\ &\quad - 0.0155\theta_0(x)\phi_4(y) + 0.0155\theta_0(x)\phi_4(y) \end{aligned} \tag{2.57}$$

Plot of the above functions well matches with the designated nodal lines and published figures. Plots are shown below.

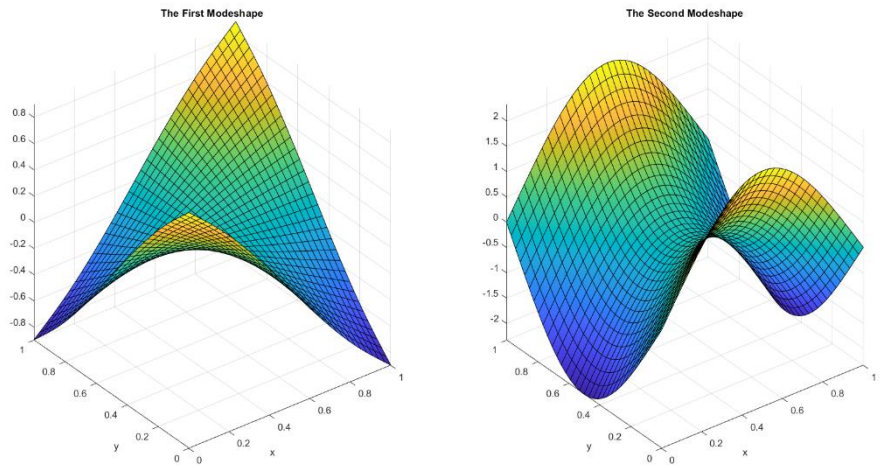

Figure 2.10. 1st (left) and 2nd (right) mode shapes

Note that these mode shapes are normalized with respect to coefficient of the first term. These results agree well with the literature[56]. A little discrepancy between results is caused by the fact that different Poisson's ratios, 0.225 and 0.343, are chosen in the article for the calculation.

Maximum deflection points of the 1st mode are corners, i.e., (0,0), (1,1), (0,1) and (1,0) while those of the 2nd mode are midpoint, i.e., (0.5,0), (0,0.5), (1,0.5) and (0.5,1). These maximum deflection points are important since they are utilized to normalize stiffness and masses.

2.4.1 Effect of cutouts

Kinetic and strain energies of the plate is computable with the known mode shape functions given as equations (2.57). Inserting mode shape functions into equations (2.42) and (2.45) results in the following tabulated kinetic and strain energies.

Table 2.5 Properties of the plate without cutouts

	1st Mode	*2nd Mode*
Strain Energy	$21.252\frac{D}{2a^2}$	$410.66\frac{D}{2a^2}$
Kinetic energy	$0.1114\frac{\rho h a^2}{2}$	$1.0179\frac{\rho h a^2}{2}$
Natural frequency	$\frac{13.8118}{a^2}\sqrt{\frac{Eh^2}{12\rho\left(1-\nu^2\right)}}$	$\frac{20.0854}{a^2}\sqrt{\frac{Eh^2}{12\rho\left(1-\nu^2\right)}}$

Effects of cutouts are taken into consideration by simply subtracting their strain and kinetics energies from the total energy of the plate. This method is previously applied and proven to be accurate for cutouts as long as they don't make up huge portion of the plate[57]. In this study, subtracting cutout energies from the plate is chosen due

to the fact that side length of the cutout is 1/36 of the plate, enormously smaller than plate dimensions. Area compromised by cutouts is smaller than 99%.

Strain and kinetic energies of the cutouts are computed by just simply changing integral limits. Below integral limits are shown for the first cutout on nodal line close to origin.

$$U_{cutout} = \frac{Dab}{2a^4}\int_{l}^{l+t}\int_{l}^{l+t}\left[\left(\frac{\partial^2 W}{\partial x^2}+\alpha^2\frac{\partial^2 W}{\partial y^2}\right)^2 -2(1-\nu)\alpha^2\left(\frac{\partial^2 W}{\partial x^2}\frac{\partial^2 W}{\partial y^2}-\left(\frac{\partial^2 W}{\partial x\partial y}\right)^2\right)\right]dXdY \tag{2.58}$$

$$U_{cutout} = \frac{\rho hab}{2}\int_{l}^{l+t}\int_{l}^{l+t} W^2 dXdY \tag{2.59}$$

Similarly integral limits are shown for the first cutout on center line close to origin.

$$U_{cutout} = \frac{Dab}{2a^4}\int_{1/2-t}^{1/2+t}\int_{l}^{l+t}\left[\left(\frac{\partial^2 W}{\partial x^2}+\alpha^2\frac{\partial^2 W}{\partial y^2}\right)^2 -2(1-\nu)\alpha^2\left(\frac{\partial^2 W}{\partial x^2}\frac{\partial^2 W}{\partial y^2}-\left(\frac{\partial^2 W}{\partial x\partial y}\right)^2\right)\right]dXdY \tag{2.60}$$

$$U_{cutout} = \frac{\rho hab}{2}\int_{1/2-t}^{1/2+t}\int_{l}^{l+t} W^2 dXdY \tag{2.61}$$

In order to express cutouts with respect to unit square plate, cutouts position and size is also expressed in terms of nondimensional parameters.

$$L = \frac{l}{a}\ \&\ T = \frac{t}{a} \tag{2.62}$$

Later these found strain and kinetic energies of cutouts are subtracted from the plate energy and square root of the energy ratio is computed.

Below a formulation for the 1st and 2nd mode natural frequency with cutouts are illustrated, respectively.

$$f_1 = \frac{1}{2\pi}\sqrt{\frac{\frac{D}{2a^2}\left(21.252 - 4U_{cutouts1}\right)}{\frac{\rho h a^2}{2}\left(0.1114 - 4T_{cutouts1}\right)}} \tag{2.63}$$

$$f_2 = \frac{1}{2\pi}\sqrt{\frac{\frac{D}{2a^2}\left(410.66 - 4U_{cutouts2}\right)}{\frac{\rho h a^2}{2}\left(1.0179 - 4T_{cutouts2}\right)}} \tag{2.64}$$

Note that cutouts are symmetric with respect to either diagonals or center lines. 1st mode transverse displacement is symmetric with respect to diagonal lines while antisymmetric with respect to centerlines. To contrary, 2nd mode is antisymmetric with respect to diagonals whilst symmetric with respect to centerlines. Hence, calculating only 1st and 2nd cutouts energies is sufficient.

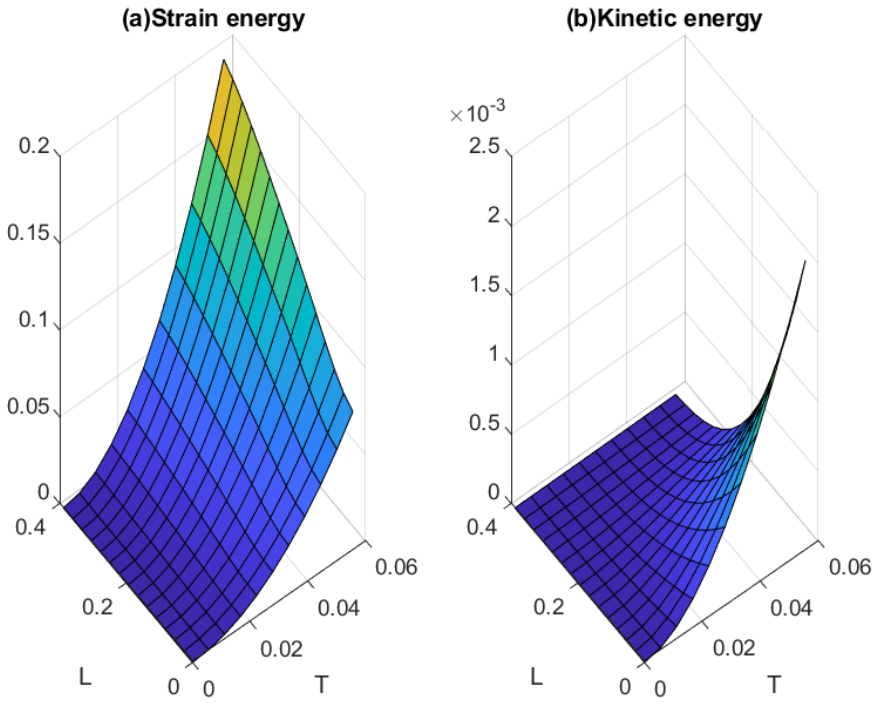

Figure 2.11. Nondimensional strain and kinetic energies of cutouts for 1st mode

A polynomial surface curve fit is computed in MATLAB and results are given below.

$$U_{cutouts1}(L,T) = 0.0094 - 1.177T - 0.04687L + 45.94T^2 + 5.634LT \quad (2.65)$$

$$T_{cutouts1}(L,T) = -5.757\times10^{-5} + 0.0115T + 0.0004024L + 0.4612T^2 \\ -0.1416LT + 0.001881L^2 - 1.478T^2L + 0.3373TL^2 - 0.007887L^3 \quad (2.66)$$

As it seen from Figure 2.11, strain energy of cutouts exhibits highly linear behavior over changing position whilst size of cutouts remains steady. On the other hand, it is obvious kinetic energy has a parabolic relation with the position of cutout in case of constant cutout size. Hence, strain and kinetic energy curve fits are computed and given below for T=1/36(t=10μm).

$$U_{cutouts1} = 0.01821 + 0.07846L \quad (2.67)$$

$$T_{cutouts1} = 0.00488L^2 - 0.003293L + 0.0005581 \quad (2.68)$$

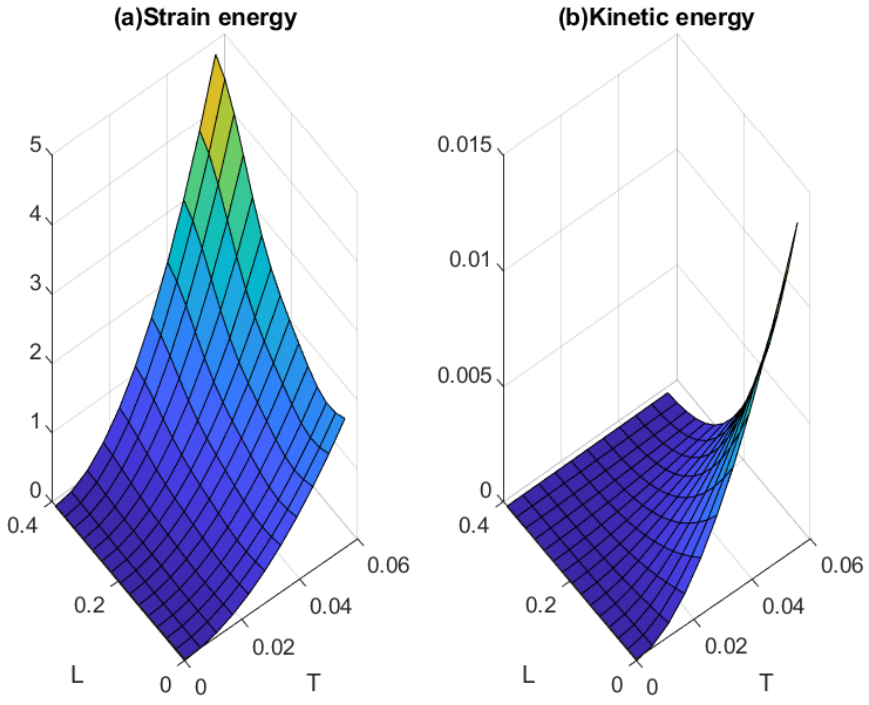

Figure 2.12. Nondimensional strain and kinetic energies of cutouts for 2nd mode

A polynomial surface curve fit is computed in MATLAB and results are given below.

$$U_{cutout2} = -0.04719 + 10.08T + 0.2173L + 397.9T^2 \\ -177.7LT + 3.999L^2 + 2946T^2L + 429.2TL^2 - 12.48L^3 \quad (2.69)$$

$$T_{cutouts2} = -0.0003719 + 0.07729T + 0.002182L + 3.109T^2 \\ -0.9626LT + 0.01632L^2 - 9.941T^2L 2.297TL - 0.05957L^3 \quad (2.70)$$

As it is seen from Figure 2.12, strain energy curve is rather steep unlike in the 1st mode. Therefore, both strain and kinetic energy levels are expected to have parabolic relation with the position of cutouts for the same constant cutout size.

$$U_{cutouts1} = 6.608L^2 - 0.5639L + 0.4634 \quad (2.71)$$

$$T_{cutouts1} = 0.003343L^2 - 0.2237L + 0.003757 \quad (2.72)$$

2.5 Capacitive actuation and detection

A figure illustrating capacitive actuation and sense circuit is shown below.

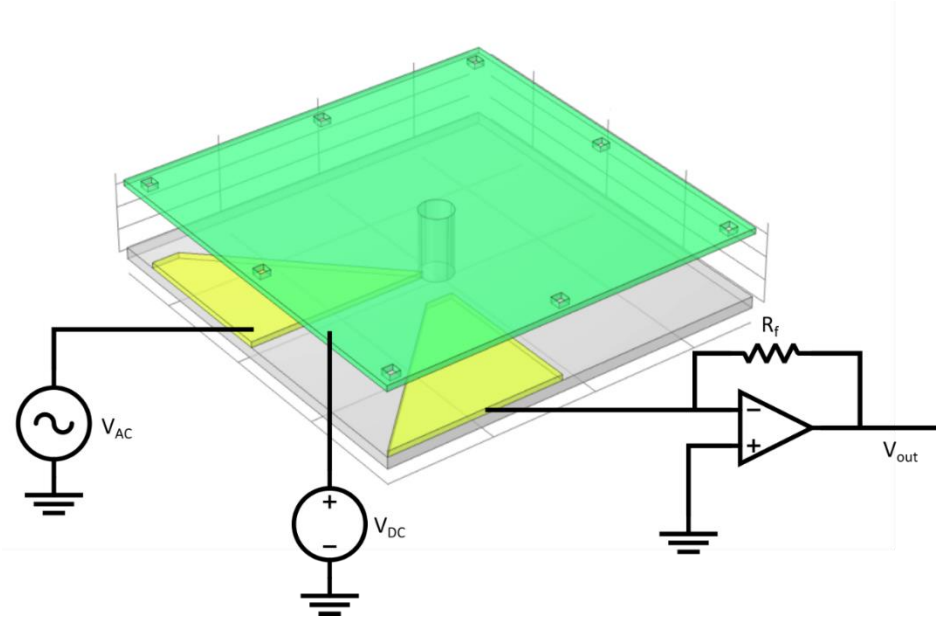

Figure 2.13. Drive and sense circuit of the plate resonator

Microresonator plate is driven with an AC voltage source whilst DC voltage is applied to plate as proof mass voltage. Output of the plate is directly fed to transimpedance amplifier to convert current to voltage. In this study, capacitive actuation is modelled as a parallel plate capacitive actuator since plate post make up a small portion of the plate structure. Resonator is considered to be in perfect vacuum to maximize Q-factor and minimize loss. Capacitance between two plates under perfect vacuum is formulated as follows:

$$C = \iint_{R_{electrode}} \frac{\varepsilon_0 dA}{g - w(x,y)} \tag{2.73}$$

Where ε_0 is the dielectric permittivity of the perfect vacuum. Plate resonator is excited with an alternating current, which is defined as shown below.

$$V_{AC} = v_{AC} \sin(\omega t) \tag{2.74}$$

Electrostatic energy stored in the capacitor has a simple formula.

$$E = \frac{1}{2} C V^2 \tag{2.75}$$

Substituting voltage difference caused by proof mass voltage and excitation force.

$$E = \frac{\varepsilon_0}{2} \left(V_{AC} - V_{DC}\right)^2 \iint_{R_{electrode}} \frac{dA}{g - w(x,y)} \tag{2.76}$$

Capacitance leads to electrostatic force which is simply gradient of the electrostatic energy stored in the capacitor.

$$F = \frac{\partial E}{\partial z} = -\frac{\varepsilon_0}{2} \left(V_{AC} - V_{DC}\right)^2 \iint_{R_{electrode}} \frac{dA}{\left(g - w(x,y)\right)^2} \tag{2.77}$$

Where $z = (g - w)$ is the definition of the distance in the z axis.

Inserting excitation voltage formula into force equation.

$$F = -\frac{\varepsilon_0}{2}\left(v_{AC}^2 \sin^2(\omega t) - 2V_{DC}v_{AC}\sin(\omega t) + V_{DC}^2\right) \iint_{R_{electrode}} \frac{dA}{\left(g - w(x,y)\right)^2} \quad (2.78)$$

Above force equation is rearranged by virtue of trigonometry.

$$\begin{aligned} F = &-\frac{\varepsilon_0}{2} \iint_{R_{electrode}} \frac{dA}{\left(g - w(x,y)\right)^2} \\ &\times\left(\frac{v_{AC}^2}{2} + V_{DC}^2 - 2V_{DC}v_{AC}\sin(\omega t) - \frac{v_{AC}^2}{2}\cos(2\omega t)\right) \end{aligned} \quad (2.79)$$

Force excitation is divided into three groups:

$$\begin{aligned} F = &\underbrace{-\frac{\varepsilon_0}{2} \iint_{R_{electrode}} \frac{dA}{\left(g - w(x,y)\right)^2}\left(\frac{v_{AC}^2}{2} + V_{DC}^2\right)}_{DC\,Term} \\ &\underbrace{+\varepsilon_0 \iint_{R_{electrode}} \frac{dA}{\left(g - w(x,y)\right)^2} V_{DC}v_{AC}\sin(\omega t)}_{Sinusoidal\,Term} \\ &\underbrace{+\frac{\varepsilon_0}{4} \iint_{R_{electrode}} \frac{dA}{\left(g - w(x,y)\right)^2} {v_{AC}}^2\cos(2\omega t)}_{Double\,Frequency\,Term} \end{aligned} \quad (2.80)$$

While DC Term is suitable to be considered as constant since transvers displacement of the plate is negligible compared to capacitive gap, double frequency term completely depends on magnitude of the excitation voltage. Moreover, driving voltage is enormously smaller than proof mass voltage, making double frequency term omissible. Considering transverse displacement of the plate as insignificant, excitation force can be expressed with only one term.

$$F = \frac{A_{electrode}\varepsilon_0 V_{DC}^2}{2g^2} \quad (2.81)$$

Capacitive detection is achieved through measurement of the current induced by vibrating resonator. There is a classical formula relating charge to capacitance and voltage.

$$q = CV \tag{2.82}$$

Rate of the change of the charge equals to current. Hence, taking derivative of the charge with respect to time results in current.

$$i = \frac{\partial q}{\partial t} = \frac{\partial C}{\partial t} V + \frac{\partial V}{\partial t} C \tag{2.83}$$

Capacitance changes with variation of the capacitive gap. Thus, capacitance is also regarded as a function of position.

$$\begin{aligned} i &= \frac{\partial q}{\partial t} = \frac{\partial C}{\partial z}\frac{\partial z}{\partial t} V + \frac{\partial V}{\partial t} C \\ i &= \frac{\partial C}{\partial z} \dot{z} V + \dot{V} C \end{aligned} \tag{2.84}$$

Sensing electrode is not applied excitation voltage, there exists only induced AC which is negligible small in magnitude. Therefore, second term of the current expression is taken to be zero.

$$i = \frac{\partial C}{\partial z} \dot{z} V_{DC} = -\frac{\varepsilon_0 A}{\left(g - w(x,y)\right)^2} V_{DC} \dot{z}^2 \tag{2.85}$$

Output of the transimpedance amplifier is expressed as following.

$$V_{out} = -R_f i = \frac{\varepsilon_0 A R_f}{\left(g - w(x,y)\right)^2} V_{Dc} \dot{z} = -\frac{\varepsilon_0 A R_f V_{DC}}{\left(g - w(x,y)\right)^2} \dot{w}^2 \tag{2.86}$$

As it is seen from the result of the transimpedance amplifier, output voltage is dependent on the first-time derivative of the transverse displacement of the plate resonator. There has to 90˚ phase between z and i. If excitation is sinusoidal, output current amplitude is a function of the vibration frequency. Increasing frequency leads to rise in current.

Proof mass voltage applied to plate causes a negative force on the plate since it is obvious from equation (2.77) that force acts in the opposite direction of the displacement. As a result, electrostatic spring softening is observed in the plate resonator. It is called softening because resonance frequency decreases as proof mass voltage grows. As previously stated, excitation voltage is negligible compared to proof mass voltage. Thus, both of the electrodes could be considered as ground. Electrostatic softening effect is highly dependent on the displacement so it is not logical to omit transverse displacement in equation (2.73).

$$C = \iint_{R_{electrode}} \frac{\varepsilon_0}{g - w(x,y)} dA \tag{2.87}$$

Inserting above equation into electrostatic energy equation.

$$E = \frac{1}{2} \iint_{R_{electrode}} \frac{\varepsilon_0 {V_{DC}}^2}{(g - w(x,y))} dA \tag{2.88}$$

Equating energy stored in capacitor to a virtual spring is one of the ways to find electrostatic spring stiffness.

$$\frac{1}{2} \iint_{R_{electrode}} \frac{\varepsilon_0 {V_{DC}}^2}{(g - w(x,y))} dA = \frac{1}{2} k_z W_0^2 \tag{2.89}$$

Where W_0 is the maximum displacement on the plate.

$$k_z = \frac{\iint_{R_{electrode}} \frac{\varepsilon_0 {V_{DC}}^2}{(g - w(x,y))} dA}{W_0^2} \tag{2.90}$$

Expanding division by Taylor series and neglecting both high order terms and odd powered terms since electrodes are placed under antisymmetric areas of the plate.

$$k_z = \frac{\varepsilon_0 a^2 V_{DC}^2}{g^3} \iint_{R_{electrode}} W^2 dXdY \tag{2.91}$$

Derivation of the equation is already published in the literature[58]. Above integral is numerically calculated with the help of MATLAB. Results are given below.

$$k_{z1} = 0.0278 \frac{\varepsilon_0 a^2 V_{DC}^2}{g^3} \tag{2.92}$$

$$k_{z2} = 0.1359 \frac{\varepsilon_0 a^2 V_{DC}^2}{g^3} \tag{2.93}$$

Taking electrostatic spring softening into consideration resonance frequency equations is written.

$$f_1 = \frac{1}{2\pi} \sqrt{\frac{\frac{Eh^3}{24a^2\left(1-\nu^2\right)}\left(21.252 - 4U_{cutouts1}\right) - 0.0278\frac{\varepsilon_0 a^2 V_{DC}^2}{g^3}}{\frac{\rho h a^2}{2}\left(0.1114 - 4T_{cutouts1}\right)}} \tag{2.94}$$

$$f_2 = \frac{1}{2\pi} \sqrt{\frac{\frac{Eh^3}{24a^2\left(1-\nu^2\right)}\left(410.66 - 4U_{cutouts2}\right) - 0.1359\frac{\varepsilon_0 a^2 V_{DC}^2}{g^3}}{\frac{\rho h a^2}{2}\left(1.0179 - 4T_{cutouts2}\right)}} \tag{2.95}$$

In order to compare results with the plates already produced, only cutout curve fits with T=1/36 is considered.

2.6 Effect of temperature

Effect of temperature can be modelled by considering expansion of the structure dimensions, density change and change in modulus of elasticity of Silicon as it is clear from equations (2.94) and (2.95) that resonance frequency is dependent on these parameters.

Changes caused by temperature change is written as below.

$$\begin{aligned} E &= E_0(1+\alpha_E \Delta T) \\ h &= h_0(1+\alpha_{Si}\Delta T) \\ g &= g_0(1+\alpha_{SiO_2}\Delta T) \\ a &= a_0(1+\alpha_{Si}\Delta T) \\ V &= a_0^2(1+\alpha_{Si}\Delta T)^2 h_0(1+\alpha_{Si}\Delta T) = V_0(1+\alpha_{Si}\Delta T)^3 \end{aligned} \tag{2.96}$$

Where V is the volume of the plate while V_0 is the volume at room temperature. Change in density can be found from conservation of mass.

$$m = \rho V = \rho_0 V_0 \tag{2.97}$$

With a little bit algebra, change in the density can be written as follows:

$$\rho = \frac{\rho_0}{\left(1+\alpha_{Si}\Delta T\right)^3} \tag{2.98}$$

Inserting all of the above equations into already calculated natural frequency equations in order to model effect of temperature.

$$f_1 = \frac{1}{2\pi}\sqrt{\frac{\frac{E_0(1+\alpha_E\Delta T)h_0^{\,3}(1+\alpha_{Si}\Delta T)}{24a_0^{\,2}\left(1-\nu^2\right)}\left(21.252-4U_{cutouts1}\right)-0.0278\frac{\varepsilon_0 a_0^{\,2}(1+\alpha_{Si}\Delta T)^2 V_{DC}^2}{g_0^{\,3}(1+\alpha_{SiO_2}\Delta T)^3}}{\frac{\rho_0 h_0 a_0^{\,2}}{2}\left(0.1114-4T_{cutouts1}\right)}} \tag{2.99}$$

$$f_2 = \frac{1}{2\pi}\sqrt{\frac{\frac{E_0(1+\alpha_E\Delta T)h_0^{\,3}(1+\alpha_{Si}\Delta T)}{24a_0^{\,2}\left(1-\nu^2\right)}\left(410.66-4U_{cutouts2}\right)-0.1359\frac{\varepsilon_0 a_0^{\,2}(1+\alpha_{Si}\Delta T)^2 V_{DC}^2}{g_0^{\,3}(1+\alpha_{SiO_2}\Delta T)^3}}{\frac{\rho_0 h_0 a_0^{\,2}}{2}\left(1.0179-4T_{cutouts2}\right)}} \tag{2.100}$$

2.7 FEM verification of the analytical model

In this section, analytical model has been verified with COMSOL Multiphysics. Plate is drawn parametrically in COMSOL so that with just only changing parameter, position of the cutout is easily manipulated. Tabulated mechanical and thermal

properties of the plate given in table 2.1 is entered to program. For other properties necessary for FEM, properties from built-in library of COMSOL is utilized.

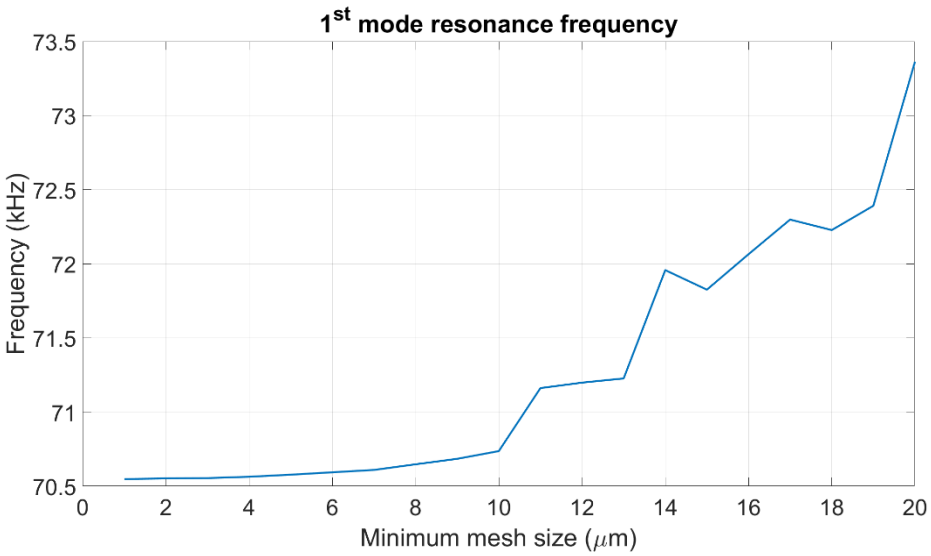

Figure 2.14. Mesh convergence study for the 1st mode

In order to choose a correct mesh size, a study for mesh convergence is conducted between 1-20 µm. Default mesh type of COMSOL is chosen, which is free tetrahedral. First and second natural frequency for different mesh sizes are computed with COMSOL. Results for the first resonance frequency is shown in Figure 2.14.

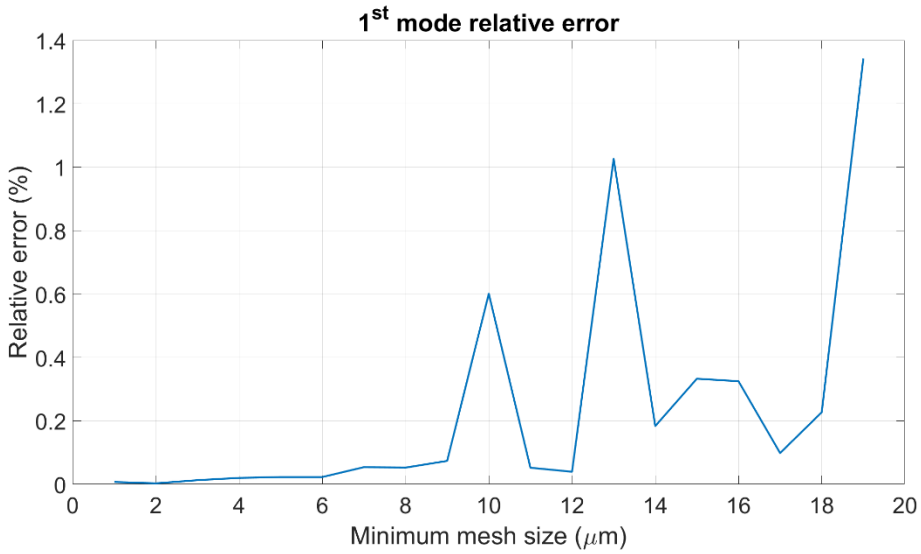

Figure 2.15. Relative error for the 1st resonance frequency

Using resonance frequencies calculated with different minimum mesh sizes, relative errors is calculated in order to interpret convergence of the results. As it is seen from Figure 2.15, relative error is less than 0.1% for mesh sizes smaller than 8 µm.

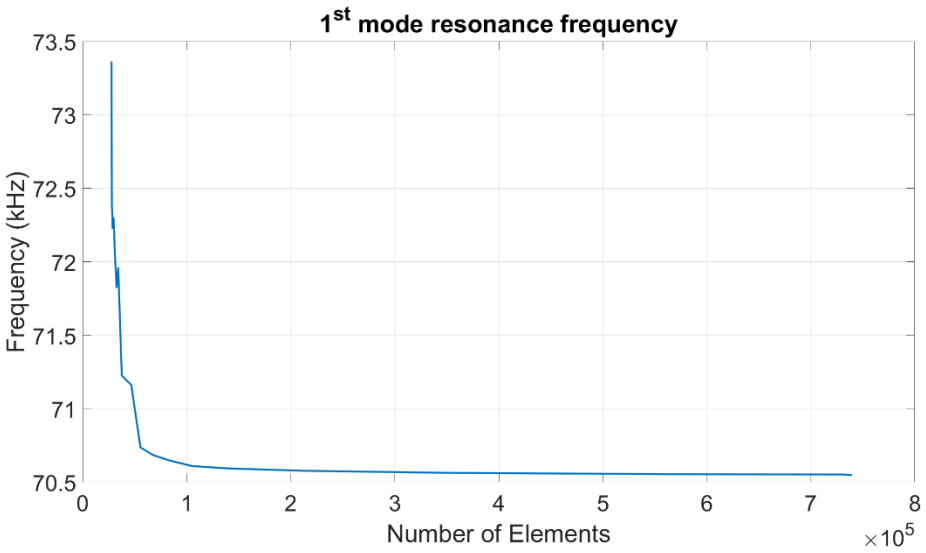

Figure 2.16. 1st resonance frequency vs the number of elements

In order to be sure about convergence of FEM, a comparison between the number of mesh elements and output resonance frequency is conducted and shown in Figure 2.16. It is obviously seen that with decreasing minimum mesh size, number of elements increase and relative error decreases. A similar trend is evident for the 2nd mode, relative error for 2nd resonance frequency is almost zero for mesh sizes smaller than 6 µm. In order to be on the safe side, mesh size of 5 µm is chosen for the rest of finite element analysis.

2.7.1 Mode shapes of the square plate

In this part of the analysis plate with plate post is simulated using COMSOL. 3D modelling of the plate is done in COMSOL with parametrical drawing. Advantage of the parametrical drawing is obviously being able to change plate design by simply changing some variables. Parameters in this scenario are gap, plate thickness, plate design, proof mass voltage, cutout position and its size. For this part of the modelling,

only Solid Mechanics physics is included. In other words, electrostatic spring softening effect along with effect of temperature is neglected.

Mechanical properties of materials used in microplate resonators are given in Table 2.2. Unknown mechanical properties are retrieved from built-in library of COMSOL. Plate, plate post, substrate and gold electrodes are selected to be linear elastic materials. While all of the surfaces are declared to be free, only face under the substrate is set to be fixed.

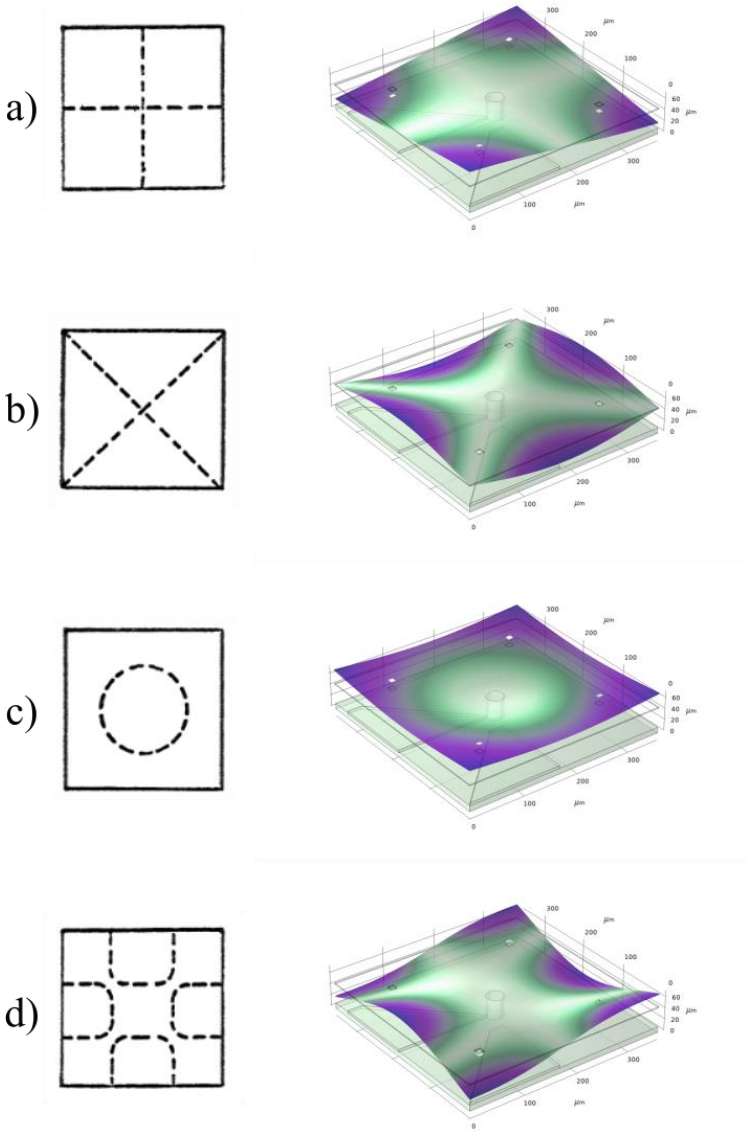

Figure 2.17. Free vibration of the microplate without electrostatic softening

Mode shape outputs of COMSOL analysis are shown in Figure 2.17. Unlike mesh convergence study in this analysis, plate post is also included in the calculations, which is expected to cause a little increase in resonance frequencies since anchor poses an additional constraint on F-F-F-F plate. In order to minimize effect of the plate post on the microplate resonance frequency, anchor is positioned at the intersection point of nodal lines of 1st and 2nd modes. 1st and 2nd mode shapes of finite element model, illustrated in Figure 2.17(a) and Figure 2.17(b), agrees with mode shapes found with analytical model. Resonance frequencies of microplates without electrostatic and thermal effects is given below.

$$\begin{aligned} f_1 &= 71.065\,kHz \\ f_2 &= 103.64\,kHz \end{aligned} \tag{2.101}$$

2.7.2 Electrostatic softening effect

Electrostatic force and its effects are studied in previous chapters. It is well known that electrostatic force causes negative stiffness and this phenomenon is called electrostatic softening effect. With decreasing gap between plate and electrodes, electrostatic force between them rises unlike mechanical springs where decline in displacement results in decrease in force. As a result, with increasing proof mass voltage, it is expected to observe decreasing resonance frequency. There is limit for proof mass voltage denoting collapse of the parallel plate capacitors called Pull-in voltage. After reaching to pull-in voltage, microplates are expected to collapse on electrodes and form short circuits. However, pull-in voltage is anticipated to be very large compared to 50 V proof mass voltage since microplates are mechanically supported from center different from parallel plate capacitors which don't have any kind of mechanical support. For instance, a similar resonator structure supported from center of the microplate is proved to be have a proof mass voltage greater than 700 V[58]. In this study, a proof mass voltage of 50 V is considered to be sufficient and far smaller than pull-in voltage.

In this part, previously drawn parametrical model of the K-plate designs are used. In order to already produced plates, plate with cutout position of 60 µm is modelled. Electrodes are declared to be ground in COMSOL since drive signal is negligible compared to proof mass voltage. For instance, -30 dBm drive signal corresponds to 20 mV while proof mass is not less than 20 volts. In order to model perfect vacuum environment, a moving mesh is defined enclosing plate, electrodes and anchor completely. Material of the vacuum is chosen as perfect vacuum from built-in library of COMSOL, which has a dielectric permittivity of 8.85×10^{-12} Fm^{-1}. As maximum displacements for both 1st and 2nd mode shapes does not exceed 5×10^{-4} µm, spatial frame can be considered as stationary.

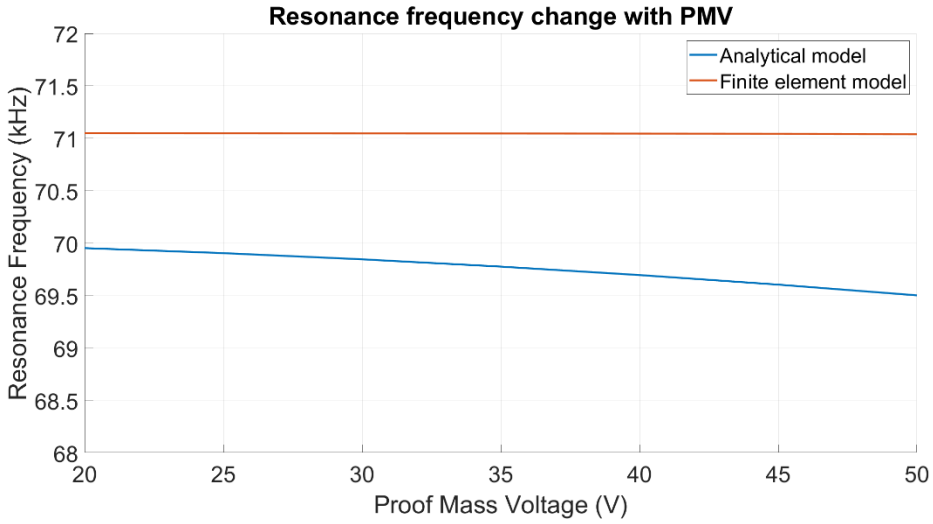

Figure 2.18. Electrostatic softening effect

Discrepancy between analytical model and COMSOL is calculated to be less than 2.5% for all of the proof mass voltages. This difference can be attributed to neglecting post plate during analytical modelling since anchor poses an extra condition rising upper bound of resonance frequency. As expected, FEM model taking plate post into consideration results in higher resonance frequencies.

Yet, error between analytical and finite element models is acceptable. Below a figure is given demonstrating relative error between finite element model and analytical model.

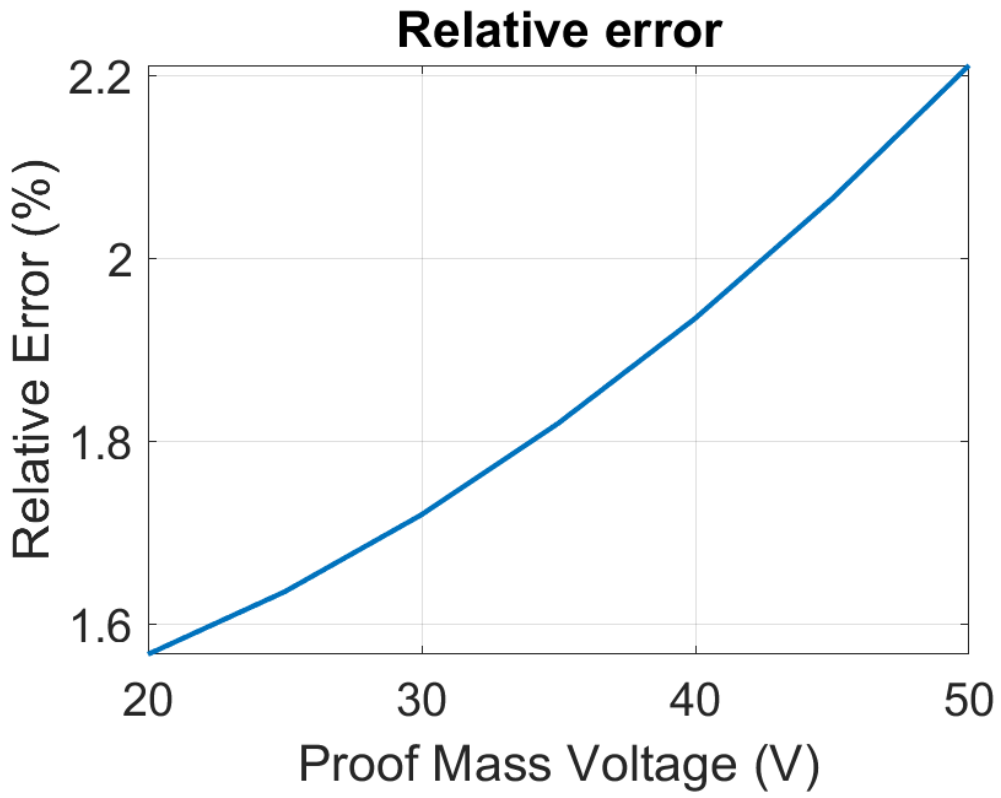

Figure 2.19. Relative error between analytical and FEM

2.7.3 Finite element modelling of cutouts

Up to this point, convergence of finite element model and discrepancy between analytical and finite element model is investigated and discussed. Consistency between analytical and finite element model is found to be sufficient. A script written in MATLAB which calculates kinetic and strain energies of cutouts at different positions for the 1st and 2nd modes. After calculation of cutouts energies, they are subtracted from total energy of the plate as previously derived with RRM. Results of these computations are saved. Finite element model is built from the same parametric model of the microplates. As position of cutouts are parametrically inserted to model

by simply changing position value of cutouts, it is possible to calculate natural frequency. A Multiphysics module is added to COMSOL which includes electrostatic and soldi mechanics physics. Plate, anchor, electrode and substrate is selected as linear elastic material. Bottom surface of substrate is chosen as fixed boundary. Otherwise, solution of FEM pops up an error stating not enough boundary conditions to solve. In the case of electrostatic, a moving mesh denoting perfect vacuum is added to model. This moving mesh has zero density so it is not selected as a linear elastic material. It is considered to effective on only electrostatic forces. After meticulous modelling of the microplates with cutouts, finite element analysis is conducted with minimum mesh size of 5 µm.

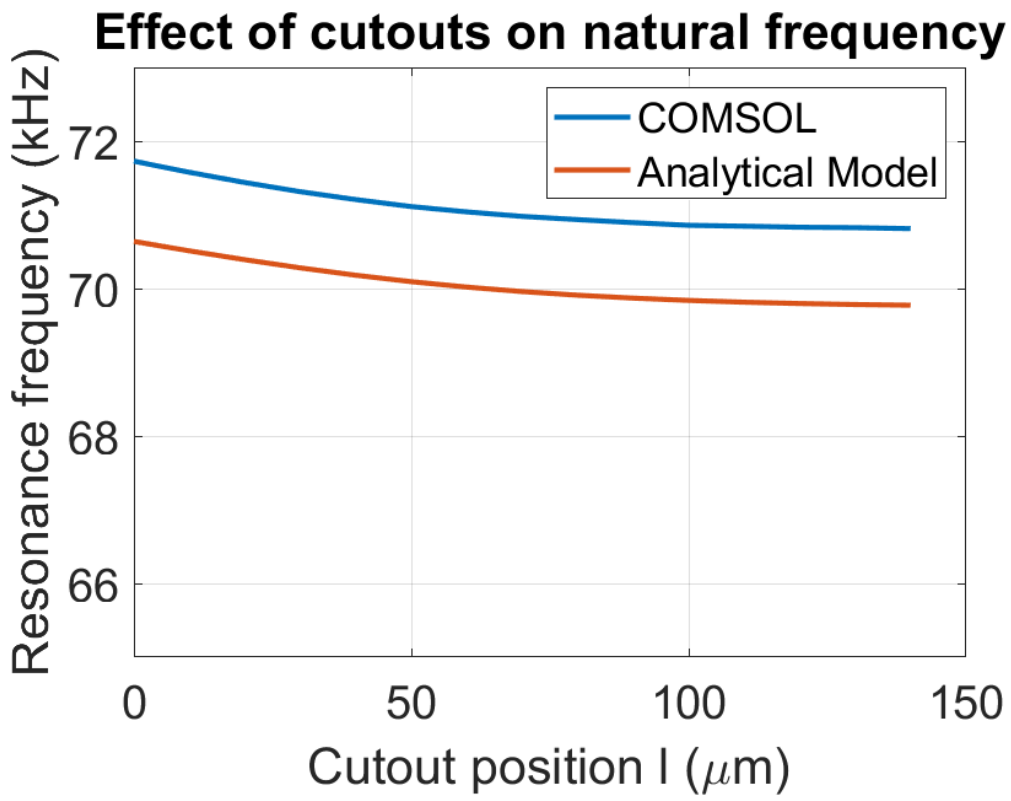

Figure 2.20. Shift of 1st resonance frequency with cutout position

As it is seen from Figure 2.20, resonance frequency declines with cutouts getting closer to center of plate. Results are in agreement with the kinetic and strain energy graphs plotted in Chapter 2.4.1. While kinetic energies of cutouts shrink, strain

energies of cutouts grow parabolically as position of cutouts gets closer to center of the microplate. Thus, decline in resonance frequency is awaited with each step towards the center of plate.

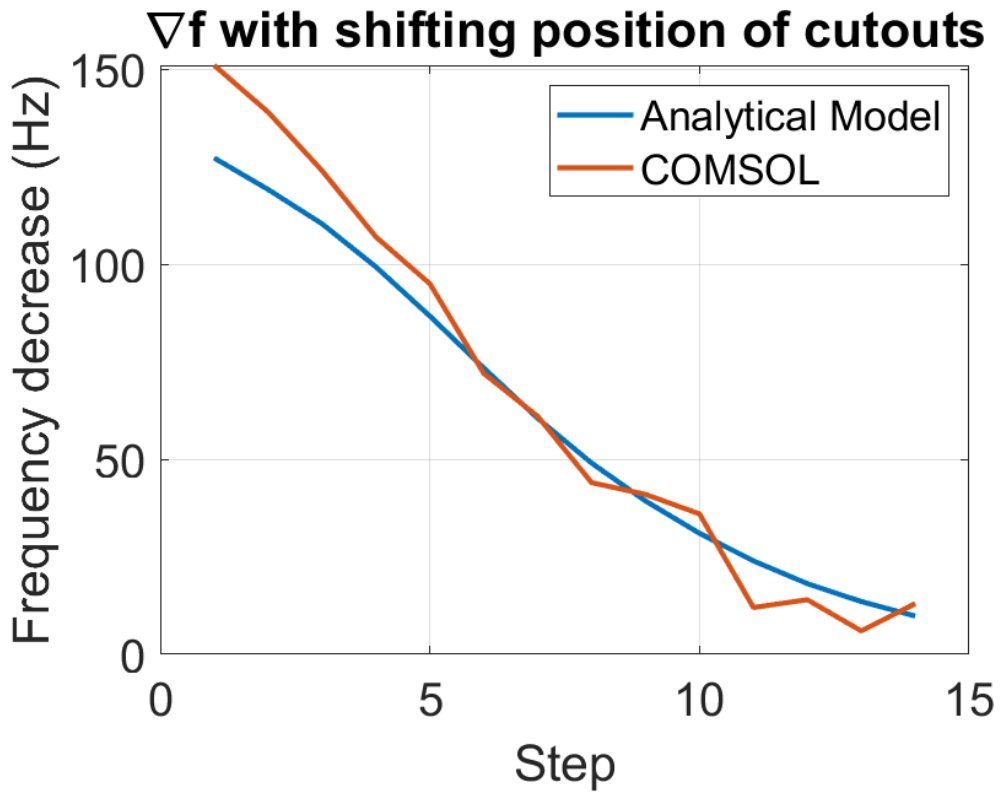

Figure 2.21. Frequency shift with each step

Above figure shows the amount of frequency decrease with each step towards center. For instance, there is a 130 Hz frequency shift between l = 0 µm and l = 10 µm. Obviously, rate of frequency shift goes down as cutouts come close to the center. It can be interpreted that cutouts close to edge of plate are easier to control resonance frequency since frequencies are farther from each other.

2.7.4 Finite element model of temperature change

Thermal effect on the microplate resonator is again modelled for cutout position of 60 µm. Except for perfect vacuum environment, i.e., moving mesh, every material is

selected for thermal domain. Then, temperature of the whole structure is defined as a parameter to allow parametric sweep analysis. With minimum mesh size of 5 µm, analysis is conducted. According to COMSOL model, a uniform temperature distribution all over the microplate is assumed since no heat source or sink is defined.

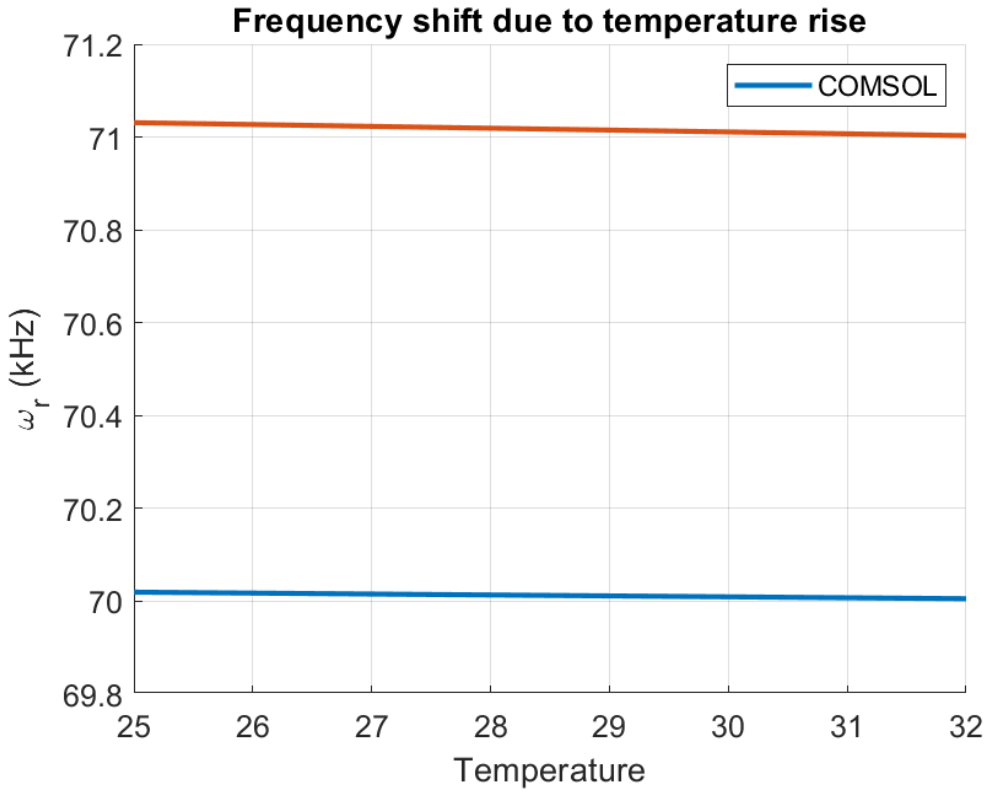

Figure 2.22. Effect of temperature on resonance frequency

It is obviously seen from the above figures, there is a linear decrease in resonance frequency for both analytical model and FEM as temperature rises. While temperature sensitivity is 4 Hz/˚C for COMSOL, 2 Hz/˚C is computed according to analytical model. Discrepancy rooting from not including post plate in analytical model seems to be persisting up to this point.

In this chapter, analytical and finite element models of microplates are compared with each other. Overall, discrepancy between them is acceptable and they show the same trend throughout to analysis.

CHAPTER 3

TEST SETUP AND EXPERIMENTS

The fabrication of microresonator plates is discussed in the first part of this chapter. How design is related to end product is explained. Later a section of design is shown along with explanation of how design is transferred from computer. Then, process flow called advance MEMS (aMEMS) is described in detail. aMEMS is a process flow in METU MEMS CENTER to produce MEMS devices from wafer. A chart illustrating each process step is also supplied along with explanations.

With an insight into microfabrication process flow, fabricated MEMS resonator plates are investigated. Results of microfabrication process flow are discussed together with possible effects of production flaws on test results. Possible reasons of microfabrication defects are highlighted and some solutions are proposed.

In the third part of the chapter, test setup is introduced. Test setup is comprised of a network analyzer, several power supplies, vacuum chamber and an oscilloscope. Read out circuit is presented. Several photographs describing test setup is also provided.

Lastly, tests and how they are conducted are explained along with results. Some results are interpreted and commented.

3.1 MEMS Manufacturing process flow

Fabrication of an array of MEMS resonator plates with adjustable frequency is first designed for the chip. While manufacturing MEMS devices, photolithography is used to pattern mask for each layer. During photolithography, a liquid called photoresist (PR) is poured on top of substrate. Later PR is soft baked in order to vaporize solvent and solidify it. After soft baking, UV radiation is applied to PR with

transparent plate with opaque patterns named mask. Later, wafer is submerged into a liquid called developer solution so that PR regions which are subjected to UV radiation dissolves away. Last step is called hard bake which completely solidifies PR for further processes. This photolithography process is sometimes called patterning. It is obvious that design in the computer converted to patterns with masks. Patterns on each mask is designed through software capable of drawing layouts. As microfabrication requires several masks to be completed successfully, multiple layouts are drawn in this software.

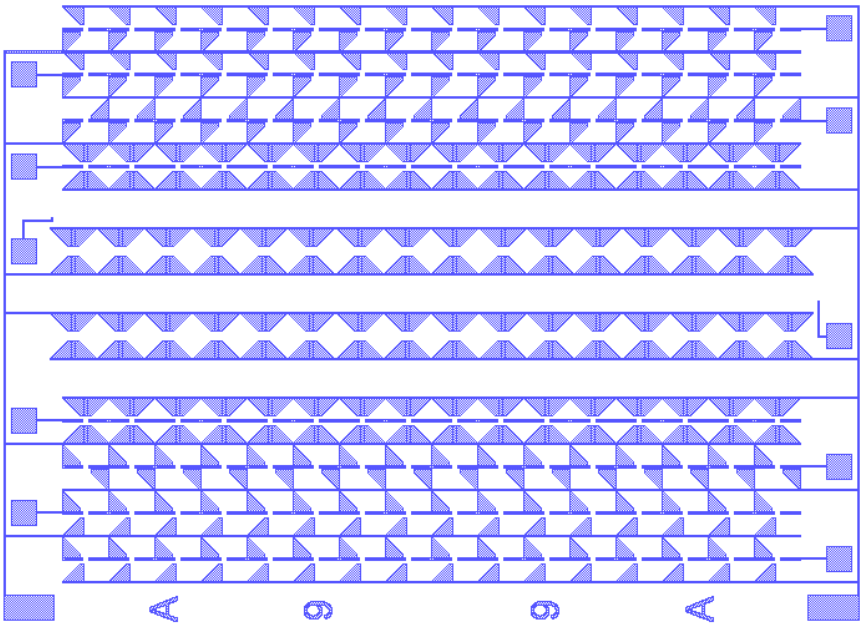

Figure 3.1. Layout of gold electrodes underneath the plates

The fabrication of MEMS plate starts with a SOI wafer and a completely glass (silicon dioxide) wafer. SOI wafer is a (111) silicon-insulator-silicon layered substrate, shown in Figure 3.2(a). The top layer is sometimes called device layer since microelectromechanical devices are produced on this layer. Thickness of the device layer is 4 µm for this SOI wafer. The first step of the microfabrication process is to pattern designed device on top layer with photolithography. After patterning, deep etching is required to have high aspect ratio cavities. Deep reactive ion etching (DRIE) is applied device layer to define side length of plates and cutouts (Figure 3.2(b)).

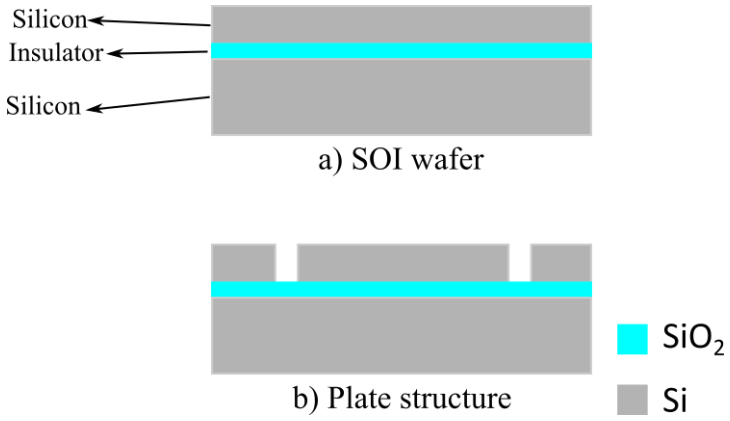

Figure 3.2. Microfabrication of resonator

On the other side, glass wafer is wet etched with hydrofluoric (HF) acid solution. Wet etching is not expected to result in vertical walls. This step forms plate anchors which supports completely free plates from intersection of nodal and centerlines (Figure 3.3(b)). Later, gold (Au) electrodes are deposited on glass wafer but first chromium (Cr) is evaporated since gold is not suitable to stick to surface of glass wafer. Deposition of metal electrodes can be seen in Figure 3.3(c) and (d).

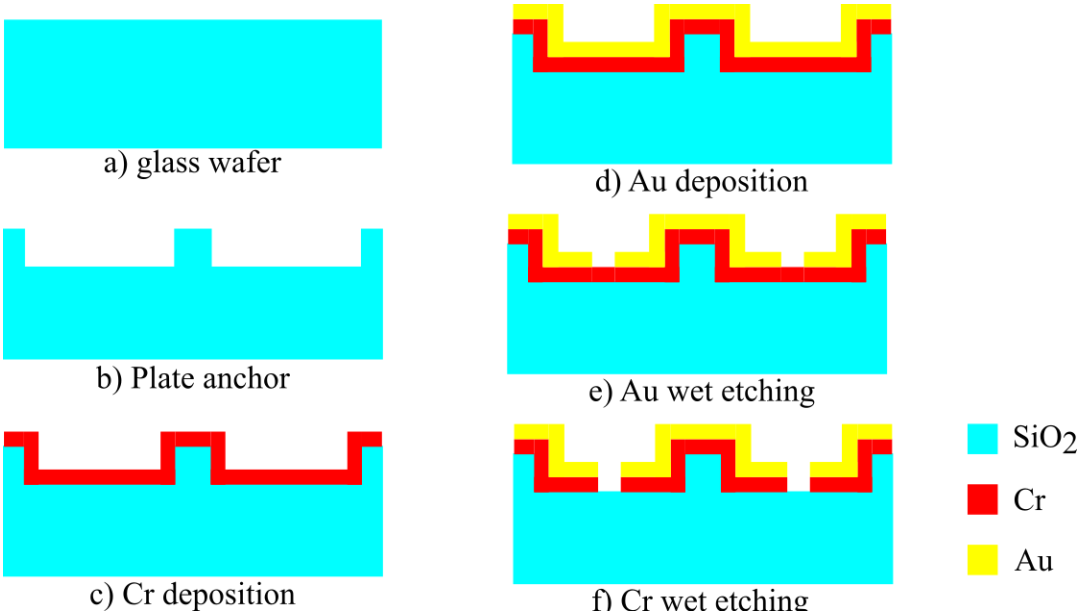

Figure 3.3. Glass wafer fabrication steps

Gold exhibits high stiction to chromium which is far more suitable material for glass wafer. Therefore, chromium is first vapor deposited on glass wafer and then gold is vapor deposited on chromium. Design of electrodes is patterned and gold is wet etched. After wet etching of gold, chromium is also wet etched (Figure 3.3(f)). At the end of all these steps, single crystal silicon (SCS) plates are on top of SOI wafer while electronic connections are formed on glass wafer.

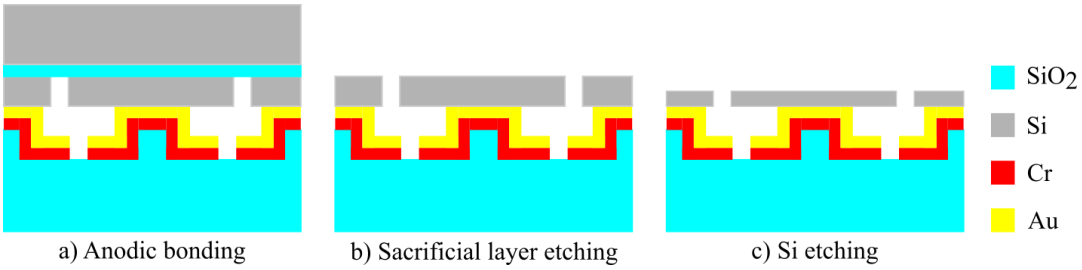

Figure 3.4. Anodic bonding and etching of sacrificial layers

In order to unite these two wafers, anodic bonding is applied (Figure 3.4(a)) but surfaces of wafers have to be flawless and neat. These two requirements are guaranteed by fabricating devices in clean rooms, which are free of dust and other contaminants owing to well isolation, and cleaning surface of wafers with a strong acidic solution. Subsequently, silicon and glass layers of SOI wafer is etched away to release plate resonators so that they are free to move (Figure 3.4(b)). Moreover, device layer is also wet etched in order to considerably reduce thickness of the plate to satisfy thin plate assumptions (Figure 3.4(c)). Not all of the microfabrication process details are provided in this chapter. Detailed explanation of the fabrication process is already provided by Pala[58].

3.2 Fabrication results

Previously, design and microfabrication process flows are explained. Unfortunately, microdevice fabrication is one of the most expensive and hard aspects of the MEMS. Even though, every step is applied according to process flow, plates with flaws are inevitable. Furthermore, it is possible to encounter defects in metal electrodes.

Solution to microfabrication defects is to optimize process flow and determine parameters for each step, e.g., duration of wet etching. However, there is not enough budget nor time for optimization of microplate fabrication. Instead of optimizing, several microplate arrays are produced and ones with less defects are selected for tests.

Quality of microfabricated array of microresonators is inspected through a probe station. The main advantage of the probe station is to isolate small vibration by virtue of pressurized gas. Therefore, it is possible to position small needles called probes on the chip and touch mechanical parts to check whether plate resonators are free to vibrate or not. Even it is possible to apply excitation signal and capture sense signal through probes. However, it is not possible to test plate resonators in atmospheric pressure because these microplates are highly influenced by gas damping.

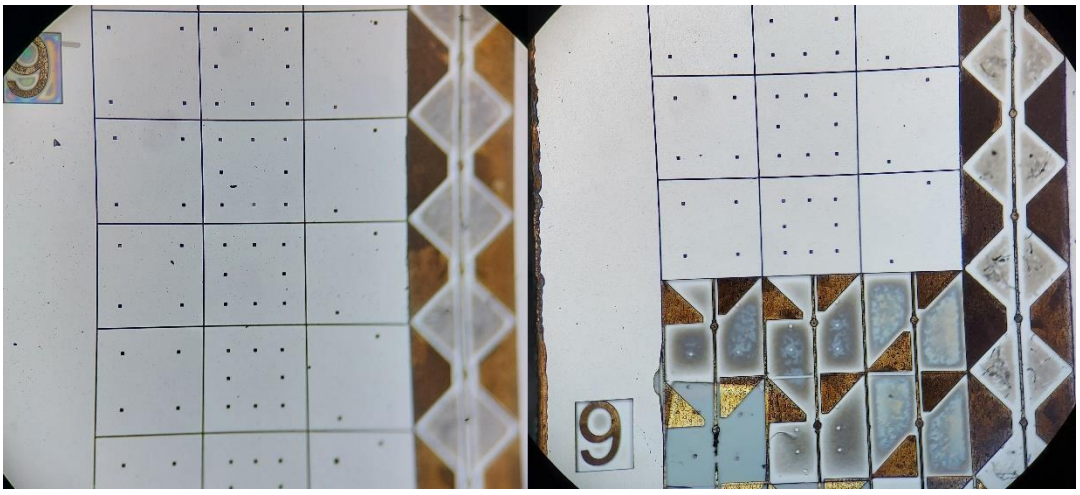

Figure 3.5. Microfabrication results

Figure 3.5 illustrates successful microfabrication results along with some defects. On the left picture an array of plate resonators without any visible defects. However, it is seen that rest of the plates just below that fruitful plates are washed away. The reason for broken plates can be long time of wet etching. A logical solution is to decrease time of wet etching. Fortunately, proof mass metal electrodes of the middle and last array are observed to be in good condition unlike the first column.

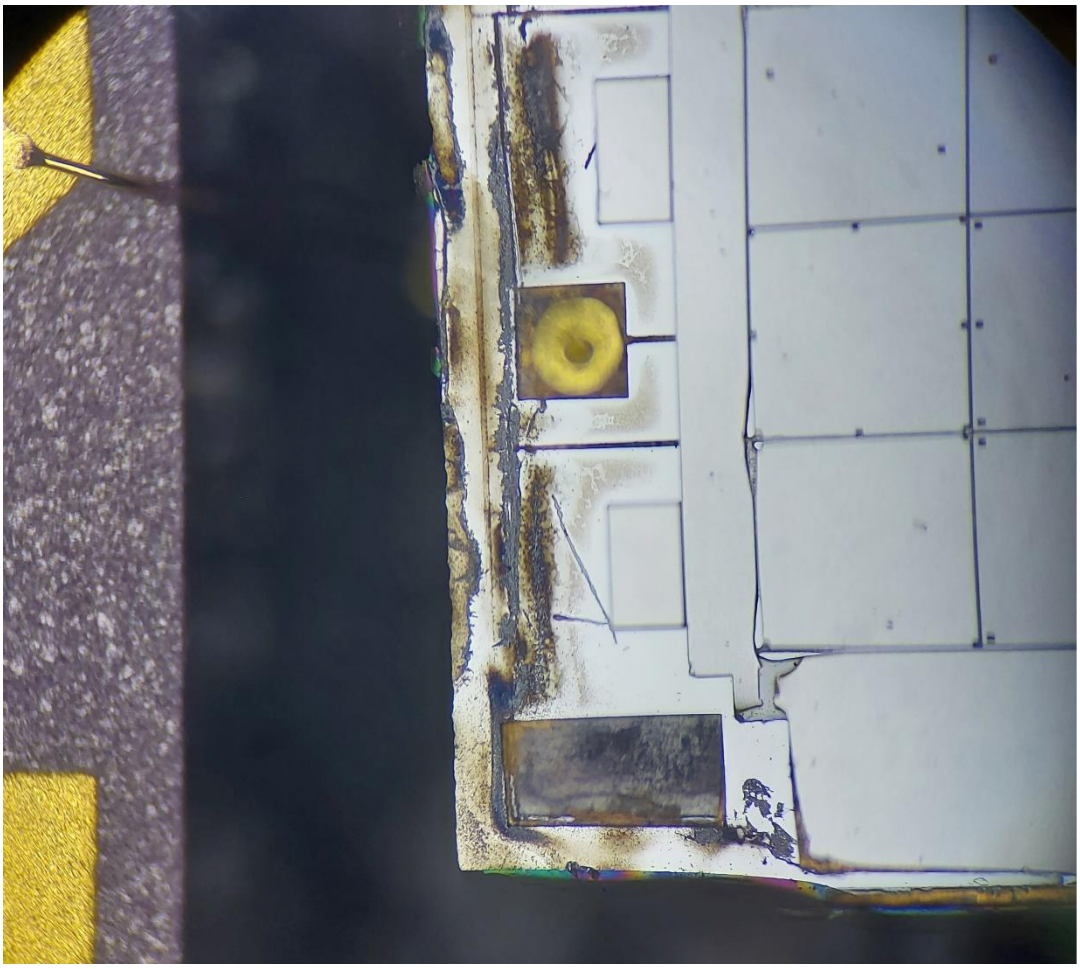

Figure 3.6. Damaged signal pad

Similar to proof mass paths, one of the signal pads is completely damaged as shown in Figure 3.6, preventing it from carrying excitation or sense signals. Unluckily, most of the chips fabricated shows similar flaws. Especially, at least of one of the signal pads is damaged in all of the chips. The main reason for damaged signal pad can be interpreted as dicing because of the fact that faulty metal electrodes are always positioned close to edge of the plate whereas signal pad without ruptures is located in between demonstration plates. Solution to this problem is to position signal pads away from the edges in the design phase.

In order to prepare chips for tests, excitation signal is connected to metal electrodes without any disconnection. On the other hand, sense signals are collected through paths passing under plates although quality of wire bonding to tiny paths is questionable.

Electrical connections are achieved through ball bonding with a semi-automatic wire bonder called TPT HB16. This device uses 25 µm gold wire and ultrasonic forces to form a bond between wire and electronic pad. Best efficiency is accomplished with correct process parameters and adequate size of the metal electrode.

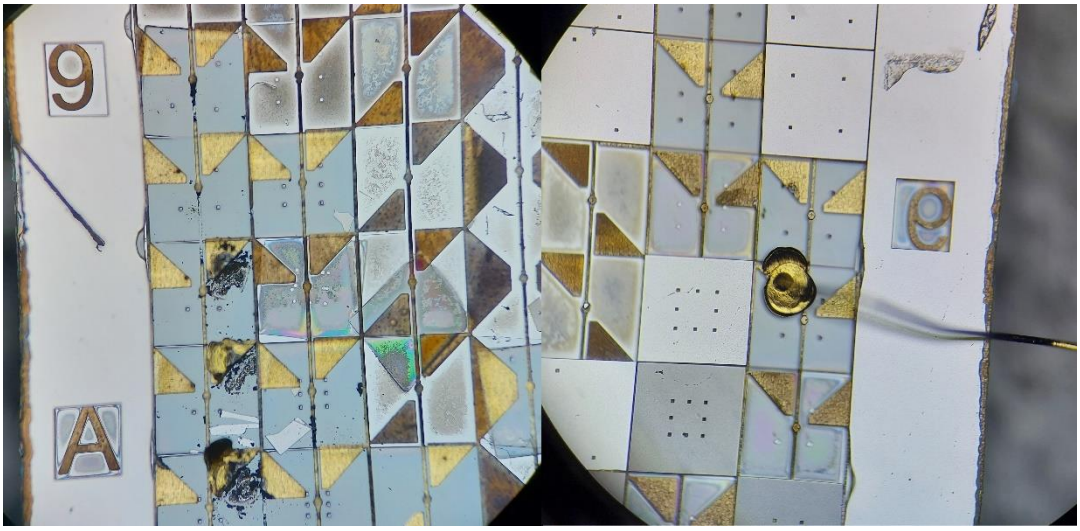

Figure 3.7. Failed and successful wire bonding attempts

As it is seen from Figure 3.7, wire bonding to tiny paths and electrodes underneath the plates is challenging since wire bonder applies ultrasonic force to form connection between pad and wire. Even path is at the risk of being damaged while wire bonding is applied since excessive ultrasonic force is harmful for the path as shown in left picture of Figure 3.7.

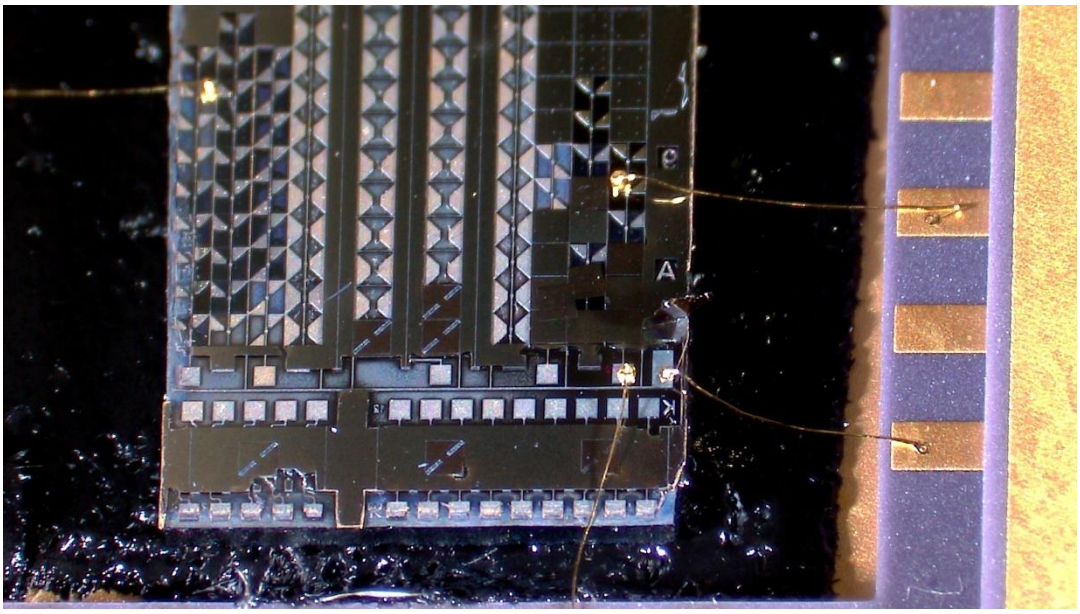

Figure 3.8. A successful wire bonding attempt

After wire bonding, short circuit test is carried out since broken plates cause undesired electrical connections between different pads. Figure 3.8 shows a successful chip ready to be tested for resonance frequency.

3.3 Test setup

Test setup comprised of three subsystems: temperature controller setup, frequency response function setup and vacuum. The first setup consists of a computer, a LM35DZ temperature sensor, thermoelectric cooler (TEC) and NI PCI-4461 data acquisition card (DAQ). Purpose of the first subsystem is to precisely control temperature of the chip so that frequency tests are conducted at constant temperature. FRF setup consists of several DC power supplies and a network analyzer named Keysight E5061B. Aim of the second subsystem is to excite plate resonators with different frequencies and capture responses. Later, Bode diagrams are plotted using known excitation and response of the system. By sweeping through frequency ranges determined by analytical model, resonance frequency of the plates with cutouts are determined. Last subsystem is made up of a vacuum chamber, vacuum pump and a

turbomolecular vacuum which utilizes magnetic levitation to rotate rotors at high speeds to further decrease pressure inside the vacuum chamber.

3.3.1 Temperature controller

The purpose of the temperature controller mechanism is to keep chip at the constant temperature so that temperature sensitivity of the plates is tested and effect of the temperature change on the plate vibration is observed. In order to measure ambient temperature a sensor named LM35DZ by Texas instruments is utilized. However, number of air particles in the vacuum chamber is so low that temperature sensor is not able to measure ambient temperature without conduction. Thus, temperature sensor is directly placed underneath the chip with a thermal pad of 0.5 mm thickness and thermal conductivity of 8 W/mK. Thermal pad prevents formation of air gaps between sensor and chip to measure chip temperature precisely.

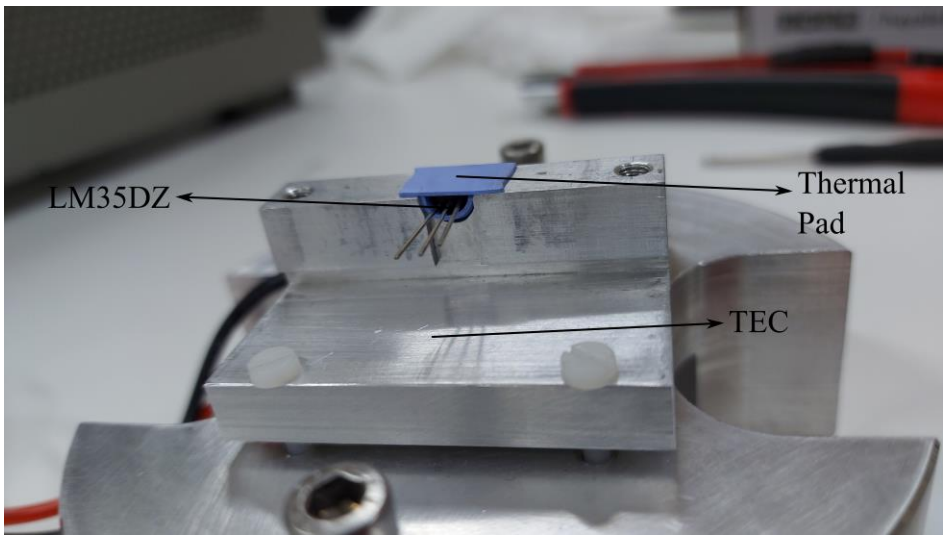

Figure 3.9. Temperature sensor placement

In this setup, a thermoelectric cooler (TEC) named TEC1-12710 is placed just beneath the aluminum surface as shown in Figure 3.9. TEC capable of transferring heat from upper side to down side forming a temperature difference between chip and heat sink. Thus, cooling of the chip is achieved through current control of the

thermoelectric cooler. Later, readout circuit is placed on top of the temperature sensor and chip is pressed to temperature sensor and aluminum block using two bolts (Figure 3.10). Control of the TEC is carried out by a programmable power supply E3640A. Power supply is connected to computer via USB type A/B cable. Then, commands written in SCPI is sent to power supply. Hence, real time control of the cooling power is attained. Lastly, a digital PID controller is written in MATLAB. MATLAB script captures temperature data from DAQ, compares it with desired temperature, calculates necessary current and sends calculate current to power supply.

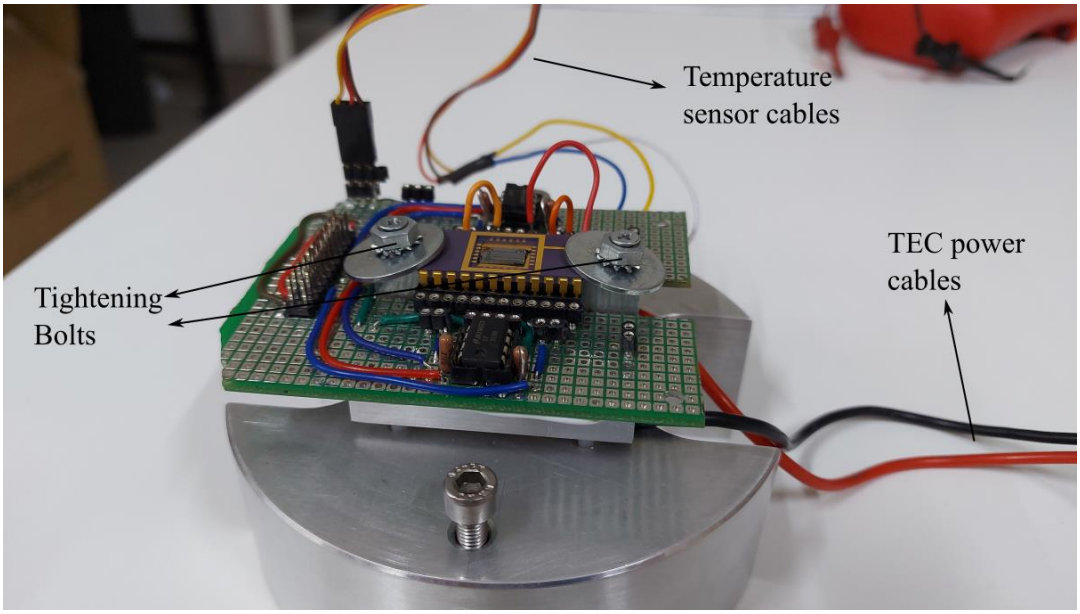

Figure 3.10. Chip ready to be tested

LM35DZ is an analog temperature sensor with a sensitivity of 0.5 ˚C. NI DAQ plugged to computer captures the output of the sensor with a 204.8 kS/s. However, mean value of each 20.4 kS is calculated in MATLAB since thermal fluctuations and noise from electronic devices is able to cause sudden signal rises and declines. As a result, digital PID controller receives temperature data per 0.1 second and similarly sends calculated current value to DC power supply at 0.1 seconds intervals.

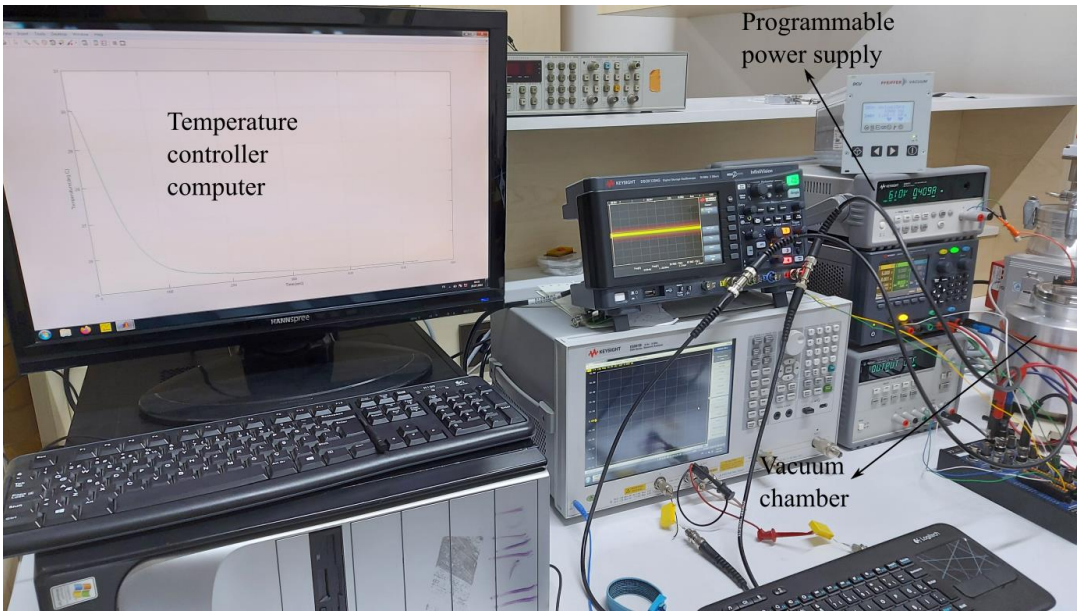

Figure 3.11. Temperature controller setup

With the setup shown in Figure 3.11, it is possible to stabilize temperature of the chip around 25 ˚C within 500 seconds. A typical temperature response of the chip is given below.

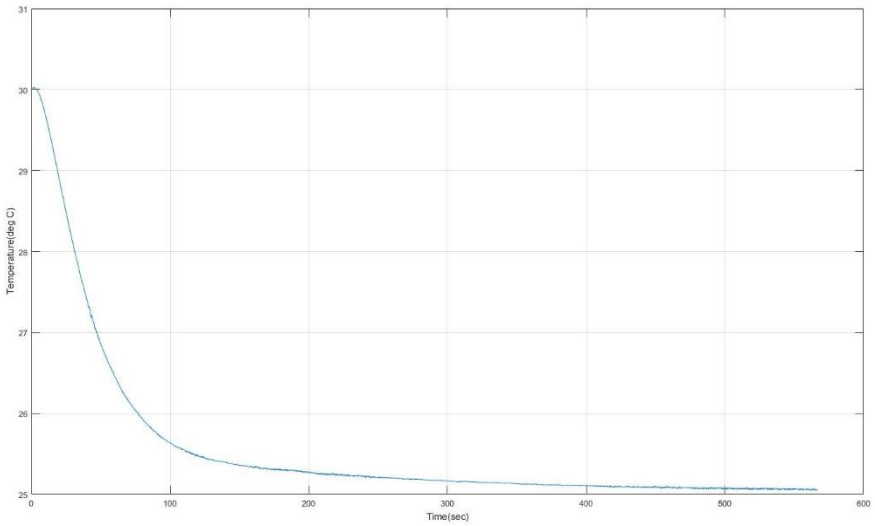

Figure 3.12. Response of the chip temperature for T_{set} = 25 ˚C

It is deducted from Figure 3.12 settling time of the system is short. However, there exists steady state error which can be caused by saturated integral controller. Yet, 0.5 ˚C accuracy for temperature controller is sufficient for experiments in this thesis.

3.3.2 Frequency response function setup

In order to test array of plate resonators, both amplitude and phase response of the plate resonators are necessary. Network analyzer is an electrical device which is able apply electrical sinus signals with certain frequencies and collect response of the system. After sweeping through a range of frequencies, amplitude and phase response of the system is computed as complex numbers by network analyzer. Later, these complex numbers are plotted as two different graphs called gain-phase or Bode diagrams. Keysight E5061B Network analyzer is used in this study, which is a multifunctional device even able to apply proof mass voltage from one of its ports.

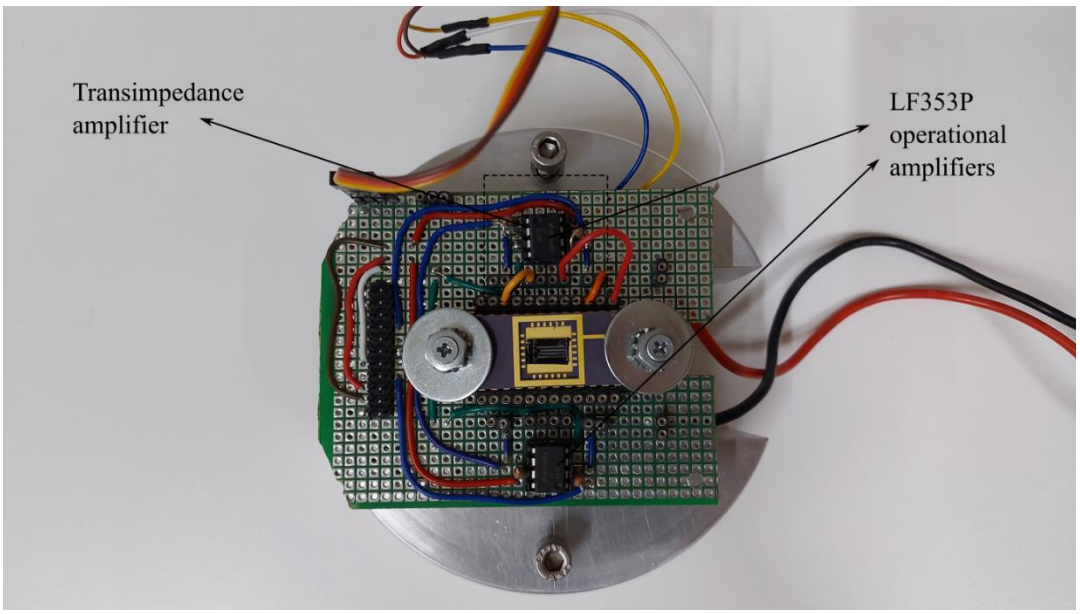

Figure 3.13. Readout circuit

A driving AC signal is applied to one of the metal electrodes as shown in Figure 2.13 while proof mass voltage SCS plate resonator what is conductive. Output of the plate vibration is current as explained under capacitive actuation and sense heading.

However, output and inputs of the network analyzer is voltage. Hence, conversion of current to voltage is necessary. Current to voltage is converted by virtue of transimpedance amplifier. Not only conversion is achieved but also signal is amplified with feedback resistance of 1 MΩ. LF353P by Texas instruments is soldered to circuit board as an operational amplifier. Overall, 2 pieces of LF353P is on the readout circuit meaning there are 4 operational amplifiers available on the circuit board. As several arrays of plate resonators are present on each chip, it is possible to wire bond several lines and test each one easily. In order to supply power to operational amplifiers, Agilent E3631A DC power supply is used, which is able to provide symmetrical DC voltage necessary power up transimpedance amplifier.

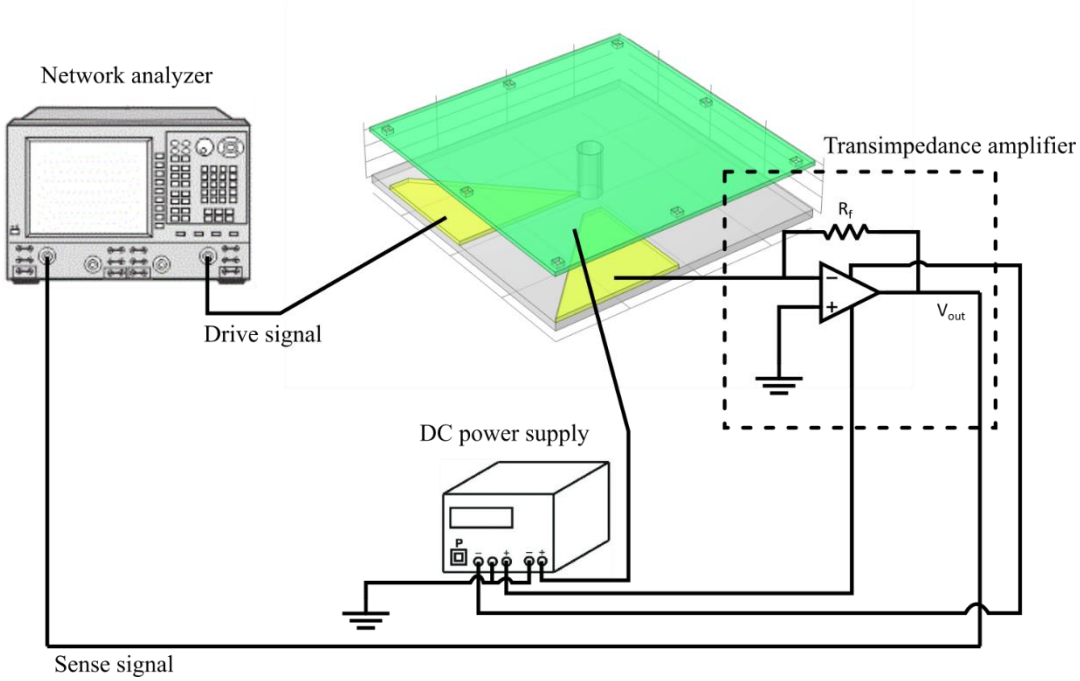

Figure 3.14. Complete illustration of the test setup

A simplified model of the test setup without temperature control setup is shown above. Array of plate resonators is denoted with a simple plate drawing. In summary, network analyzer applies AC drive signals from one of the ports and gathers response of the array from other port. Later, divides response of the device under test (DUT) by applied signal to calculate gain and phase values. Repeating the same procedure

for a range of frequencies results in plots called Bode diagrams. Gain diagram is conventionally plotted in logarithmic scale.

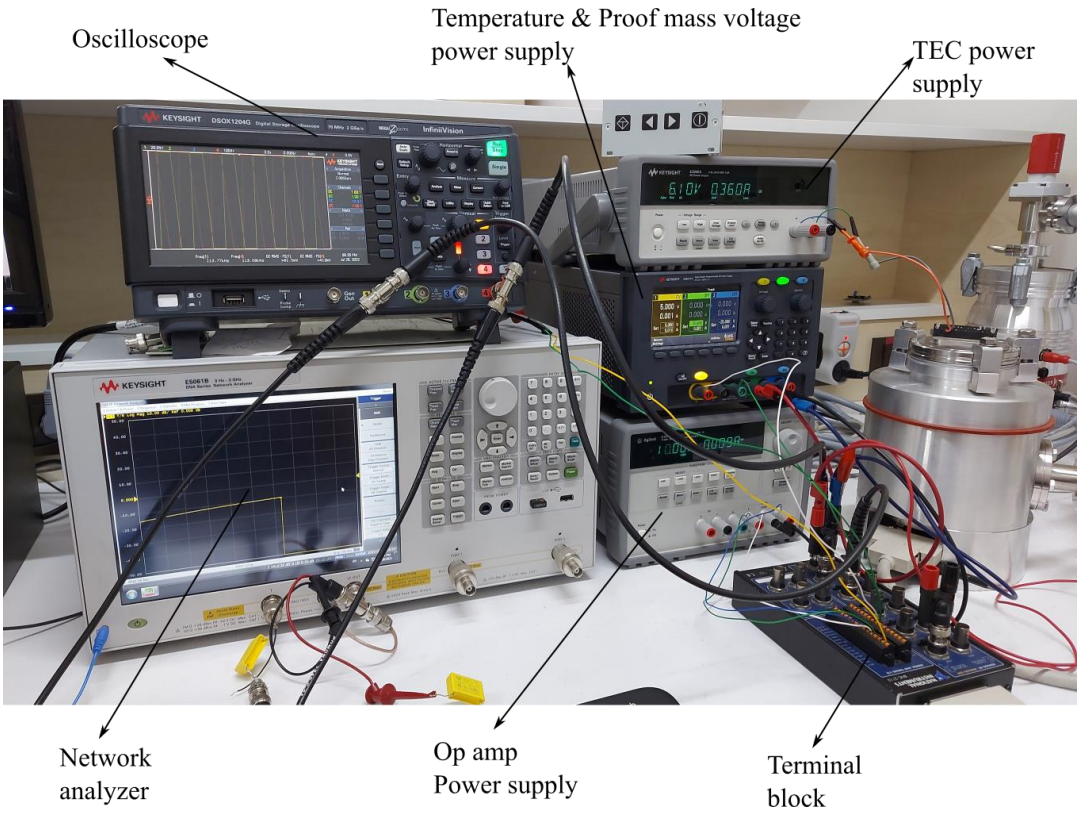

Figure 3.15. FRF test setup

Apart from above power supply, another DC power supply is to provide voltage to both plate proof mass pad and LM35DZ temperature sensor. Proof mass voltage is chosen to be given from a standalone power supply rather than network analyzer as there is always a voltage leakage from these devices. Nonetheless, it is possible to form a short circuit between positive and negative ends of the proof mass pads with standalone power supply since it is simply plugging ground banana cable in proof mass banana cable. Task distribution of different power supplies are shown in Figure 3.15.

An oscilloscope is also added to test mechanism to observe applied and read sinus signals. With the help of oscilloscope, detection of short circuits and other defects are possible straightforwardly.

Shielded terminal block is utilized to send and receive signals without interference. Terminal block is compatible with BNC (Bayonet-Neill Concelman) connectors. Shielding against inference is one of the most prominent features of BNC cables. Therefore, it is made sure that drive and sense signals are carried with BNC cables rather than simple ones to prevent gathering incorrect data.

3.3.3 Vacuum setup

Vacuum is achieved with through two steps. In the first step, a simple vacuum pump is started to drop pressure below 70 mTorr inside aluminum vacuum chamber. After pressure drops below 75 mTorr, turbomolecular pump is started since starting above that pressure level is destructive for critical parts such as magnetically-levitated rotor. In the second step, it almost takes 10 minutes to reach pressure levels below 1 mTorr. However, after certain pressure value (1 mTorr), pressure inside the vacuum chamber is fixed. Test can be conducted after reaching the constant pressure level.

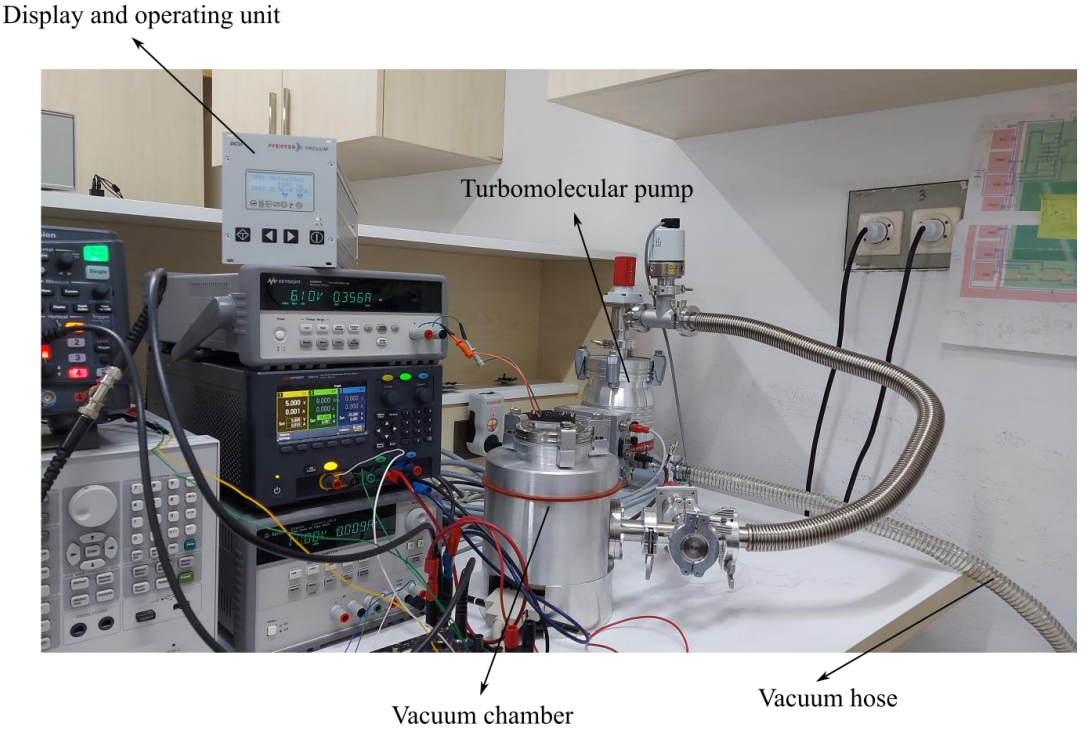

Figure 3.16. Vacuum system

Vacuum chamber is one of the parts that should be given upmost care since condition of the vacuum chamber directly effects the minimum achievable pressure with vacuum and turbomolecular pumps. For instance, touching assembly surfaces of the vacuum chamber should be avoided because small dirt and body fats hinders the perfect sealing between lid and vacuum chamber causing gas leakage into chamber.

Vacuum pump is placed on top of a foam in order to isolate vibration of vacuum pump. Vacuum pump is connected to turbomolecular pump with vacuum hose. On the other hand, connection between turbomolecular pump and vacuum chamber is a stainless-steel vacuum hose as shown in Figure 3.16.

After preparing each subsystem, chip is mounted to readout circuit. An FC26P connector with 25 pin flat cable is plugged to readout circuit. Other end of the flat cable is a connector called D-SUB which compatible connector placed at the top and bottom of the vacuum chamber. Thanks to electrical connections in vacuum chamber, readout circuit is successfully connected to terminal block.

3.4 Experiments and results

After preparing test setup, one of the specimens is placed inside the vacuum chamber. Short-circuit is checked with a multimeter and it is made sure that every subsystem of the test setup is functional.

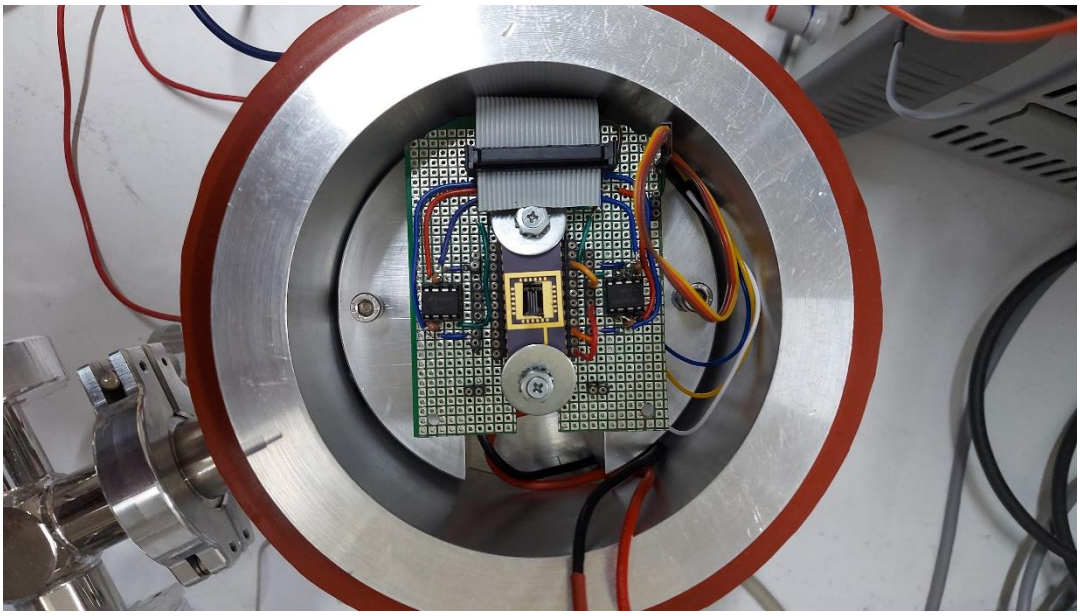

Figure 3.17. DUT inside the vacuum chamber

Device under test is a chip with a functional array of K-plates. Even though, several plates seem to be free to vibrate. Most of the plates washed away during wet etching. Only microplates with cutout positions of 140, 60, 20, 10, 0 µm along with a reference plate (without any cutout) are visible. Yet, reference plate and l = 20 µm don't seem to be vibrating. The reason for not responding might be unetched sacrificial layers under microplates or being adjoint to L-plates and substrate around the plates.

In this part of the thesis, three experiments are conducted: proof mass voltage sweep, frequency response function of several plates on the same array and temperature sweep for only one plate.

3.4.1 Proof mass voltage sweep

After placing chip inside the vacuum chamber and starting vacuum pump, all electrical connections are made with the help of shielded terminal block. Even though specimen has 4 actively vibrating plates, only one of them is focused to clearly observe effect of changing proof mass voltage. Too large excitation voltages are not preferred in order to avoid nonlinear vibrations. With previously performed tests, it is clear that nonlinear responses observed for excitation voltages greater than -25 dBm. To be on the safe side, -30 dBm is selected from Keysight Network Analyzer.

Starting from proof mass voltage of 50 V, frequency response is recorded with each proof mass voltage decrease for a narrow band in which there is only one resonance.

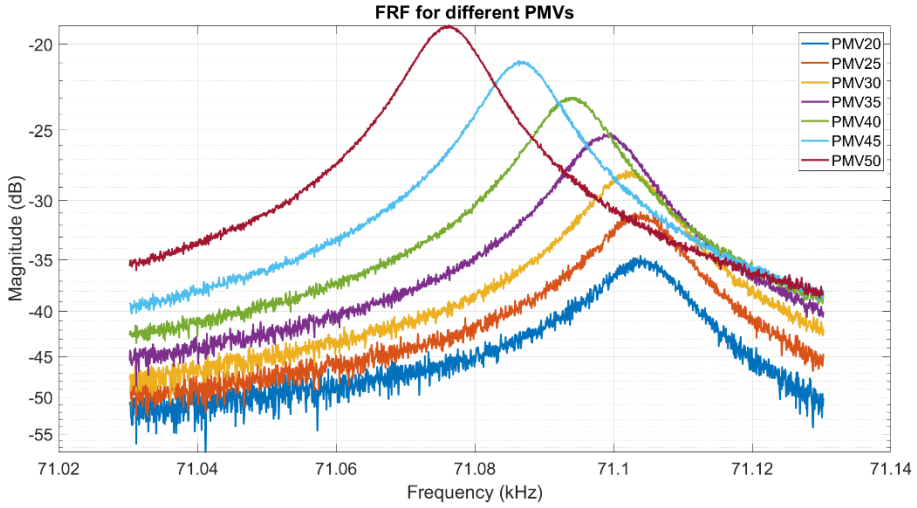

Figure 3.18. Proof mass voltage sweep for l = 60 µm

At first glance, it is obvious resonance frequency of the microplate resonator decrease with rising proof mass voltage. Such a result is expected as derived in analytical model. This phenomenon is called electrostatic softening effect. Although signal to noise ratio goes up with larger proof mass voltage, it is not logical due to uncertainties in microfabrication process flow. A damaged post plate could lead to

collapse of a microplate resonator, forming short-circuit. Since maximum voltage of network analyzer is 42 V, any kind of short-circuit should be avoided.

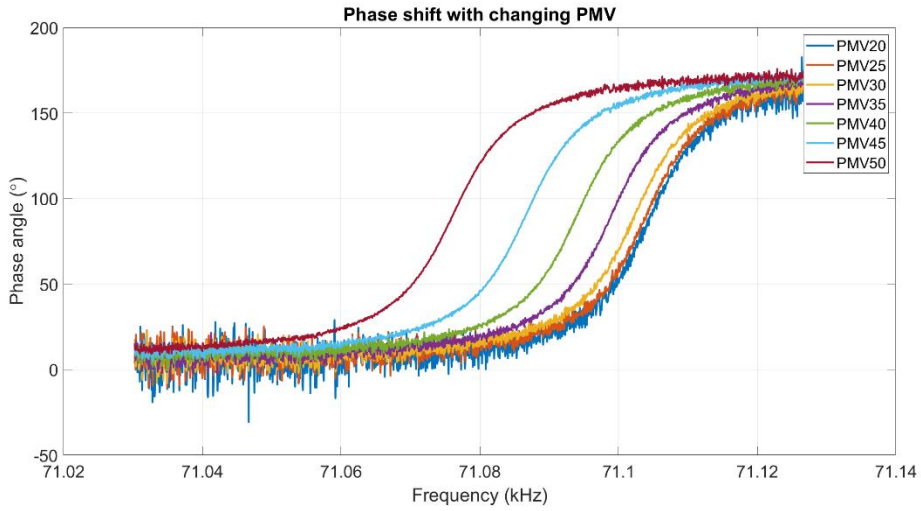

Figure 3.19. Phase response for different proof mass voltages

Phase response of the microplate resonator shows a similar trend by shifting towards lower frequencies. Since 50 V proof mass voltage is utilized for the study. A resonance frequency of 71.076 kHz with a quality factor of 5300 can be deduced for this microplate resonator.

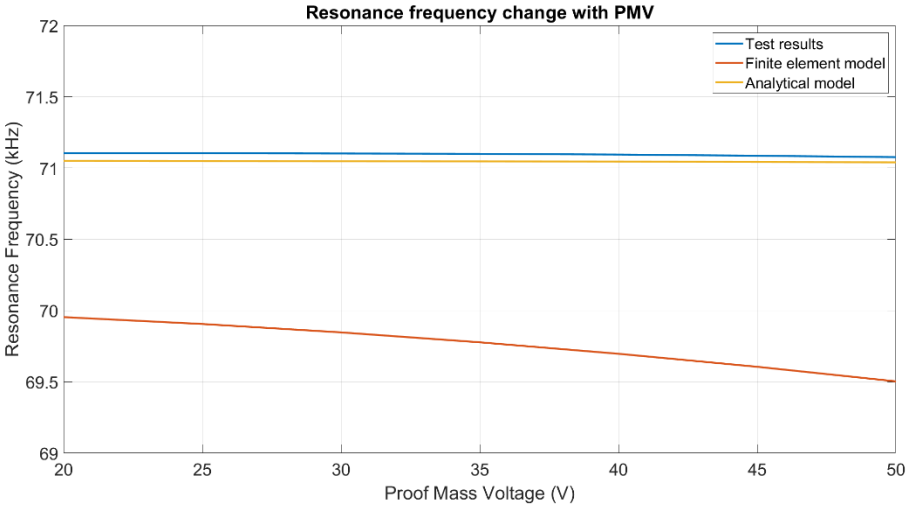

Figure 3.20. Comparison between test and models

According test data and analytical model, relative error between them doesn't exceed 2.5%. As for the finite element model, results perfectly agree with each other. Both analytical and finite element model predicted a slight decrease in resonance frequency as proof mass voltage increases. This slight prediction is verified by test results.

3.4.2 Frequency shift due to cutouts

Array of microplate resonators with cutout positions 140, 60, 10 and 0 μm are connected in series with each other. In other words, it is possible to excite all of them from one gold pad while response of each microplate resonator is collected from only one pad. In order to detect resonance frequencies, a FRF is taken from 5 Hz to 100 kHz. Resonance frequencies are seen around 71 kHz. A second frequency response function is recorded between 70 kHz and 73 kHz with a proof mass voltage of 50 V.

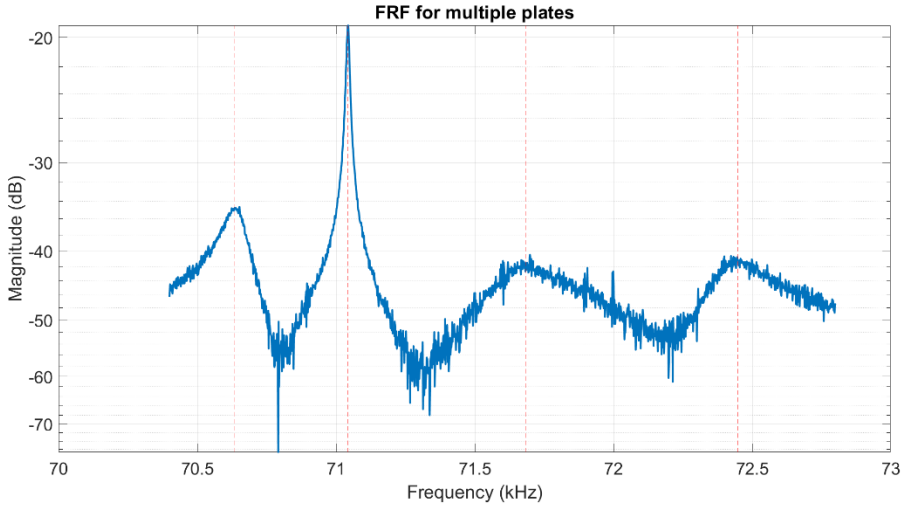

Figure 3.21. FRF between 70 kHz and 73 kHz

As previously stated, several plates do not respond to capacitive actuation due to microfabrication flaws. It is made sure that these peaks are microplate resonators by changing proof mass voltage and observing resonance frequency shift.

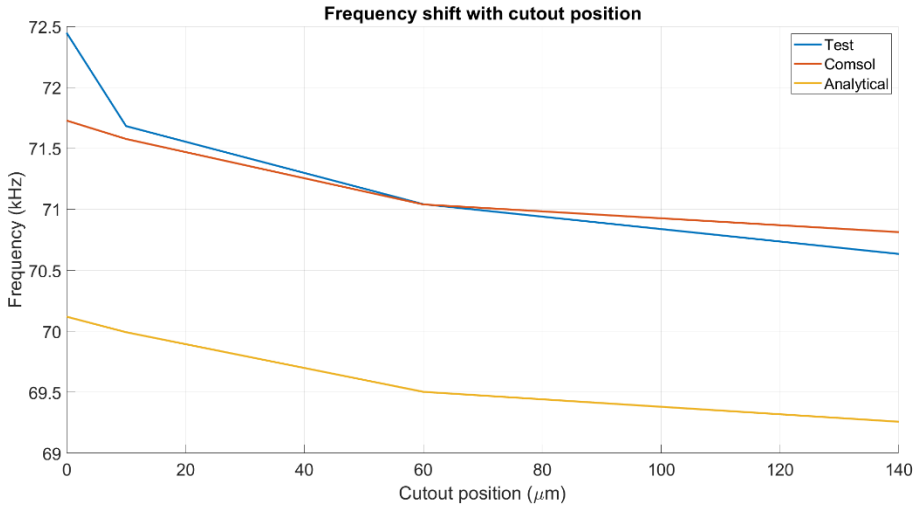

Figure 3.22. Comparison between test and models

Similar to proof mass voltage tests, COMSOL and test results exhibit high consistency while analytical model persists a similar relative error smaller than 3.5%. Especially, resonance frequency of cutout position of 0 µm is higher than both COMSOL and analytical model. The reason behind such a huge difference might be different thickness of the microplate or unsuccessful etching of plate edge since resonance frequency increase is highly influenced by thickness and boundary conditions.

Overall, these array of microplate resonators are in agreement with models developed in Chapter 2 despite the fact that microfabrication flaws prevent high quality factors.

3.4.3 Resonance frequency shift due to temperature rise

Up to this point, temperature of the system is fixed at 25 ˚C with the help of thermoelectric cooler. In this part of tests, another microplate is used since previous resonators stopped responding after intensive testing. Thus, resonance frequency of the microplate is around 78.6 kHz rather than 71 kHz. After determining whereabouts of resonance frequency, temperature of chip is increased from 25 ˚C to

32 ˚C step by step. In each step, system is kept on hold at least 5 minutes to let temperature of vacuum chamber stabilize around desired temperature. Similar to 2nd test conducted, proof mass voltage of 50 V is applied.

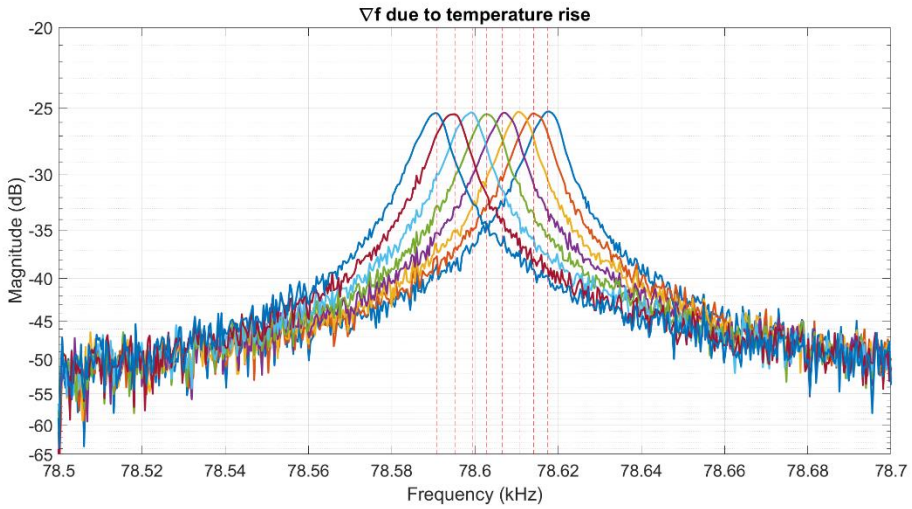

Figure 3.23. Frequency shift due to temperature rise

Above figure illustrates frequency response function of the same microplate at different temperatures. While the rightmost peak is recorded at 25 ˚C, peak of the resonance shifts towards right with increasing temperature. As a result, the leftmost peak data is collected at 32 ˚C.

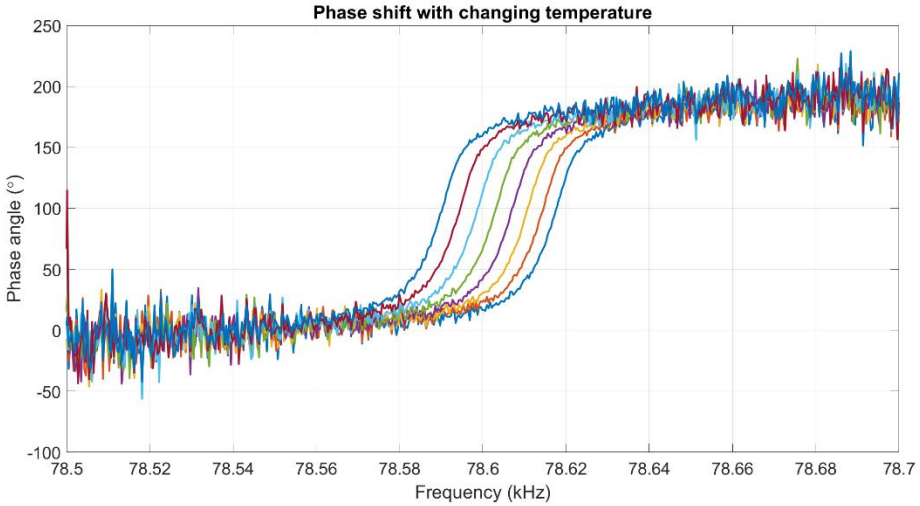

Figure 3.24. Phase angle shift with rising temperature

Figure 1.1 illustrates phase angle of the microplate resonator with temperature change. As expected, 90˚ phase shifts towards lower frequencies with increasing temperature.

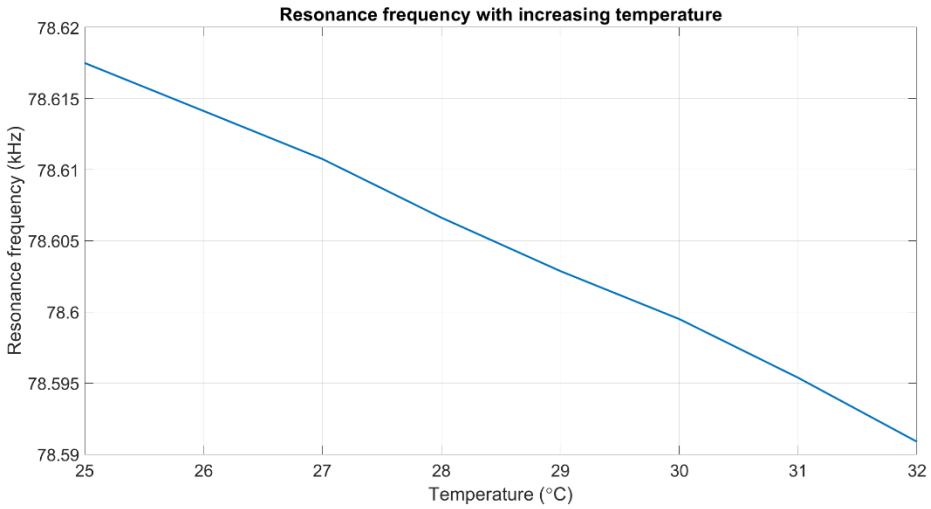

Figure 3.25. Frequency decrease with each step

According to Figure 3.25, an average of 3.8 Hz decrease is observed with each step. Therefore, it can be deduced that resonance frequency and temperature change exhibits almost linear relation. While temperature sensitivity is found to be ~3.8 Hz/˚C, it is calculated to be 4 Hz/˚C by COMSOL and 2 Hz/˚C by analytical model. However, it should be noted that both of these coefficients calculated by models are for t = 1.61 µm thick plate. It is for sure thickness of this plate is more than 1.7 µm. Hence, discrepancy between models and microplate test can be dealt by finding a microplate with less microfabrication flaws.

Lastly, quality factor of this plate is measured to exceeding 9000. This result is impressive compared to microplates previously tested. It implies duration of wet etching is detrimental to microplate structure since none of the plates with thickness of 1.61 µm has achieved a quality factor close to this number.

CHAPTER 4

CONCLUSION AND FUTURE WORK

In this thesis, an array of microplate resonators with adjustable resonance frequency is designed. Adjustment of resonance frequency is achieved through deliberate cutouts placed at unique positions on the plate. Analytical modelling of the plate is done with the help of semi-analytical methods along with finite element modelling to compute resonance frequency of each element of the array. Microfabrication and characterization tests are conducted to prove consistency between models and tests. Summary of each step along with conclusions are given below:

- Demand for MEMS devices, application areas along with resonators are investigated. Different type of resonators with high quality factor is listed and discussed. Later, resonant sensors and their advantages are discussed with example area of applications. A literature survey has been conducted to investigate state-of-the-art resonant temperature sensors and compare them with each other. At the end, infrared radiation sensors discussed and need for resonant thermal detectors is justified.
- Microplate resonators with cutouts are introduced as resonant temperature sensors. Flexural modes are selected over bulk modes because resonance frequencies of bulk modes are rather high and low surface-to-volume ratio hinders its use as a sensor. First two modes are selected to be mode-of-interest since resonance frequency greatly increases and microplate displacement decreases with increasing number of modes. As higher modes have more nodal lines compared lower ones, displacement area decreases and current induced by microplate vibration does so.
- Transverse vibration of microplate is modelled with the help of Rayleigh-Ritz method to calculate resonance frequencies while any kind of energy loss is omitted. Effect of cutouts is taken into account with a rather simple method

by just subtracting their strain and kinetic energies from total energy of the mod. Later, a parametric finite element model is drawn in COMSOL to easily analyze two different designs called L-plate and K-plate designs. Only difference between them is the number of cutouts. It turns out that microfabrication of only K-plate is successful. Thus, K-plates are focused for the rest of the study. Discrepancy between analytical and COMSOL models can be attributed to not including post plate in analytical model. Yet, relative error between them is smaller than 2.5%, making analytical model credible.

- Thermal and electrical effects are included into analytical model with simple modelling such as only expansion of material and coefficient of Young's modulus of Si are utilized to model temperature change. On the other hand, simple capacitance and electrostatic force equations seem adequate to simulate electrical effects such as electrostatic spring softening effect. In this manner, 4 Hz/˚C and 2 Hz/˚C temperature sensitivities are computed by finite element and analytical models, respectively.
- Microfabrication process flow is explained in detail along with possible flaws which can be caused by process flow and simple solutions are proposed. Fabricated specimens are investigated under wire-bonder and probe station and several problems regarding produced parts are pointed out. In order to overcome such flaws, a different approach is explained and attempts are shown. Wire-bonding of chips to DIP packages is a challenging step due to damaged pads. Even though, several work arounds are tried, most of the end-results failed to show response under test. Lack of differential drive pad, presence of too many plates on the same array and damages caused by dicing steps to gold electrodes seem to be problem related to microfabrication. Another important problem is stiction between plates and substrate occurring after wet etching step. These problems could be easily dealt with a considerate design step beforehand. Unfortunately, microfabrication process flow is long and costly step which is not possible to repeat.

- In the last part of the thesis, test setup is explained in detail which consists of a vacuum system, a FRF setup and temperature controller. In order to correctly measure temperature of specimen, temperature sensor is tightly pressed to DIP package by means of two bolts since it is not possible measure temperature inside the vacuum chamber in absence of air. All of the tests are conducted under 1 mTorr in order to eliminate damping on microplates. It is shown that Q-factors over 9000 is achievable with microplate resonators. However, flaws occurred during wet etching step seems to be main reason Q-factors as low as 300. Moreover, uncertainties of wet etching results in variation of plate thickness even in the same array of microplate resonators. Temperature sensitivity of a microplate resonator is measured to be 3.8 Hz/˚C, which is close to values calculated by COMSOL and analytical models.
- FRF of an array of 4-microplate resonator proves to be consistent with finite element and analytical model. Yet, discrepancy between analytical model and test result can be attributed to not including anchor. According to test results and models, it is possible to shift resonance frequency of a microplate resonator up to 140 Hz by simply changing position of cutouts along diagonal lines.

4.1 Future work

Apart from these achievements, following improvements and work can be done to enhance microplate resonators with adjustable resonance frequency.

- Plate post should be included into analytical model by searching literature for similar problems so that discrepancy between finite element model and analytical model is reduced.
- Microfabrication process should be optimized to eliminate uncertainties regarding plate thickness, etching of sacrificial layer and detachment from other plates.

- Design of the array should be improved to increase yield. For instance, addition of a differential drive electrode is an essential tool to solve parasitic feedthrough capacitance problem. Similarly, failure or detachment of a microplate completely disables an array since plates are too close to each other causes short-circuit between electrodes. Gold electrodes should be placed away from the edge of the chip since nearly all of the sense pads are damaged due to dicing.
- A PLL control should be applied to continuously track resonance frequency of a microplate so that stability of microplate vibration could be checked and temperature resolution of microplate resonator can be determined.
- A complex PLL control should be applied to continuously track several resonance frequencies of microplates so that a matrix of microplate resonators could be used as an IR sensor.

REFERENCES

[1] R. P. Feynman, “There’s plenty of room at the bottom,” in *Micromechanics and MEMS: Classic and Seminal Papers to 1990*, 1997, pp. 2–9. doi: 10.1109/9780470545263.sect1.

[2] F. M. Kaplan, “1959 : the year changed everything,” p. 322, 2009.

[3] A. N. Saxena, “Invention of integrated circuits: Untold important facts,” *Invention Of Integrated Circuits: Untold Important Facts*, pp. 1–523, Jan. 2009, doi: 10.1142/6850.

[4] P. Rai-Choudhury, “MEMS and MOEMS Technology and Applications,” 2000, Accessed: Jun. 07, 2022. [Online]. Available: https://books.google.com/books?hl=tr&lr=&id=v6KOTaI2DhAC&oi=fnd&pg=PR9&dq=mems+and+moems&ots=FD2EXbZdpS&sig=9Yu_nITCchZLJTEx6XypPoA0fAw

[5] “Harvey C. Nathanson, Inventor of the First MEMS Device, Dies at 83 - IEEE Spectrum.” https://spectrum.ieee.org/harvey-c-nathanson-inventor-of-the-first-mems-device-dies-at-83 (accessed Jun. 05, 2022).

[6] H. Fujita, “Decade of MEMS and its future,” in *Proceedings of the IEEE Micro Electro Mechanical Systems (MEMS)*, 1997, pp. 1–8. doi: 10.1109/memsys.1997.581729.

[7] S. (Salvatore) Baglio, Salvatore. Castorina, and N. Savalli, “Scaling issues and design of MEMS,” p. 229, 2007.

[8] Yole Developpement, “Status of the Mems Industry - Market Update 2021,” *Yole Market Update*, 2021. http://www.yole.fr/Status_Of_The_MEMS_Industry_Market_Update_2021.aspx (accessed Jun. 09, 2022).

[9] I. B. of W. and Measures, “The international system of units (SI),” 2001, Accessed: Jun. 16, 2022. [Online]. Available: https://physics.nist.gov/cuu/pdf/sp330.pdf

[10] C. T. C. Nguyen, “MEMS technology for timing and frequency control,” *IEEE Transactions on Ultrasonics, Ferroelectrics, and Frequency Control*, vol. 54, no. 2. Institute of Electrical and Electronics Engineers Inc., pp. 251–270, Feb. 01, 2007. doi: 10.1109/TUFFC.2007.240.

[11] J. T. M. van Beek and R. Puers, “A review of MEMS oscillators for frequency reference and timing applications,” *Journal of Micromechanics and Microengineering*, vol. 22, no. 1, p. 013001, Dec. 2012, doi: 10.1088/0960-1317/22/1/013001.

[12] K. Wang, A. C. Wong, and C. T. C. Nguyen, “VHF free-free beam high-Q micromechanical resonators,” *Journal of Microelectromechanical Systems*, vol. 9, no. 3, pp. 347–360, Sep. 2000, doi: 10.1109/84.870061.

[13] W. T. Hsu and K. Cioffi, “Low phase noise 70MHz micromechanical reference oscillators,” *IEEE MTT-S International Microwave Symposium Digest*, vol. 3, pp. 1927–1930, 2004, doi: 10.1109/MWSYM.2004.1338986.

[14] S. Pourkamali, A. Hashimura, R. Abdolvand, G. K. Ho, A. Erbil, and F. Ayazi, “High-Q single crystal silicon HARPSS capacitive beam resonators with self-aligned sub-100-nm transduction gaps,” *Journal of Microelectromechanical Systems*, vol. 12, no. 4, pp. 487–496, Aug. 2003, doi: 10.1109/JMEMS.2003.811726.

[15] C. T. C. Nguyen and R. T. Howe, “Integrated CMOS micromechanical resonator high-Q oscillator,” *IEEE Journal of Solid-State Circuits*, vol. 34, no. 4, pp. 440–455, Apr. 1999, doi: 10.1109/4.753677.

[16] J. E. Y. Lee, B. Bahreyni, and A. A. Seshia, “An axial strain modulated double-ended tuning fork electrometer,” *Sensors and Actuators, A: Physical*, vol. 148, no. 2, pp. 395–400, Dec. 2008, doi: 10.1016/J.SNA.2008.09.010.

[17] M. H. Li, W. C. Chen, and S. S. Li, “CMOS-MEMS transverse-mode square plate resonator with high Q and low motional impedance,” *2011 16th International Solid-State Sensors, Actuators and Microsystems Conference, TRANSDUCERS’11*, pp. 1500–1503, 2011, doi: 10.1109/TRANSDUCERS.2011.5969683.

[18] K. L. Chen, S. Wang, J. Salvia, R. T. Howe, and T. W. Kenny, “Encapsulated out-of-plane differential square-plate resonator with integrated actuation electrodes,” *TRANSDUCERS 2009 - 15th International Conference on Solid-State Sensors, Actuators and Microsystems*, pp. 1421–1424, 2009, doi: 10.1109/SENSOR.2009.5285839.

[19] M. U. Demirci and C. T. C. Nguyen, “Mechanically corner-coupled square microresonator array for reduced series motional resistance,” *Journal of Microelectromechanical Systems*, vol. 15, no. 6, pp. 1419–1436, Dec. 2006, doi: 10.1109/JMEMS.2006.883588.

[20] D. Platz and U. Schmid, “Vibrational modes in MEMS resonators,” *Journal of Micromechanics and Microengineering*, vol. 29, no. 12. IOP Publishing, p. 123001, Oct. 25, 2019. doi: 10.1088/1361-6439/ab4bad.

[21] J. Basu and T. K. Bhattacharyya, “Microelectromechanical resonators for radio frequency communication applications,” *Microsystem Technologies*, vol. 17, no. 10–11, pp. 1557–1580, Oct. 2011, doi: 10.1007/S00542-011-1332-9/FIGURES/14.

[22] J. E. Y. Lee, J. Yan, and A. A. Seshia, “Low loss HF band SOI wine glass bulk mode capacitive square-plate resonator,” *Journal of Micromechanics and Microengineering*, vol. 19, no. 7, p. 074003, Jun. 2009, doi: 10.1088/0960-1317/19/7/074003.

[23] J. Wang, J. E. Butler, T. Feygelson, and C. T. C. Nguyen, “1.51-GHz Nanocrystalline diamond micromechanical disk resonator with material-mismatched isolating support,” *Proceedings of the IEEE International*

Conference on Micro Electro Mechanical Systems (MEMS), pp. 641–644, 2004, doi: 10.1109/MEMS.2004.1290666.

[24] A. K. Pandey, O. Gottlieb, O. Shtempluck, and E. Buks, "Performance of an AuPd micromechanical resonator as a temperature sensor," *Applied Physics Letters*, vol. 96, no. 20, p. 203105, May 2010, doi: 10.1063/1.3431614.

[25] M. A. Hopcroft *et al.*, "Using the temperature dependence of resonator quality factor as a thermometer," *Applied Physics Letters*, vol. 91, no. 1, p. 013505, Jul. 2007, doi: 10.1063/1.2753758.

[26] W.-T. Hsu, J. R. Clark, and C. T.-C. Nguyen, "A Resonant Temperature Sensor Based on Electrical Spring Softening," *Transducers '01 Eurosensors XV*, pp. 1456–1459, 2001, doi: 10.1007/978-3-642-59497-7_344.

[27] A. Rogalski, "Progress in focal plane array technologies," *Progress in Quantum Electronics*, vol. 36, no. 2–3. Pergamon, pp. 342–473, Mar. 01, 2012. doi: 10.1016/j.pquantelec.2012.07.001.

[28] C. Cabuz, S. Shoji, K. Fukatsu, E. Cabuz, K. Minami, and M. Esashi, "Fabrication and packaging of a resonant infrared sensor integrated in silicon," *Sensors and Actuators A: Physical*, vol. 43, no. 1–3, pp. 92–99, May 1994, doi: 10.1016/0924-4247(93)00671-P.

[29] Z. Qian, Y. Hui, F. Liu, S. Kang, S. Kar, and M. Rinaldi, "Graphene–aluminum nitride NEMS resonant infrared detector," *Microsystems & Nanoengineering 2016 2:1*, vol. 2, no. 1, pp. 1–7, Jun. 2016, doi: 10.1038/micronano.2016.26.

[30] C. Murphy, "Why MEMS Accelerometers Are Becoming the Designer ' s Best Choice for CbM Applications Accelerometers in CbM Applications." Accessed: Jun. 01, 2022. [Online]. Available: https://www.mouser.in/pdfDocs/WhyMEMSAccelerometers.pdf

[31] R. Abdolvand, B. Bahreyni, J. E. Y. Lee, and F. Nabki, “Micromachined resonators: A review,” *Micromachines*, vol. 7, no. 9. 2016. doi: 10.3390/mi7090160.

[32] S. A. Chandorkar, M. Agarwal, R. Melamud, R. N. Candler, K. E. Goodson, and T. W. Kenny, “Limits of quality factor in bulk-mode micromechanical resonators,” *Proceedings of the IEEE International Conference on Micro Electro Mechanical Systems (MEMS)*, pp. 74–77, 2008, doi: 10.1109/MEMSYS.2008.4443596.

[33] E. F. F. Chladni, “Entdeckungen über die Theorie des Klanges,” 1787.

[34] M. D. Waller, “Vibrations of free square plates: Part I. Normal vibrating modes,” *Proceedings of the Physical Society*, vol. 51, no. 5, pp. 831–844, 1939, doi: 10.1088/0959-5309/51/5/312.

[35] J. Kim, D. Cho, and R. S. Muller, “Why is (111) Silicon a Better Mechanical Material for MEMS?,” in *Transducers ’01 Eurosensors XV*, Springer Berlin Heidelberg, 2001, pp. 662–665. doi: 10.1007/978-3-642-59497-7_157.

[36] K. E. Petersen, “Silicon as a Mechanical Material,” *Proceedings of the IEEE*, vol. 70, no. 5, pp. 420–457, 1982, doi: 10.1109/PROC.1982.12331.

[37] L. Zhang, R. Barrett, P. Cloetens, C. Detlefs, and M. Sanchez Del Rio, “Anisotropic elasticity of silicon and its application to the modelling of X-ray optics,” *Journal of Synchrotron Radiation*, vol. 21, no. 3, pp. 507–517, 2014, doi: 10.1107/S1600577514004962.

[38] H. Watanabe, N. Yamada, and M. Okaji, “Linear Thermal Expansion Coefficient of Silicon from 293 to 1000 K,” *International Journal of Thermophysics 2004 25:1*, vol. 25, no. 1, pp. 221–236, Jan. 2004, doi: 10.1023/B:IJOT.0000022336.83719.43.

[39] B. El-Kareh, “Fundamentals of Semiconductor Processing Technology,” *Fundamentals of Semiconductor Processing Technology*, 1995, doi: 10.1007/978-1-4615-2209-6.

[40] M. A. Hopcroft, W. D. Nix, and T. W. Kenny, “What is the Young’s modulus of silicon?,” *Journal of Microelectromechanical Systems*, vol. 19, no. 2, pp. 229–238, 2010, doi: 10.1109/JMEMS.2009.2039697.

[41] D. Ullmann, “Life and work of E.F.F. Chladni,” *The European Physical Journal Special Topics 2007 145:1*, vol. 145, no. 1, pp. 25–32, Sep. 2007, doi: 10.1140/EPJST/E2007-00145-4.

[42] A. E. H. Love, “XVI. The small free vibrations and deformation of a thin elastic shell,” *Philosophical Transactions of the Royal Society of London. (A.)*, vol. 179, pp. 491–546, Dec. 1888, doi: 10.1098/rsta.1888.0016.

[43] S. P. Timoshenko, “ LXVI. On the correction for shear of the differential equation for transverse vibrations of prismatic bars ,” *The London, Edinburgh, and Dublin Philosophical Magazine and Journal of Science*, vol. 41, no. 245, pp. 744–746, May 1921, doi: 10.1080/14786442108636264.

[44] B. Eric Reissner, “The Effect of Transverse Shear Deformation on the Bending of Elastic Plates,” *Journal of Applied Mechanics*, vol. 12, no. 2, pp. A69–A77, Jun. 1945, doi: 10.1115/1.4009435.

[45] R. D. Mindlin and N. York, “Influence of Rotatory Inertia and Shear on Flexural Motions of Isotropic, Elastic Plates,” *Journal of Applied Mechanics*, vol. 18, no. 1, pp. 31–38, Mar. 1951, doi: 10.1115/1.4010217.

[46] S. P. Timoshenko, “Theory of Plates and Shells (McGraw-Hill Classic Textbook Reissue Series),” p. 568, 1964.

[47] S. Chakraverty, *Vibration of Plates*. CRC Press, 2008. doi: 10.1201/9781420053968.

[48] Y. Xing, G. LI, and Y. Yuan, “A review of the analytical solution methods for the eigenvalue problems of rectangular plates,” *International Journal of Mechanical Sciences*, vol. 221, p. 107171, May 2022, doi: 10.1016/J.IJMECSCI.2022.107171.

[49] J. W. S. B. Rayleigh, “The theory of sound,” 1877.

[50] W. Ritz, “Über eine neue Methode zur Lösung gewisser Variationsprobleme der mathematischen Physik,” 1908.

[51] W. Ritz, “Theorie der Transversalschwingungen einer quadratischen Platte mit freien Rändern,” *Ann Phys*, vol. 333, no. 4, pp. 737–786, 1909, doi: 10.1002/andp.19093330403.

[52] S. S. Rao, *Vibration of Continuous Systems*. John Wiley and Sons, 2007. doi: 10.1002/9780470117866.

[53] S. Ilanko, L. E. Monterrubio, and Y. Mochida, *The Rayleigh-Ritz Method for Structural Analysis*. wiley, 2014. doi: 10.1002/9781118984444.

[54] D. Young, “Vibration of Rectangular Plates by the Ritz Method,” *Journal of Applied Mechanics*, vol. 17, no. 4, pp. 448–453, Dec. 1950, doi: 10.1115/1.4010175.

[55] A. W. Leissa, *Vibration of plates*, vol. 160. Scientific and Technical Information Division, National Aeronautics and Space Administration, 1969.

[56] A. Lemke, “Experimentelle Untersuchungen zur W. Ritzschen Theorie der Transversalschwingungen quadratischer Platten,” *Ann Phys*, vol. 391, no. 13, pp. 717–750, 1928, doi: 10.1002/andp.19283911304.

[57] R. Ali and S. J. Atwal, “Prediction of natural frequencies of vibration of rectangular plates with rectangular cutouts,” *Computers and Structures*, vol. 12, no. 6, pp. 819–823, Dec. 1980, doi: 10.1016/0045-7949(80)90019-X.

[58] S. Pala, “Temperature detection using micro plate vibrations,” Middle East Technical University, Ankara, 2017. Accessed: May 22, 2021. [Online]. Available: https://open.metu.edu.tr/handle/11511/26473